The University Of Sheffield.

Further Investigation of Hydrogen-air Diffusion Flame Ignition Behaviour and Flame Colour

Miss Muyi Pan

May 2022

This thesis is submitted to the Department of Mechanical Engineering, University of Sheffield in fulfilment of the requirements for the degree of Doctor of Philosophy.

Declaration

The work presented in this thesis is that of the Author and has not been submitted for any other award or degree at the University of Sheffield or any other university or institution.

Dedication

For my nieces and nephews: Xucheng Yin, Shaowen Pan, Shirong Pan, Yuning Pan, Yaowen Liang, Songning Yang and Shiyuan Pan.

Acknowledgements

First of all, I would like to show my greatest appreciation to my supervisor Professor Yang Zhang. I would not have found my research direction easily and presented my research results without his guidance and help.

Second, I would like to express my gratitude to my beloved parents, Mr. Xiaoping Pan and Mrs. Caiyun Tang. Thank them for their education and support over the past twenty-eight years. The care and love they gave me during the tough times gave me the courage to face all the difficulties in my life.

Also, I would like to give my thanks to my grandparents, Mr. Haiqing Pan, Mr Yusheng Tang, and Mrs. Yueqin Dong, for their understanding, support, and love. Especially to my grandfather, Mr. Haiqing Pan, who was a great man, and I will never forget him.

Apart from that, I would like to thank my colleagues. To Mr. Xuanqi Liu, who helped me with my experiment generously; To Dr. Xiao Wang and Mr. Ahemd Albadi for the happy time we spent together in the lab; To Dr. Hangxu Zhou, who gave me a lot of help in daily life; To Dr. Yufeng Lai, who gave me plenty of precious advice; To Dr. Jing Zhang and Mr. Yuchen Zhang for the help on data processing. Also, I would like to show my appreciation to Dr. Lukai Zheng, Dr. Yiran Wang, Dr. Houshi Jiang, Dr. Ahmad Muneer El-Deen Faik, Mr. Shuaida Ji, Mr. Haibo Zhou, and Mr. Xiangfei Meng.

I would like to show my gratitude to Mr. Ian Fu, who supported me to overcome all the difficulties over the past five years, I will never forget the lovely time we spent together; To my faithful friends Mr. Shuan Shen, Mrs. Jingyi Yang, Miss Huayi Fang,

Mrs. Jiaxin Peng, Mrs. Shurui Yu, Miss Jingxuan Zhao, Miss Siyu Qiu, Mr. Zhikun Li, Mr. Yongqiang Hu, Mr. Keya Li, Mr. Quanliang Zhang, and Mr. Yifan Li, our friendship will last long and never fade away.

Finally, I would like to especially thank my adorable pets, Oreo and Big Paw, for the happiness and companionship they give to me.

星霜荏苒，居诸不息，四载春秋，潜精研思。

椿萱之恩，明师之诲，砚席之谊，感佩不忘。

白袷蓝衫，莫道人生多歧路，长风破浪正当时。

Publications

Muyi Pan, Xiao Wang, Ahmed Albadi, Y P Han and Yang Zhang, "Further investigation of hydrogen flame colour", in the 27th International Colloquium on the Dynamics of Explosions and Reactive System (27th ICDERS), Beijing, China, 2019.

Muyi Pan, Xuanqi Liu, Ahmed Albadi, Yufeng Lai, Xiao Wang, Yuchen Zhang and Yang Zhang, "Resolving visible emission lines in a hydrogen-air diffusion flame", *Combustion and Flame*. Under Review.

Under preparation:

Muyi Pan, Yufeng Lai, Xuanqi Liu and Yang Zhang, "Investigation of hydrogen-air diffusion flames spectra in the wavelength range of 590 nm to 700 nm".

Abstract

Hydrogen-air diffusion flame is commonly described as colourless. However, even in controlled laboratory conditions with careful imaging, the flame appears reddish. Although hydrogen flame colour was first described as "faint reddish-brown" by W. F. Barrett in 1872 [1], the misconception about if the hydrogen flame colour is invisible still has not been well addressed until today.

In this research, the ignition process of hydrogen flame is captured by using schlieren imaging and high-speed imaging technique. The flame colour of soapy hydrogen bubble is yellow while of distilled water hydrogen bubble is more reddish. The hydrogen-air diffusion flame direct images are captured by a DSLR camera as well. Various co-flow conditions are applied and the colour of the flames are slightly different but generally red.

The spectra of hydrogen-air diffusion flame in the wavelength range of 590 nm to 700 nm are analysed in this research. Air and oxygen co-flow with different flow rate are applied as comparisons. The intense emission lines in this wavelength range are identified according to the HITRAN and the NIST database. The spectra of hydrogen diffusion flame under different co-flow conditions are similar. H_2O and OH contribute significantly to the reddish flame colour, and some other elements from the equipment or atmosphere also have contributions. Furthermore, the results approved that H_2O and OH provide more emission lines in the hydrogen flame with co-flows, which might be due to the higher flame temperature. Moreover, the

emission line of $H-\alpha$ also presents in the spectra. Therefore, it is highly possible that $H-\alpha$ participates in the reaction and emits light in the combustion process of hydrogen diffusion flame.

Contents

List of Figures

List of Tables

Nomenclecture

PAHs	Polycyclic Aromatic Hydrocarbons
DSLR camera	Digital Single-lens Reflex camera
RGB	Red, Green, Blue primary colours
$H-\alpha$	Hydrogen alpha
HITRAN	High-resolution Transmission Molecular Absorption Database
NIST	National Institute of Standards and Technology Database
ϕ	Equivalence ratio
m_{fuel}	Mass of fuel
m_{ox}	Mass of oxygen
n_{fuel}	Mole number of fuel
n_{ox}	Mole number of oxygen
CH^*	Excited methylylidene radical
C_2	Diatomic carbon
CO_2	Carbon dioxide
H_2O	Water
OH^*	Excited hydroxyl radical
H_2	Hydrogen

O_2	Oxygen
H	Hydrogen atom
N_2	Nitrogen
Ar	Argon
HO_2	Hydroperoxyl
H_2O_2	Hydrogen peroxide
O_3	Ozone/Trioxygen
N_2O	Nitrous oxide
NH_3	Ammonia
HNO_3	Nitric acid
NO	Nitric Oxide
NO^+	Nitrosonium ion
UHP	Ultra high purity
$\upsilon(\sigma), \upsilon(\pi), \delta(\pi)$	Vibrational states
$V(\sigma), V(\pi), V(\delta)$	Vibrational quantum numbers
λ	Wavelength
υ	Wavenumber
E	Energy
h	Planck's constant

$\bar{\nu}$	Emission frequency
c	Velocity of light
r	Radius
n	Refractive index
C_0	Speed of light travels in vacuum
$\Delta\varepsilon$	Differential angle
α	Incident light angle
β_m	Diffraction light angle (m is the order of diffraction)
d	Groove spacing/pitch
G	Groove frequency/density
ε	Angle between the plane perpendicular to the grooves and the incident light path
θ	Diffraction angle of the light
R	Resolving power
$\Delta\lambda$	Limit of resolution
ϕ	Phase angle of the first minimum
N	Number of illuminate slits
CCD	Charge-Couple Device
MOS	Metal-Oxide-Semiconductor

ADC	Anlog-Digital Converter
SNR	Signal-to-Noise Ratrio
fps	Frames per second
q	Flow rate
ρ	Density
XCO_2	Concentration of carbon dioxide
T	Temperature in Kelvin
t	Temperature in degree Celsius
M	Atomic weight in atomic mass unit (amu)
FWHM	Full width at half maximum intensity
f_r	Oscillator strength
g_i	Stastical weights of upper level
g_k	Stastical weights of lower level
N_i	Ground state number density
Tl	Thallium
I	Iodine
Cm	Curium
Ti	Titanium
Pm	Promethium

Au	Gold
Si	Silicon
Xe	Xenon
Tm	Thulium
Eu	Europium
Ne	Neon
Te	Tellurium
Kr	Krypton
Sb	Antimony
Ce	Cerium
Al	Aluminum
P	Phosphorus
Ar	Argon
Sn	Tin
In	Indium
Zr	Zirconium
Cs	Cesium
Tc	Technetium
V	Vanadium

Ba	Barium
U	Uranium
Cu	Copper
Pa	Protactinium
Se	Selenium
Ra	Radium
Pr	Praseodymium
Pt	Platinum

Chapter 1: Introduction

1.1 Motivation

The use of fire is a turning point in the development of human culture and technology. Humans have been studying combustion for centuries. Combustion is a study of gaseous fuels, liquid fuels, and solid fuels, including the ignition, flameout, combustion process, and mechanism. The application of combustion is used in various fields such as aerospace, aviation, machinery, electronics, materials engineering, etc. However, in addition to its essential role in human development, combustion also has some hazards. Traditional fuels produce a lot of waste, including carbon dioxide, soot particles, polycyclic aromatic hydrocarbons (PAHs), and other substances that are polluting the environment [2]. Therefore, the research and application of clean energy are vital. In recent decades, there has been a growing interest in hydrogen as clean energy. Hydrogen is a light, storable, reactive, and high energy content per unit mass gaseous fuel [3].

However, while the application of hydrogen brings significant advantages, there are also many problems. Hydrogen is odorless; hence it is challenging to detect if any leakage happens. Also, its flammability range is vast compared to natural gas or gasoline, and its ignition energy is 20 times lower. Besides, hydrogen flame is almost

invisible in natural light conditions. Therefore, hydrogen can cause severe fires if leaked or misused [4].

Fundamental research on hydrogen can provide the theoretical basis for the application of hydrogen and make the use of hydrogen safer and more efficient. One of the unconcluded characteristics of hydrogen is its flame colour. There have been researches reporting a variety of colours generated from hydrogen flames. Some researchers believe that the visible colour is due to impurties in airborne dust, mainly sodium. Other studies also suggest that the vibrational-rotational band of water vapour causes the reddish flame colour.

The presence of the hydrogen $H-\alpha$ spectrum is also a possible cause of the reddish flame colour of hydrogen. In detail, such a spectrum is relatively close to the proverbial sodium colour, which may overshadow the reddish colour. As a possible reason for such reddish colour appearing in blue hydrogen flame, the $H-\alpha$ may be considered based upon the Bohr atom model. When the electron energy level of hydrogen falls from n = 3 to n = 2, $H-\alpha$ will be emitted in visible red light colour (656.28 nm) [5] and possibly contribute to the reddish colour of a hydrogen flame. Furthermore, *H* radicals are abundant during combustion, and those excited H radicals may emit hydrogen-alpha $(H-\alpha)$ light. Therefore, it is also likely for $H-\alpha$ to exist in a hydrogen flame.

Detailed analysis of hydrogen flame colour may supply a possibility for a new diagnostic method in terms of the combustion of hydrogen-containing gaseous fuel. Therefore, the detailed study of hydrogen flame colour is critical and meaningful.

1.2 Aim and Objectives

This project aims to analyse the hydrogen flame colour in the red colour band, including the ignition process flame colour, the stable hydrogen-air diffusion flames under different co-flow conditions, the spectrum of hydrogen-air diffusion flame under different co-flow conditions. Also, to investigate the possible contributions of various species to the reddish flame colour.

To achieve the aim of this project, the main objective is to capture the images of the hydrogen ignition process, the images and the spectrum of hydrogen-air diffusion flame under different co-flow conditions. Then find out the strong emission lines in the red colour range, and match them with different species. The sub-objectives of this research are listed below:

Hydrogen flame ignition process visualisation experiment

- To set up a synchronized schlieren imaging and high-speed imaging system.
- To prepare soapy and distilled water hydrogen bubbles.
- To analyse the behaviour of hydrogen during the ignition process through the schlieren images.
- To find out and analyse the RGB channel values of the hydrogen bubble ignition images captured by the high-speed camera.
- To compare the similarities and differences between soapy and distilled water hydrogen bubble flame colours.

Hydrogen-air diffusion flame direct imaging visualization experiment

- To capture the hydrogen-air diffusion flames under different co-flow

conditions with the same DSLR camera settings.

- To find out and analyse the RGB channel values of the flame images.
- To compare the similarities and differences between the hydrogen flames under different co-flow conditions.
- To capture and analyse the hydrogen-air diffusion flame with a narrowband filter ($H-\alpha$ filter).

Hydrogen-air diffusion flame spectrum experiment

- To set up a precisely instrumented spectroscopic imaging system.
- To calibrate the hydrogen-air diffusion flame (with/without co-flow) spectrum with sodium double lines.
- To pick out the strong emission lines in the range of red light by using Python script.
- To find out species which might involve in the combustion process.
- To find out emission lines of the possible species in the range of 590-700 nm by using the High-resolution Transmission Molecular Absorption Database (HITRAN) (https://hitran.org/) [6] and National Institute of Standards and Technology (NIST) database (https://physics.nist.gov/) [7].
- To identify the emission lines in the hydrogen-air diffusion flame spectrum by matching them with the data provided by the databases.
- To compare the relative intensity of these species under different combustion conditions, including hydrogen-air diffusion flame, hydrogen-air diffusion flame with air co-flow, and hydrogen-air diffusion flame with oxygen co-flow.
- To determine the contribution of $H-\alpha$ on the reddish flame colour of

hydrogen flames.

1.3 Structure of the thesis

This thesis contains seven chapters; a brief of each chapter is listed below:

Chapter 1 introduces the motivation, aim, objectives and structure of this thesis.

Chapter 2 gives the background information on combustion, hydrogen flames, and visualisation methods, including the schlieren imaging technique, direct imaging technique, and spectrograph.

Chapter 3 presents the hydrogen flame ignition process visualization experiment. It uses schlieren imaging and high-speed imaging techniques to visualize and analyse the soapy and distilled water hydrogen bubble flame during its ignition process.

Chapter 4 presents the direct images of hydrogen-air diffusion flame under different co-flow conditions. The similarities and differences between the flame colours are analysed. The possibility of the contribution of $H-\alpha$ is determined by a narrowband filter.

Chapter 5 analyses the results of the hydrogen-air diffusion flame spectrum. The intense emission lines in the range of 590-700 nm are picked out and matched with the emission line data provided by HITRAN and NIST database. Hence the possible species that contributed to the reddish flame colour could be identified.

Chapter 6 analyses the spectra of hydrogen-air diffusion flame with different co-flow conditions. The emission lines in the same range are compared with the hydrogen diffusion flame without co-flow. Species and elements that contributed to

the reddish colour of hydrogen diffusion flame are further verified.

Chapter 7 concludes all the research methods and results involved in this study. Future works related to the hydrogen spectrum are discussed, and the possibility of applying the results to industrial applications is presented.

Appendices and references are listed at the end of this thesis.

Chapter 2: Literature review

2.1 Overview of combustion

Combustion is a complex process that involves physical and chemical reactions. It is closely related to daily life. The development of civilization is inseparable from combustion. The substance that could be combusted and release energy is defined as chemical fuel. There are three types of chemical fuel in general: solid fuel (wood, coal etc.), liquid fuel (petrol, diesel etc.) and gaseous fuel (hydrogen, methane, propane etc.).

At the current stage, global demands of natural gas keep growing fast [8]. However, natural gas is not renewable energy, which means it will finally be used up. Also, the combustion of natural gas produces a large amount of greenhouse gas. Therefore, new fuels are urged to be used to replace those currently used traditional fuels [9].

Research in the combustion properties of different fuels is essential. With understanding the properties of the fuel, its combustion process could be monitored and optimised, hence saving energy and improving efficiency. Combustion properties of fuel include burning rate, ignition energy, flame structure and flammability etc.

2.2 Flames of gaseous fuel

In this project, flames of gaseous fuel are studied. Bunsen burner is one of the most commonly used laboratory gas burners.

Bunsen burner was invented by German chemist Robert Wilhelm Bunsen and British chemist Henry Enfield Roscoe in 1857 based on the gauze burner, a former commonly used laboratory gas burner.

The gauze burner is a burner that mixes gaseous fuel and oxidizer in a cylindrical metal chamber before ignition. A metal gauze is added to the top of the burner outlet to prevent flashbacks. However, the metal gauze greatly influences the flame, such as flame stability and colour [10]. To eliminate the disadvantages of the gauze burner, Bunsen and Roscoe improved the burner. The cylindrical metal chamber was replaced by a long and narrow tube. Fuel and oxidizer mix in the tube. At the same time, pressure in the tube before ignition is positive to prevent flashbacks.

Bunsen burner can provide both diffusion and premix flames. Fuel enters the burner with a gas pipe at the bottom, and the valve controls the oxidizer inlet. Fig. 1 is a drawing Bunsen burner [10] [11].

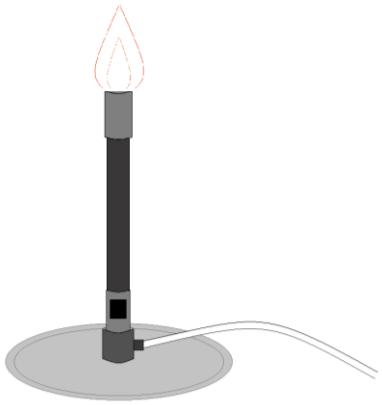

Fig. 1: Schematic drawing of a typical Bunsen Burner.

The equivalence ratio (∅) is an essential parameter in combustion. It is defined as:

Equivalence ratio (∅) **Equation. 1**

$$= \frac{\boldsymbol{Actural\ fuel/oxidizer\ ratio}}{\boldsymbol{Stoichiometric\ fuel/oxidizer\ ratio}}$$

It could also be defined by mass or the number of moles.

$$\emptyset = \frac{\frac{\boldsymbol{m_{fuel}}}{\boldsymbol{m_{ox}}}}{\left(\frac{\boldsymbol{m_{fuel}}}{\boldsymbol{m_{ox}}}\right)_{\boldsymbol{st}}} = \frac{\frac{\boldsymbol{n_{fuel}}}{\boldsymbol{n_{ox}}}}{\left(\frac{\boldsymbol{n_{fuel}}}{\boldsymbol{n_{ox}}}\right)_{\boldsymbol{st}}} \qquad \textbf{Equation. 2}$$

Where m is the mass and n is the mole number, the subscript st means the stoichiometric condition.

Stoichiometric condition is defined as the ratio of mass or mole number of fuel and oxidizer that satisfies the chemical reaction equation. Under this condition, the oxidizer is entirely consumed by all the provided fuel [12].

The equivalence ratio is also used to define fuel to oxidizer conditions. Fuel lean condition is when $\emptyset < 1$, and the fuel-rich condition is when $\emptyset > 1$.

There are mainly three types of flame in gaseous fuel combustion: premixed, partially premixed, and diffusion, depending on the mixing condition of fuel and oxidizer prior to the combustion process.

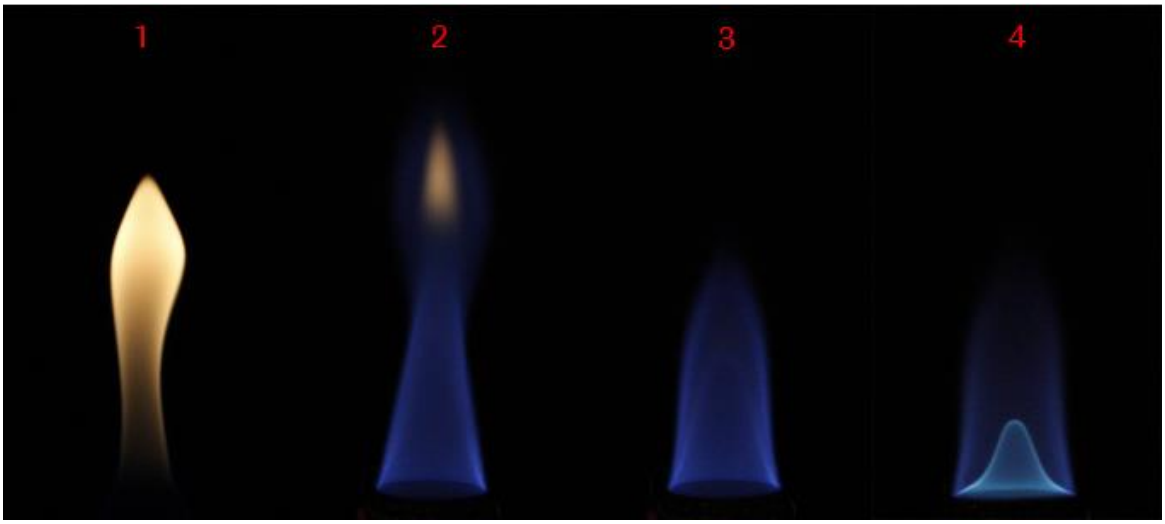

Fig. 2: Bunsen flame of methane-air flame: 1) Diffusion flame; 2) Partially premixed flame (less air condition); 3) Partially premixed flame (more air condition); 4) Premixed flame.

Fig. 2 demonstrates that different flames are different in both shape and colour, and it represents that the detailed mechanism of combustion under various oxidation conditions is different.

2.2.1 Diffusion flame

Diffusion flame occurs when fuel and oxidizer enter the same zone with turbulent and molecular diffusion [6]. Fuel enters the zone and is then mixed with an oxidizer to reach its flammability range.

According to Glassman *et al.*, the structure of the diffusion flame is more complex than the premixed flame. Diffusion flame has a more comprehensive chemical

reaction and composition change zone [13]. The rate of fuel and oxidizer mixing is lower than the rate of the chemical reaction. The figure below indicates the typical diffusion flame structure generated from the Bunsen burner.

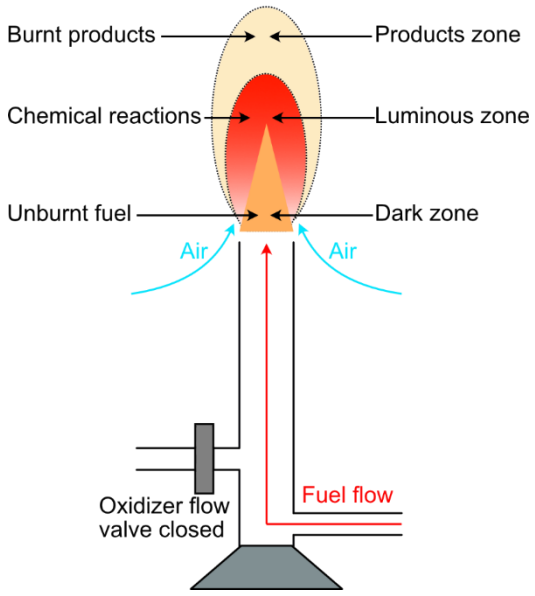

Fig. 3: Bunsen burner diffusion flame Structure.

The oxidizer flow valve is closed to generate a diffusion flame by cutting off the oxidizer flow input. Fuel is only mixed with the surrounding air.

Furthermore, due to the separate storage of fuel and oxidizers, diffusion flame is commonly used in industries as a consideration of safety. However, the instability of flame is still a fundamental research topic. The instability of flame is mainly caused by the buoyancy forces generated by the flame's high temperature. Co-flow is usually used in a diffusion flame to increase its stability [14] [15]. Fig. 4 is a typical co-flow laminar diffusion flame burner.

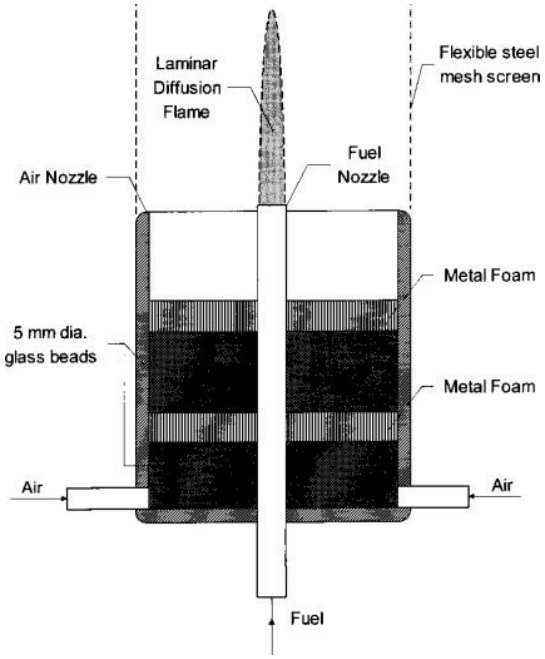

Fig. 4: A typical co-flow laminar diffusion flame burner [16].

Laminar diffusion flames with co-flow result in longer and more stable flames due to an increased flow rate. Fig. 5 is an example of different flow rate laminar propane diffusion flames with a fixed co-flow rate at 6.2 cm/s. It can be seen from the figure that the flame length is proportional to the propane flow rate.

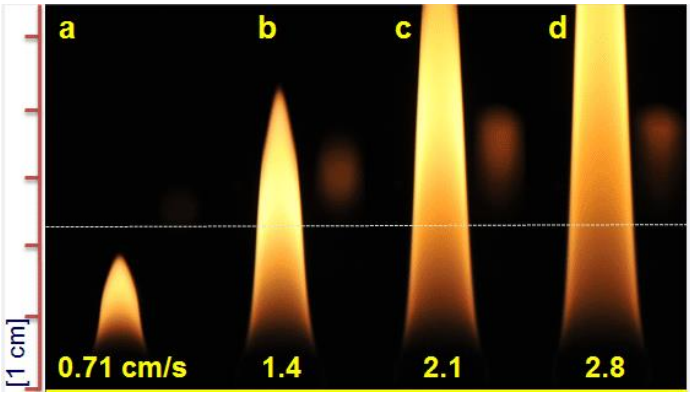

Fig. 5： Propane diffusion flame at: a) 0.71 cm/s; b) 1.4 cm/s; c) 2.1 cm/s; d) 2.8 cm/s. The fixed co-flow rate is 6.2 cm/s [17].

2.2.2 Premixed flame

The premixed flame is generated when fuel and oxidizer are mixed homogenously before ignition. The structure of a typical premixed flame is shown in Fig. 6. The dark zone is the unburnt fuel-oxidizer mixture. Chemical reactions and heat release happen in the luminous zone, and the temperature in this zone is the highest [18].

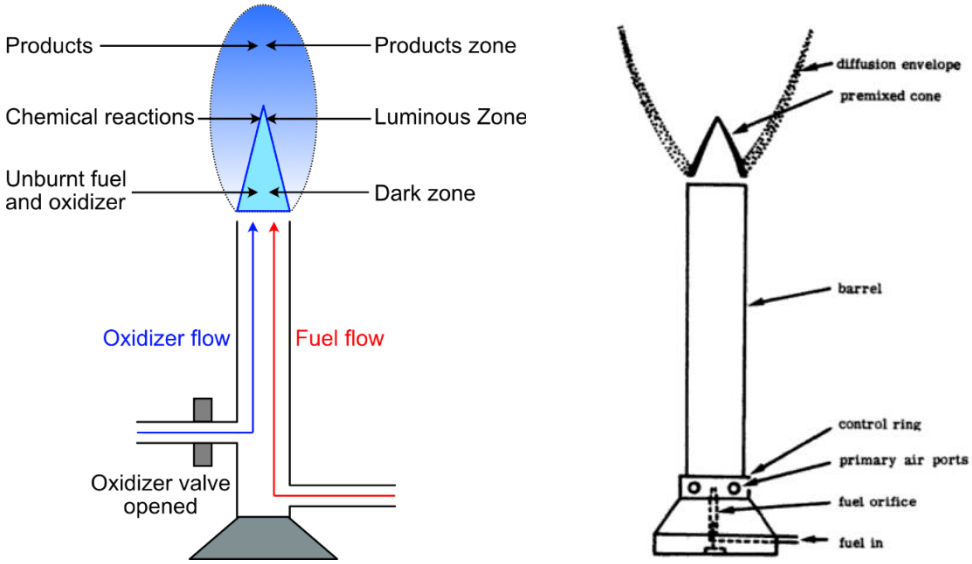

Fig. 6: Bunsen burner premixed flame structure with left: fully opened oxidizer valve at the beginning; Right: gradually opened oxidizer valve (primary air ports in the figure) [19].

According to Murty, a diffusion envelope appears when the oxidizer valve opens gradually. The premixed flame cone reduces its size with the increase of oxidizer flow input, and the diffusion envelope gradually disappears simultaneously. Once the input oxidizer flow reaches the stoichiometric condition, the diffusion flame envelope disappears and remains only the bluish premixed cone. Moreover, compared to the Bunsen burner diffusion flame, the premixed flame is shorter and dimmer [19].

2.2.3 Partially premixed flame

The partially premixed flame is generated when the available fuel exceeds the stoichiometric condition. Part of the fuel mixes with oxidizer before ignition and behaviours as the premixed flame. The rest part of the fuel diffuses into the surrounding air and shows diffusion flame behaviour. Hence, a typical partially premixed flame has both premixed flame and diffusion flame characteristics.

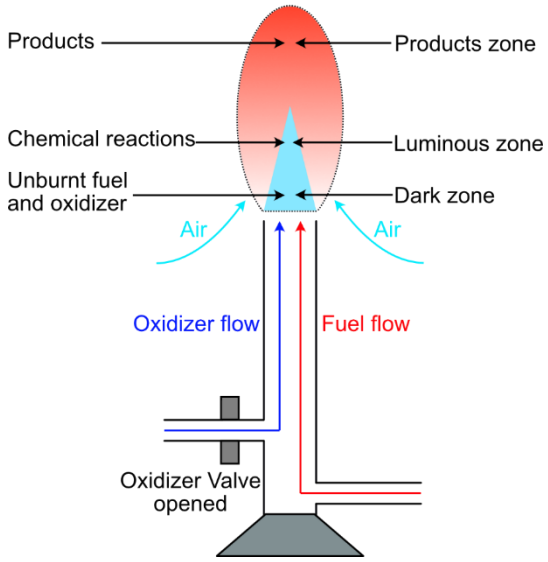

Fig. 7: Bunsen burner partially premixed flame.

2.3 Mechanism of atomic/molecular emission of flames

The emission of atomic/molecular from a flame is mainly due to thermal causes or chemiluminescence. This involves particles in motion due to thermal energy, resulting in emission of radiation.

In thermal excitation, the main sources of energy that contribute to the atoms and

molecules are collision energy and thermal interactions. Bohr's theory states that atoms and molecules can only stay in stationary states, which are selected by specific quantum conditions. Light emission happens when an atom or molecule transits from one energy state to another [20].

$$\boldsymbol{E_1 - E_2 = h\bar{\nu} = hc\nu} \qquad \textbf{Equation. 3}$$

Where E is the energy of the state. $E_1 - E_2$ is the energy difference between two states.

h is the Planck's constant, which equals $6.63 \times 10^{-34} m^2 kg/s$.

$\bar{\nu}$ is the emission frequency.

c is the velocity of light.

ν is the wavenumber in cm^{-1} [20].

A typical molecule energy is associated with translation, rotation, vibration, and potentially electronic excitation. At ordinary and high temperatures, the translational and rotational degrees of freedom of the molecules are fully excited, but the same may not hold true for the vibrational and electronic excitation. According to the Boltzmann distribution, the number of molecules with a given energy E is proportional to $e^{-\frac{K}{kT}}$, with T for absolute temperature and k for the gas constant per molecule. At a higher temperature, the vibrational degree of freedom will become important, and the specific heat will be higher, which also leads to a more intense spectral emission [20].

Collisions have the potential to transfer energy between species. It is likely that collisions between particles of molecular or atomic masses are the most effective

means of inducing excitation. The possibility of a molecule being excited to an electronic state where there is a difference in nuclear separation compared to its initial value is higher.

Emission in flame due to chemiluminescence is caused by the chemical reactions, which release energy in the form of photons. Excited species transits between their electronic energy levels in the chemical reaction and releasing photons of characteristic wavelengths. Normally, emission lines due to chemiluminescence are discrete.

In both thermal causes and chemiluminescence, the amount of energy available is limited, resulting in the observed spectra always corresponding to transitions between low energy states [20].

2.4 Flame colour of gaseous fuel

Referring to Gaydon, the most significant difference between combustion and other chemical reactions is light emission [21]. Flame releases a different spectrum due to the excitement of species. Photons release energy in the process and emit lights [22] [23]. Flame colour is different for every flame [21].

Human eyes are only sensitive to a narrow band of spectrum. The wavelength of visible light is from about $350\ nm$ to $750\ nm$, as shown in Fig. 8. The Colour of a flame is determined by the visible light emitted. However, the spectrum of flame also covers ultraviolet and infrared.

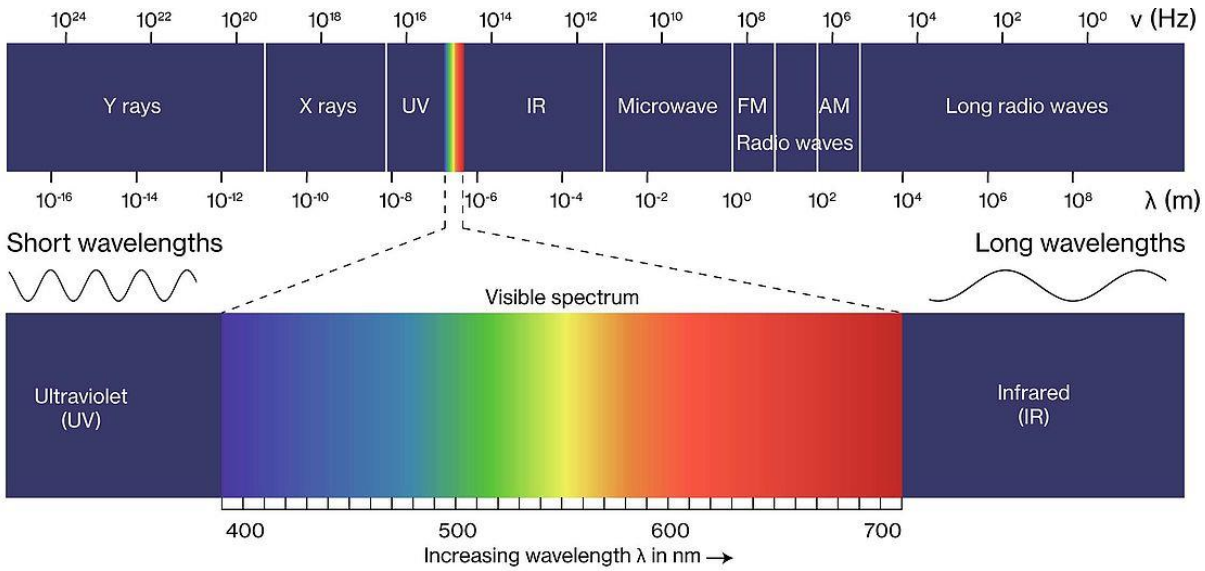

Fig. 8: Spectrum of all wavelength range and in visible range [24].

For a typical Bunsen burner Hydrocarbon flame, the bluish inner cone is a combination of blue, green and violet lights [24]. The excited radical CH^* emits light with $430\ nm$ wavelength, and C_2 emits lights with $473.71\ nm$ and $516.52\ nm$. Spectra of CH^* and C_2 radicals produce the the blue flame colour. The orange colour is contributed by the grey-body radiation of the incandescent soot. Besides the visible lights, hydrocarbon flame also gives lights in the infrared and ultraviolet range. The products of hydrocarbon flame include $\mathrm{CO_2}$, $\mathrm{H_2O}$ and $\mathrm{OH^*}$ radicals. $\mathrm{CO_2}$ contributes a strong emission band at $4.4\ \mu\mathrm{m}$ and another band at $2.8\ \mu\mathrm{m}$. $\mathrm{H_2O}$ provides light with a $2.8\ \mu\mathrm{m}$ wavelength. Spectra lines emitted by $\mathrm{CO_2}$ and $\mathrm{H_2O}$ are both in infrared. Meanwhile, light emitted by $\mathrm{OH^*}$ radicals have a wavelength of $309\ \mathrm{nm}$, which is in the ultraviolet range. Hydrocarbon gas diffusion flame, such as methane and propane, presents orange or red colour with some weak blueish emissions. It has been proved that the orange flame colour is due to the soot emission generated in the combustion process. The orange colour is contributed by the grey-body radiation of the

incandescent soot [25]. Fuel composition affects its flame colour predominantly. Fuel with rich carbon content has the brightest inner cone and strongest C_2 emission bands. Strong OH^* emission bands occur in fuel with oxygen content. Fig. 9 shows the emission of a typical hydrocarbon flame.

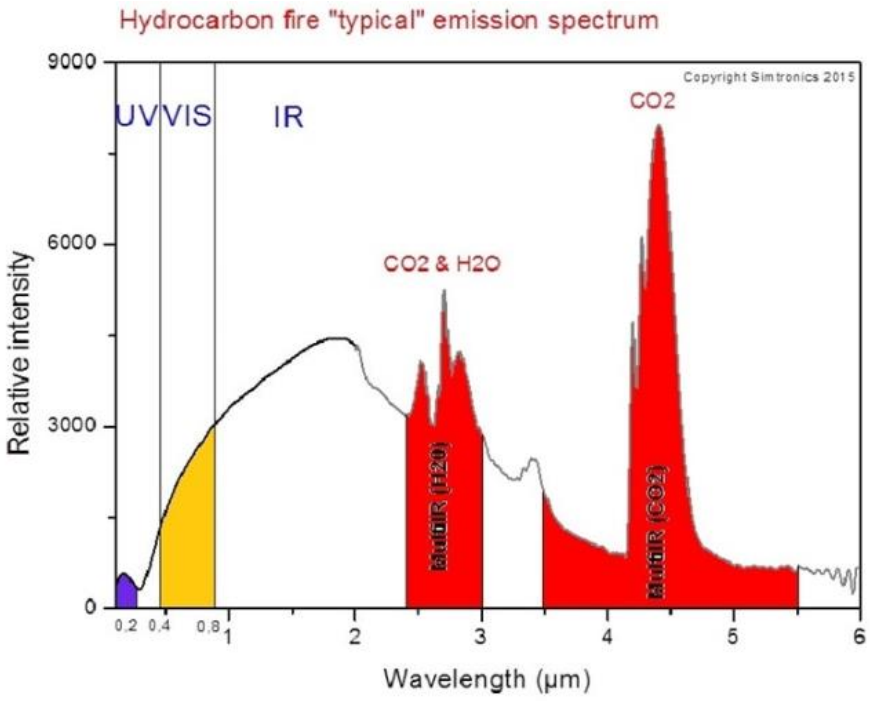

Fig. 9: Typical hydrocarbon flame emission spectrum [26].

In addition to the fuel composition, the intensity of emission bands of a premixed flame is also based on the equivalence ratio. Fig. 10 is the variation of $\boldsymbol{C_2}$ and $\mathbf{CH}$ emission in a low-pressure ethylene/oxygen flame under different equivalence ratios.

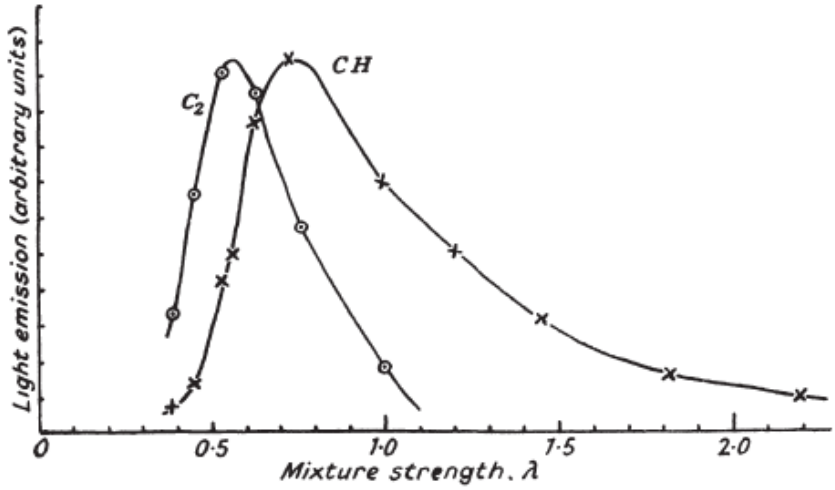

Fig. 10: Variation of C_2 and CH emission in a low-pressure ethylene/oxygen flame [21].

λ is defined as the mixture strength, which is the reciprocal of the equivalence ratio.

Flame temperature determines the emission intensity of diffusion flame containing carbon. High-temperature soots generate grey-body radiation and emit a continuous spectrum. Different temperature decides the intensity distribution in the continuum [21].

2.5 Hydrogen combustion

Hydrogen is the simplest and lightest atom on the Earth, and it is the most abundant element in the universe. However, Hydrogen does not naturally exist as a form of gas on the Earth. Instead, Hydrogen always combines with other elements to form a substance. For example, Hydrocarbon is one of the organic compounds which contains hydrogen. Hydrocarbon can be found in many fuels, including natural gas,

gasoline, methanol and propane. Therefore, to get hydrogen gas, artificial work should be applied. The two most common ways to get hydrogen are 'reforming' from natural gas and water electrolysis [27].

2.5.1 Hydrogen Properties

Hydrogen is a flammable gas; its lower flammability limit is 4%, and the upper flammability limit is 76% (in volume) at room temperature. The flammability limits of hydrogen are highly dependent on the initial pressure. The lower flammability limit decreases at the same temperature while the upper flammability limit increases with increasing initial pressure [28]. The flammability limits of hydrogen are influenced by temperature as well. Keeping the pressure constant and lowering the temperature would increase the lower limit and decreases the upper limit. Hence, the flammability range is narrowed down by decreasing initial pressure and temperature.

According to David Rainer [29], in air, hydrogen has the lowest ignition energy (0.019 mJ), highest diffusivity, and high burning velocity. In atmospheric air, the burning rate of hydrogen varies from 4 cm/s to 325 cm/s, which depends on the hydrogen concentration. Hydrogen-air laminar flame has the highest burning rate between equivalence ratios of $\emptyset = 1$ and $\emptyset = 2$.

Therefore, due to the high burning rate, low ignition energy, and wide flammability range, hydrogen is easier to transfer from detonation to ignition compared to other flammable gases. To prevent unwanted ignition, adding inert gases (e.g. nitrogen) could reduce the flammability range of Hydrogen [29].

2.5.2 Hydrogen combustion mechanism

In steady-state combustion, hydrogen reacts with oxygen in the air and produces water vapour as the only product [30]. The reaction could be represented by the following chemical reaction equation:

$$\boldsymbol{2H_{2(g)} + O_{2(g)} \longrightarrow 2H_2O_{(l)}}$$

In the equation, (g) represents the state of hydrogen and oxygen as gas, and (l) indicates H_2O is liquid [31].

The detailed mechanism of hydrogen-air combustion is listed as below:

Chain reaction of hydrogen combustion	
1a	$\mathrm{H + H + M = H_2 + M}$
1b	$\mathrm{H + H + H_2 = H_2 + H_2}$
1c	$\mathrm{H + H + N_2 = H_2 + N_2}$
1d	$\mathrm{H + H + H = H_2 + H}$
2	$\mathrm{O + O + M = O_2 + M}$
3	$\mathrm{O + H + M = OH + M}$
4a	$\mathrm{H_2O + M = H + OH + M}$
4b	$\mathrm{H_2O + H_2O = H + OH + H_2O}$
5a	$\mathrm{H + O_2(+M) = HO_2(+M)}$
5b	$\mathrm{H + O_2(+Ar) = HO_2(+Ar)}$
6a	$\mathrm{OH + OH(+M) = H_2O_2(+M)}$
6b	$\mathrm{OH + OH(+H_2O) = H_2O_2(+H_2O)}$
7	$\mathrm{O + H_2 = OH + H}$
8	$\mathrm{H + O_2 = OH + O}$
9	$\mathrm{H_2 + OH = H_2O + O}$
10	$\mathrm{OH + OH = H_2O + O}$

11	$HO_2 + O = OH + O_2$
12	$H + HO_2 = OH + OH$
13	$H + HO_2 = H_2O + O$
14	$H + HO_2 = H_2 + O_2$
15	$H_2 + O_2 = OH + OH$
16	$HO_2 + OH = H_2O + O_2$
17a	$HO_2 + HO_2 = H_2O_2 + O_2$
17b	$HO_2 + HO_2 + M = H_2O_2 + O_2 + M$
18	$H_2O_2 + H = HO_2 + H_2$
19	$H_2O_2 + H = H_2O + OH$
20	$H_2O_2 + O = HO_2 + OH$
21	$H_2O_2 + OH = HO_2 + H_2O$

Table. 1: Chain reaction of hydrogen combustion [32].

The species involved in hydrogen combustion mainly include H, H_2, N_2, O, O_2, OH, Ar, HO_2, and H_2O_2. Moreover, there are other species might also participate in the reaction due to the high temperature of the flames, including NO_2, N_2O, NH_3, NO, HNO_3, and O_3 etc.

2.5.3 Hydrogen ignition mechanism

Unlike steady combustion, hydrogen ignition is a rapid and energetic process. According to W. K. Kim [33], the propagation behaviour of hydrogen-air mixture depends on the equivalence ratio. In his research, the schlieren photography technique was used to record the ignition process of hydrogen-air soap bubbles with an equivalence ratio from 0.7 to 4.0.

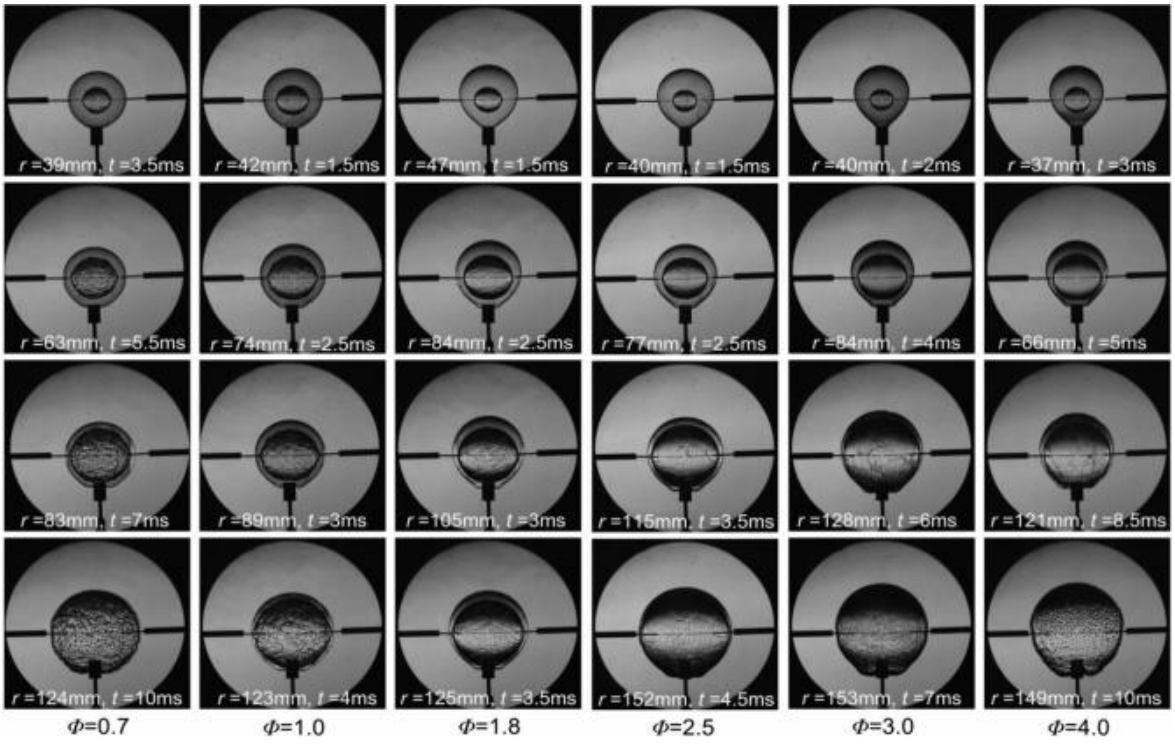

Fig. 11: Schlieren images of flame propagation at various equivalence ratios. r = flame radius, t =time from ignition [33].

Fig. 11 shows that when the equivalence ratio is lower than and equal to 2.5, the flame front winkles during propagation, while this phenomenon is not observed when equivalence is 3.0 and 4.0. Referring to Kim, winkling of flame front might be caused by spontaneous flame instability. In the cases of a higher equivalence ratio, he concluded that the flame was stabled due to a weaker combustion reaction at the convex segment towards the unburned gas and a more robust reaction at the concave segment. Besides, it could be noticed that flame propagation velocity increases with the increase of equivalence ratio before ϕ reaches 1.8, while the velocity decreases with the increase of equivalence ratio after ϕ greater than 3.0. [33].

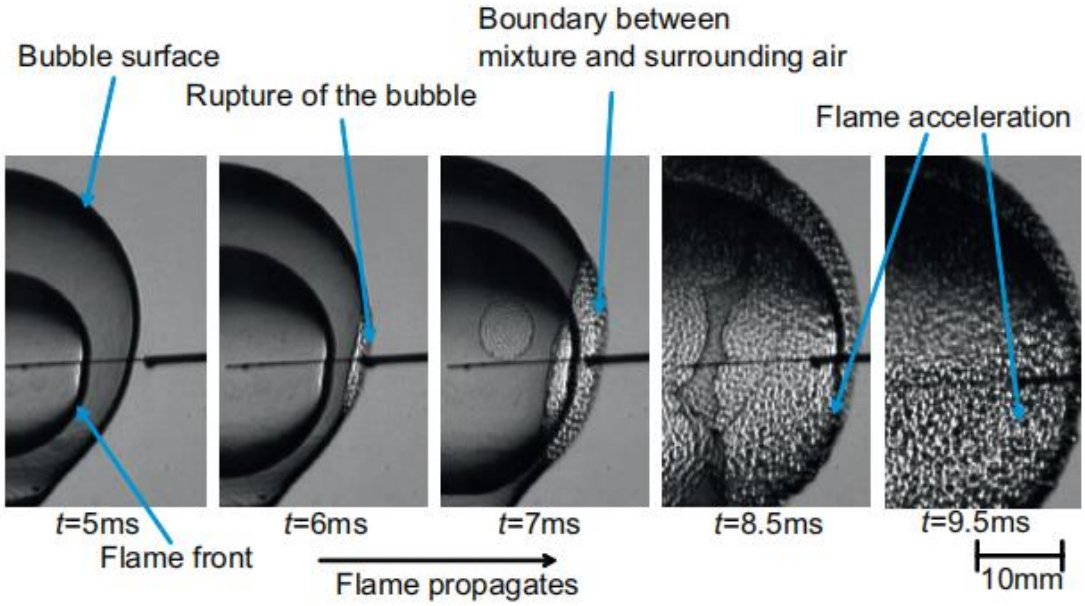

Fig. 12: Schlieren images of the mixing process of rich fuel mixture with air [34].

It can be seen from Fig. 12 that when the bubble is ignited, the flame propagates inside the bubble. Then the bubble ruptures from the edge just before the flame front reaches the boundary. After the bubble raptures, the rich fuel mixes with the surrounding air, and the flame acceleration occurs.

2.5.4 Hydrogen flame colour

Although hydrogen flame colour was firstly described as "faint reddish-brown" by W. F. Barrett in 1872 [1], the misconception about if the hydrogen flame colour is invisible still has not been well addressed until today. In detail, water (H_2O) is the only chemical product after the combustion of hydrogen and oxygen, of which the light emitted by water molecules is mainly in the infrared regime and hard to be observed by human eyes. Its emission bands in the visible range are very weak [35].

2.5.4.1 "Blue continuum"

R.W. Shefer proved that hydrogen flame is actually visible. The hypothesis raised by his group is the "Blue continuum".

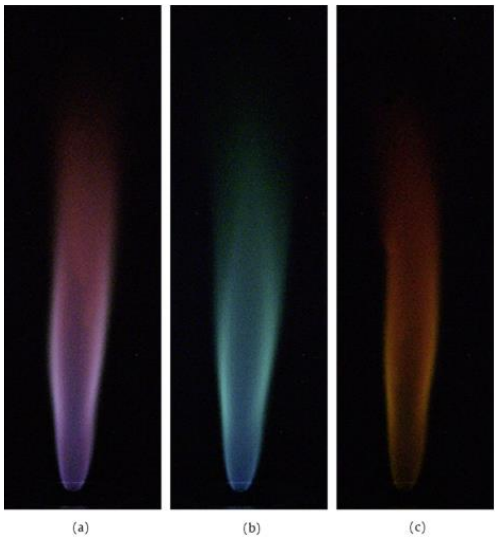

Fig. 13: Direct flame luminosity photography in a laminar diffusion H_2-air jet flame. (s) Unfiltered; (b) short-wavelength pass filter with 550nm cut-off wavelength; (c) long-wavelength pass filter with 530nm cut-off wavelength [36].

In Shefer's experiments [36], the aperture used for the image is f/2.4, and the exposure time is 90 ms. Hydrogen fuel jet exit velocity is 47 m/s, and the co-flow air velocity is 0.57 m/s. Reynolds number is 837. Fig. 13 shows that pure hydrogen (UHP grade) emits bluish and reddish colour in the diffusion flame.

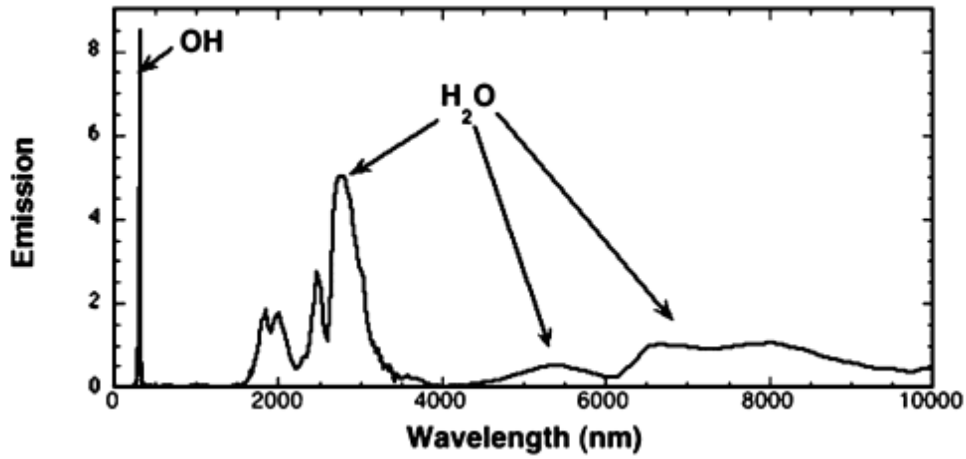

Fig. 14: Emission spectra in typical diffusion H_2-air jet flame [36].

Fig. 14 indicates that OH molecules have strong emissions in the ultraviolet range. Besides, H_2O provides strong emission bands at 1800 nm, 2700 nm and 6300 nm, which are in the infrared range.

Apart from the diffusion flame, the premixed hydrogen-air flame also shows visible colours. In Shefer's research [36], different equivalence ratios of the hydrogen-air mixture are tested. Fig. 15 shows a Flame luminescence photographs of premixed $\boldsymbol{H_2}$-air jet with different equivalence ratio. The result indicates that the colour of the premixed hydrogen-air flame depends on the equivalence ratio. With the increase of equivalence ratio, the red colour is more distinct at downstream of flame. The blue colour appears at the upstream of flame at all equivalence ratios.

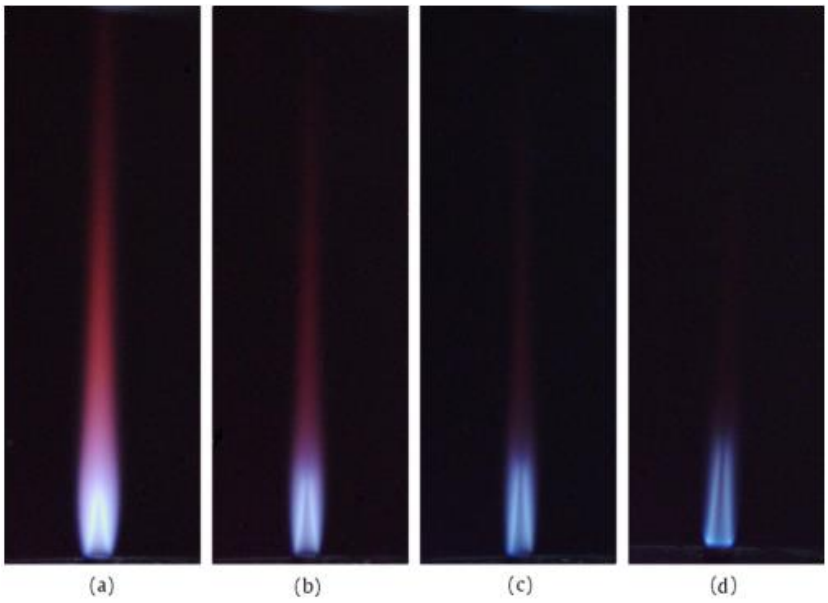

Fig. 15: Flame luminescence photographs of premixed H_2-air jet. (a) $\phi = 1.0$; (b) $\phi = 0.8$; (c) $\phi = 0.7$; (d) $\phi = 0.62$. Aperture f/2.4 with 4 s exposure time. Jet velocity is 33 m/s. Reynolds number = 580 [36].

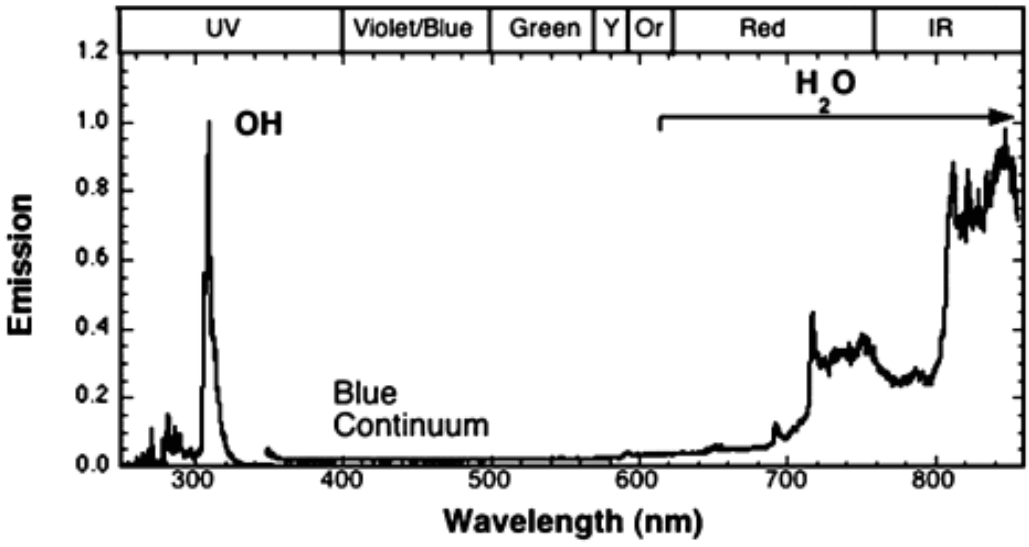

Fig. 16: Emission spectra in typical premixed H_2-air jet flame [36].

Fig. 16 shows that OH molecules have a strong emission band in the premixed flame spectrum similar to hydrogen diffusion flame. H_2O contributes strong emission in the infrared range, which is similar to the diffusion flame spectrum. Apart from OH

and H_2O molecules, a continuous blue emission exists in the range between 350 nm to 600 mn. Therefore, Schefer concluded that the colour of hydrogen flame is caused by the "blue continuum" emission [36].

However, the "blue continuum" may explain emission bands in the blue region, but the reddish colour of hydrogen diffusion flame is still not well addressed.

2.5.4.2 Sodium contamination

Another common explanation for hydrogen diffusion flame colour is sodium contamination in the surrounding air.

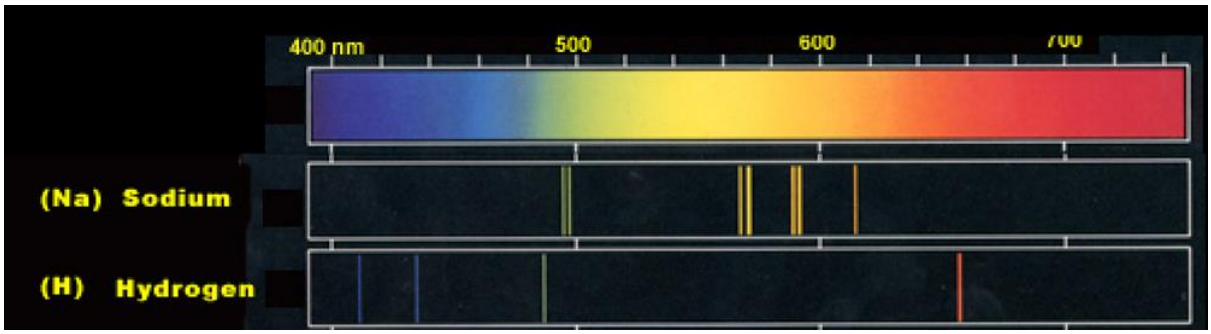

Fig. 17: Comparison of sodium and hydrogen emission spectrum [37].

Sodium has strong emission bands in the visible range, as shown in Fig. 17 and Fig. 19. The two characteristic spectral lines of sodium are known as 'Sodium Doublets'. The occurrence of sodium double lines is due to electron transition from different states. The transition from $P_{3/2}$ state to S state emits the line at 588.99 nm and the transition from $P_{1/2}$ state to S state emits the line at 589.59 nm [38], which is in the yellow colour range.

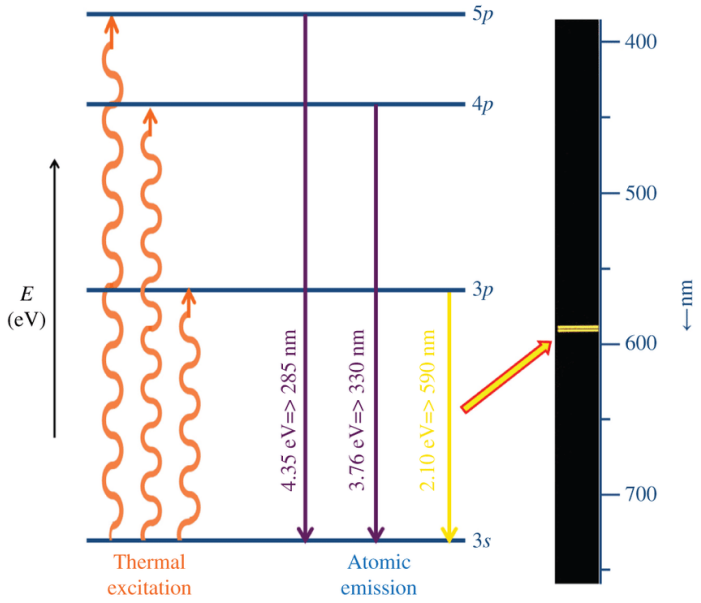

Fig. 18: Atomic emission of sodium [39] [40].

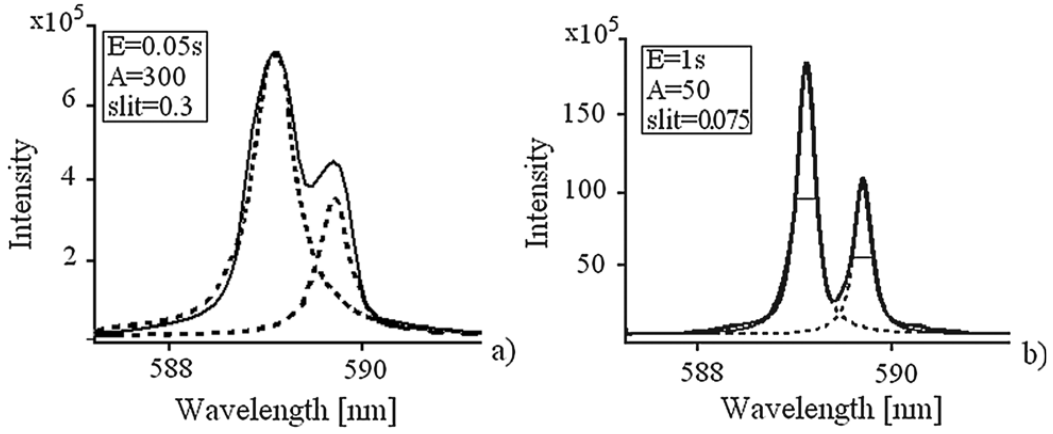

Fig. 19: Intensity measurement of Sodium doublet lines emitted from a short lifetime palsma with different exposure time E, slit widths and accumulation A [41].

Sodium contamination may explain the yellow flame in some cases of hydrogen diffusion flame, for example, the launch of the NASA Delta IV rocket (Fig. 20). The launch site is close to the sea-coast; hence it is reasonable to have a large amount of sodium in the air. In addition, the ablative coating and the carbon contained nozzle of

the rocket [42] might have influence on the flame colour under a high temperature.

Fig. 20: NASA Delta IV rocket launch [43].

Furthermore, Fig. 21 is a raw spectrum of a meteor captured in 2018. It could be noticed that the sodium line in the meteor spectrum is intense [44]. It might be due to the large amount of sodium in the meteor composition, or it might be caused by the sodium in the atmosphere.

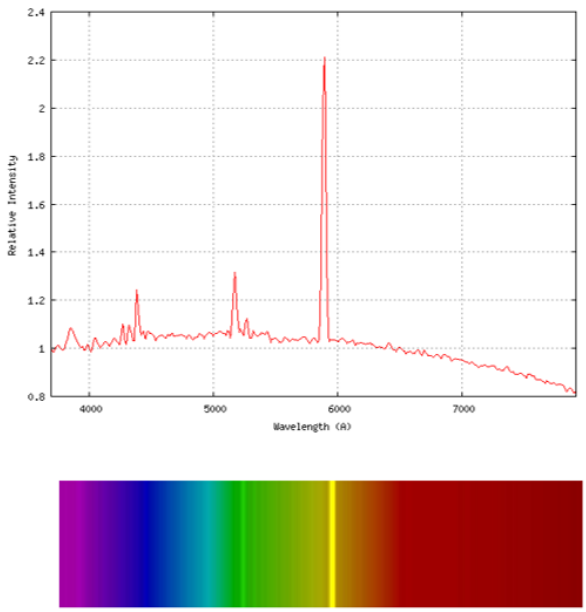

Fig. 21: Raw spectrum of a meteor captured in 2018 with intense sodium emission line [44].

2.5.4.3 Water vibration-rotation bands

An alternative potential cause of the faint colour of hydrogen flame can be due to the existence of water vapour, which is produced during the combustion process. Referring to Kitagawa, water vapour has vibration-rotation absorption bands in the visible range, and some of them are in proximity to the hydrogen emission band [45].

T. Kitagawa captured the spectrum of oxy-hydrogen flame with a glass spectrograph. The research indicates there are some weak emission bands in the range of $360\ \text{nm}$ to $500\ \text{nm}$. The spectrum also shows the existence of a large number of strong emission bands between $550\ \text{nm}$ and $700\ \text{nm}$ [46].

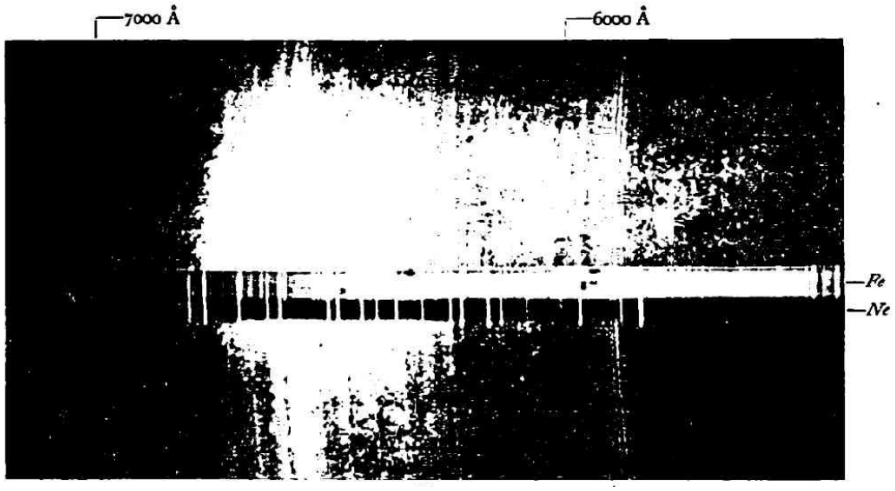

Fig. 22: The emission bands of oxy-hydrogen flame [46].

Oxygen involved in the hydrogen flame spectrum taken by Gaydon (Fig. 23) in the range of 610 nm to 730 nm showed clear emission band heads at around 645 nm and 652 nm. He also suggested that these bands were generated by the vibration-rotation bands of water [47].

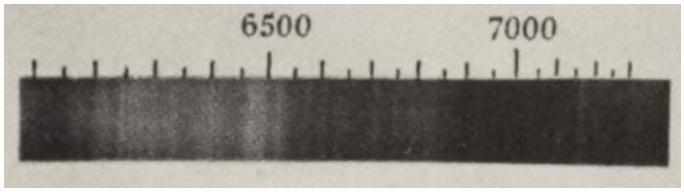

Fig. 23: Flame spectrum of oxygen burning in hydrogen in the range of 610 nm to 730 nm [47].

A water molecule is made of an oxygen atom and two hydrogen atoms. Due to the isosceles triangular molecular structure, as shown in Fig. 24, the water molecule has three freedoms of vibration [48].

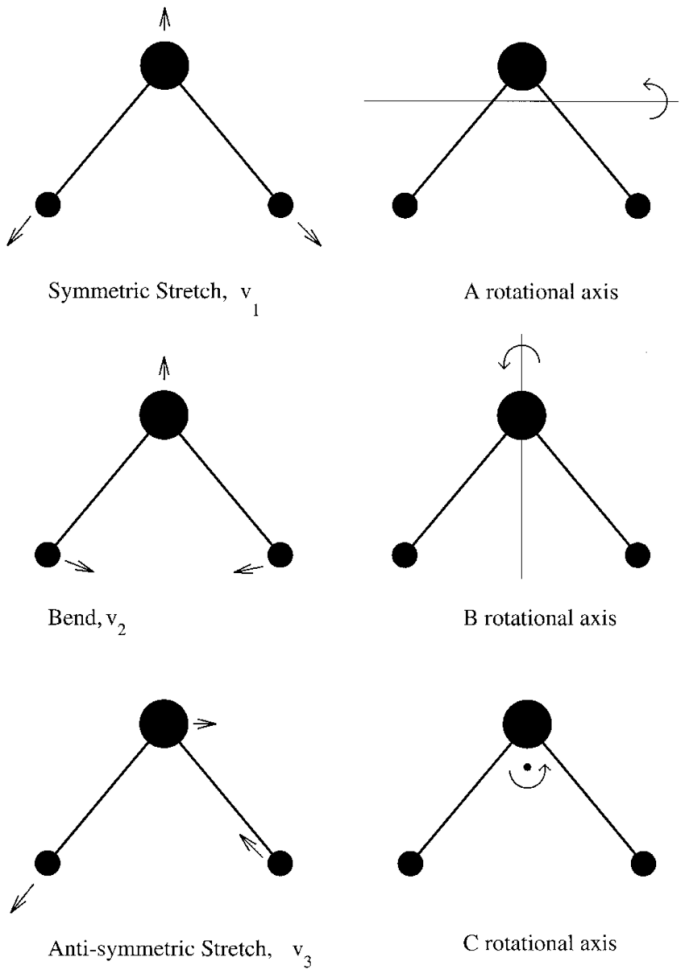

Fig. 24: Water molecule vibrational and rotational motions [48].

According to the research by Mecke, Baumann and Freudenberg, the three fundamental vibrations are $\upsilon(\sigma)$, $\upsilon(\pi)$ and $\delta(\pi)$, and V_σ, V_π and V_δ represent their vibrational quantum numbers. There are a total of 6 water vapour vibrational rotational bands in the wavelength range of 570 nm to 700 nm.

No.	Vibrational State $(\upsilon(\sigma), \upsilon(\pi), \delta(\pi))$	Wavelength (nm)	Wavenumber (cm^{-1})	Vibrational energy, KCal
1	(3, 2, 0)	571.4	17495.44	49.7
2	(1, 4, 0)	591.6	16898.81	48.0
3	(1, 3, 2)	594.3	16821.62	47.8
4	(3, 1, 1)	631.4	15832.47	45.0
5	(1, 3, 1)	651.4	15347.90	43.6
6	(3, 1, 0)	698.2	14318.73	40.7

Table. 2: The vibrational rotational band of water vapour in the range of 570 nm to 700 nm [46].

T. Kitagawa also listed the wavelength and wavenumber of the emission bands of the oxy-hydrogen flame in the range of 565 nm to 700 nm.

No.	Wavelength (λ, nm)	(υ, cm^{-1})	No.	Wavelength (λ, nm)	(υ, cm^{-1})
1	568.33	17590	13	622.00	16072
2	571.53	17492	14	625.51	15982
3	580.69	17215	15	632.16	15815
4	586.16	17056	16	637.71	15676
5	588.02	17001	17	645.75	15482
6	590.02	16943	18	646.80	15456
7	592.38	16878	19	649.04	15404
8	594.88	16807	20	651.68	15340
9	598.88	16692	21	657.45	15207
10	616.57	16215	22	662.86	15083
11	618.15	16173	23	692.20	14443

12	620.26	16119	

Table. 3: The wavelength and wavenumber of oxy-hydrogen flame in the range of 565 nm to 700 nm recorded by Kitagawa [45].

Theoretically, water vapour is the only product of oxy-hydrogen flame, and it has strong emission bands in infrared. It is possible that water also has emission bands in the visible light range.

Hence, the vibration-rotation bands of water are compared with the oxy-hydrogen flame emission bands.

Absorption spectrum of the vibration-rotation bands of water vapour				**Emission bands of the oxy-hydrogen flame**			
No.	λ, nm	**Intensity**	v, cm^{-1}	**No.**	λ, nm	**Intensity**	v, cm^{-1}
1	588.06	6	17001	5	588.02	6	17001
2	591.42	4	16903	7	592.38	4	16878
3	594.30	6	16821	8	594.88	6	16807
4	651.74	10	15340	20	651.68	10	15340

Table. 4: Comparison of absorption bands of the water vibration-rotation bands and emission bands of the oxy-hydrogen flame [47].

Four emission bands in the red light range match the vibration-rotation bands of water. Hence, the reddish colour of diffusion hydrogen flame may be caused by the absorption bands of water vapour. However, there is no clear evidence that water vapour can emit visible lights in combustion.

2.5.4.4 $H-\alpha$ transition

The presence of the hydrogen spectrum is also a possible cause of the reddish flame colour of hydrogen. In detail, such a spectrum is relatively close to the proverbial sodium colour, which may overshadow the reddish colour. As a possible reason for such reddish colour appearing in blue hydrogen flame, the may be considered based upon the Bohr atom model.

A hydrogen atom contains a proton and an electron. When hydrogen gas is heated up, the electron in the atom absorbs the energy and is excited. Hence the electron jumps to other states from its ground state. However, the electron is not very stable in other states. Thus, the electron will fall back to the ground state after a short time. It requires the least energy for the electron to stay in the ground state. Therefore, energy will be released when the electron falls back to the ground state. When the electron energy level of hydrogen falls from n = 3 to n = 2, it will be emitted in visible red light colour (656.28 nm) [5] and possibly contribute to the reddish colour of a hydrogen flame. Fig. 25 shows photoelectric effect of an atom.

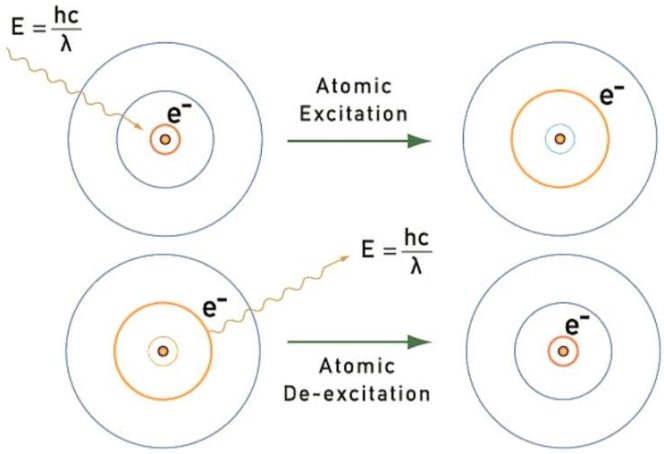

Fig. 25: Photoelectric effect of an atom [50].

When the electron falls back from n=3 state to n=2 state, a 656.3nm wavelength spectral line in the Balmer series, this light is identified as Hydrogen-alpha $(H-\alpha)$ light [5].

The following figure (Fig. 26) shows the different series of hydrogen electron transitions.

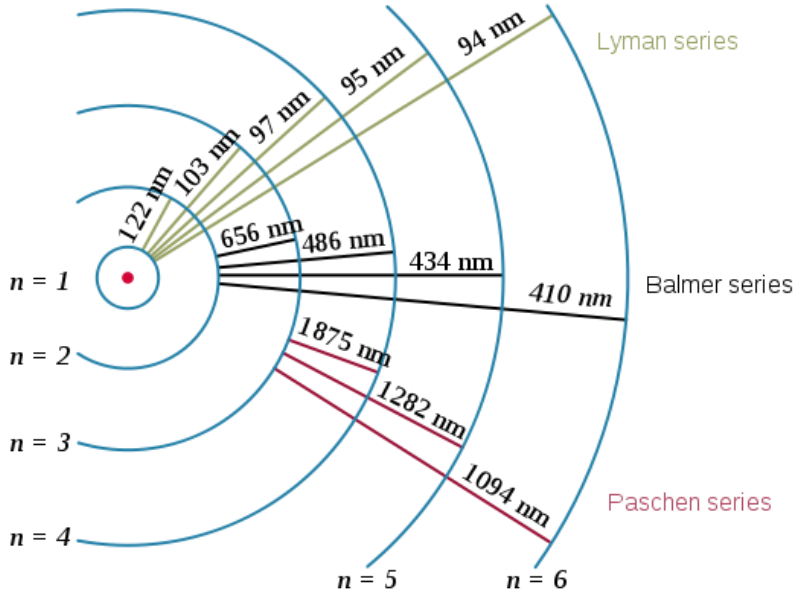

Fig. 26: Hydrogen electron transitions and their resulting wavelengths [50].

According to the spectrum, hydrogen-alpha light has a visible red colour. The flame of hydrogen ignition has a similar colour to the hydrogen alpha light, which leads to the motivation of this project.

Moreover, the emission spectrum of hydrogen shows there are five distinct emission lines in the visible range. As Fig. 27 shows, four of them are in the range of violet and blue colour range, while only one line is in the red light range.

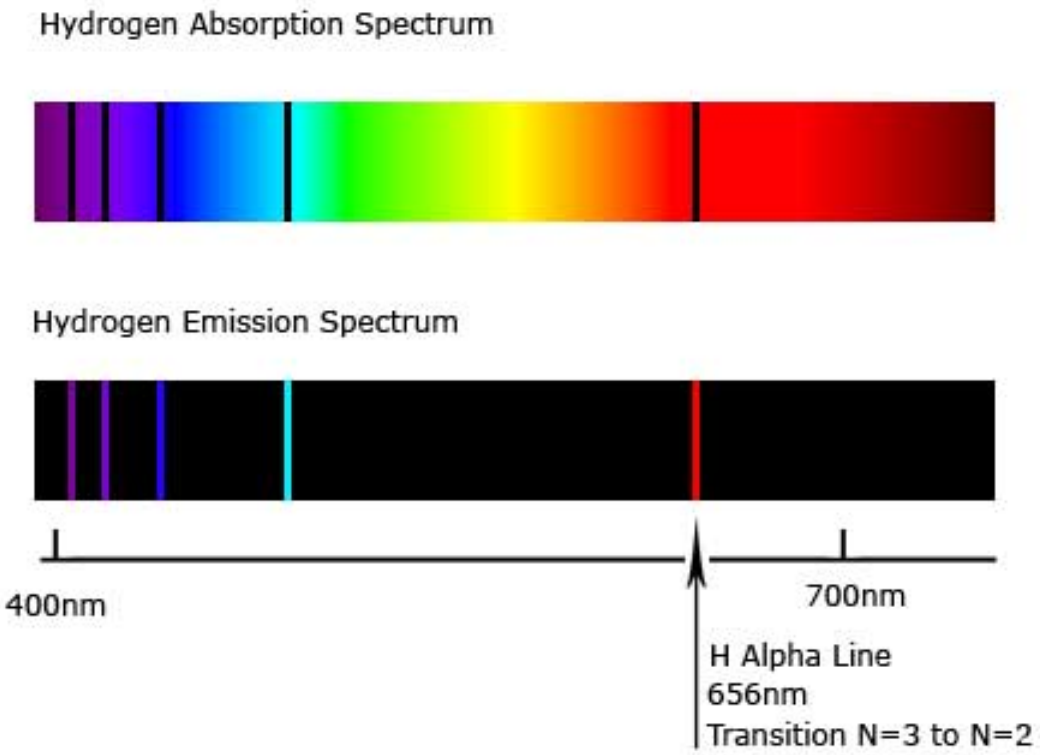

Fig. 27: Hydrogen absorption and emission spectrum [51].

2.6 Visualization methods for combustion research

Visualization of combustion is critical in the research, especially in the area of flame colour. For example, the optical spectrometer is used for flame colour research, and the schlieren imaging system could capture the detailed fluid dynamic during combustion. In this section, optical spectrometer, digital camera and schlieren imaging technique used in the combustion research areas will be discussed.

2.6.1 Schlieren imaging technique

2.6.1.1 Fundamental of Schlieren imaging technique

Quoting Hubert Schardin's words, 'The basic principle of the schlieren technique is the combination of the optical projection of an object with an indication of its light deflection.' [52].

When light propagates in inhomogeneous transparent media, the reflective difference within the overall background is defined as 'schlieren' [52]. Flow density change can lead to the occurrence of schlieren, and a change in flow density could be caused by temperature or velocity difference. Refracting light rays are the basic of the schlieren technique. The mathematical basis behind it is demonstrated below:

The refractive index (n) describes the direction change of the light rays when passing through a media. It could be defined mathematically as:

$$\boldsymbol{n = \frac{c_0}{c}} \qquad \textbf{Equation. 4}$$

Where c is the speed of light travels in the media,

c_0 is the speed of light travels in vacuum (approximately $3 \times 10^8 ms^{-1}$).

Defining x, y, z as the normal cartesian coordinates of a system. Then the bending light ray is proportional to the gradients of refractive index in x, y plane.

As shown in Fig. 28, assuming the refractive index gradience is negative. A planar wavefront passing through z_1, and propagating to z_2.

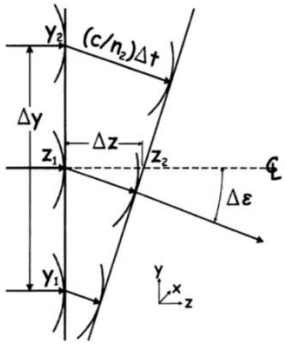

Fig. 28: Diagram of elemental light refraction by $\frac{dn}{dy}$ [52].

The differential angle $\Delta\boldsymbol{\varepsilon}$ could be expressed as:

$$\Delta\boldsymbol{\varepsilon} = \frac{(\boldsymbol{c_0/n_2 - c_0/n_1})}{\Delta\boldsymbol{y}} \times \Delta\boldsymbol{t} \qquad \textbf{Equation. 5}$$

Where, n_2 and n_1 are different refractive index due to the negative refractive index gradient,

Δt is the differential time.

$$\Delta\mathbf{t} = \Delta\mathbf{z} \times \frac{\mathbf{n}}{\mathbf{c_0}} \qquad \textbf{Equation. 6}$$

Combining Equation. 5 and Equation. 6, the differential angle is:

$$\Delta\boldsymbol{\varepsilon} = \frac{\boldsymbol{n}}{\boldsymbol{c_0}} \times \frac{(\boldsymbol{c_0/n_2 - c_0/n_1})}{\Delta\boldsymbol{y}} \times \Delta\boldsymbol{z} \; = \frac{\boldsymbol{n}}{\boldsymbol{n_1 n_2}} \times \frac{(\boldsymbol{n_1 - n_2})}{\Delta\boldsymbol{y}} \times \Delta\boldsymbol{z} \qquad \textbf{Equation. 7}$$

When Δy approaches to 0, hence $\frac{n}{n_1 n_2}$ turns to be $\frac{1}{n}$. Differentiate $\Delta\varepsilon$ in terms of Δz, then:

$$\frac{\boldsymbol{d\varepsilon}}{\boldsymbol{dz}} = \frac{\mathbf{1}}{\boldsymbol{n}} \times \frac{\boldsymbol{dn}}{\boldsymbol{dy}} \qquad \textbf{Equation. 8}$$

Due to ε is a very small angle, thus

$$\boldsymbol{\varepsilon \approx \frac{dy}{dz}} \qquad \textbf{Equation. 9}$$

Substitute Equation. 9 into Equation. 8, it would be:

$$\boldsymbol{\frac{\partial^2 y}{\partial z^2} = \frac{1}{n} \times \frac{\partial n}{\partial y}} \qquad \textbf{Equation. 10}$$

Equation. 10 is the expression of the refracted ray curvature.

Similarly,

$$\boldsymbol{\frac{\partial^2 x}{\partial z^2} = \frac{1}{n} \times \frac{\partial n}{\partial x}} \qquad \textbf{Equation. 11}$$

Equation. 10 and Equation. 11 are the mathematical core of schlieren imaging technology [52].

The first schlieren method was developed by Robert Hooke in the 17th century. Fig. 29 shows Hooke's original schlieren system setup. This setup only contains two candles, a lens and human eyes [52].

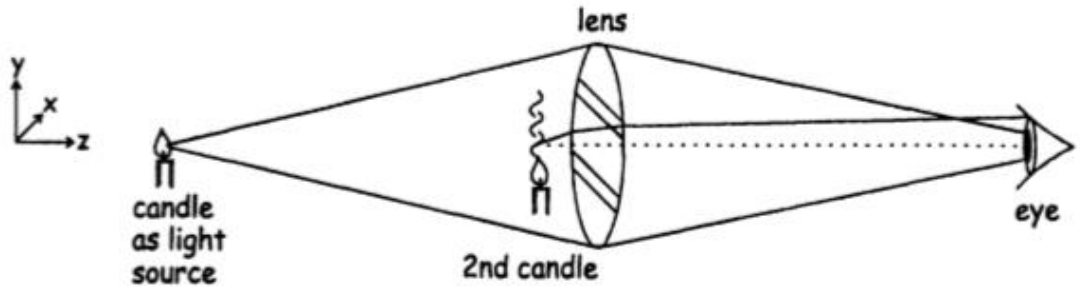

Fig. 29: Hooke's original schlieren system setup [52].

The first candle is used as a light source, and the image of the second candle

flame is projected on the human pupil by the lens. Some intense light rays are refracted, fall outside the pupil, and are blocked. Therefore, the intensity difference seen by the human eye could reveal the transparent plume of the candle flame.

In the 19th century, August Toepler designed the first proper schlieren setup, including a lantern light source, an adjustable knife-edge, a telescope and a long-focus lens [52]. Fig. 30 is the Toepler's schlieren setup.

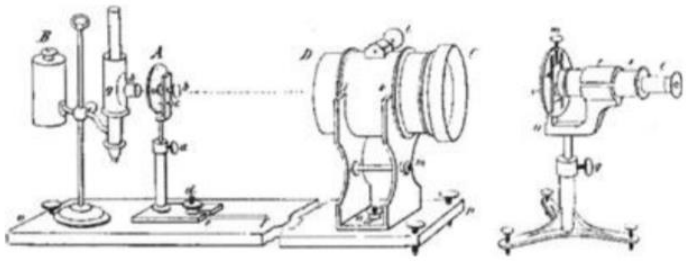

Fig. 30: Toepler's schlieren setup [52].

With this proper schlieren setup, Toepler observed sound shock waves. The image below (Fig. 31) is a drawing of the schlieren image showing a spherical shock wave propagating from the electrical spark. Hence, August Toepler was honoured as the first who saw sound [52].

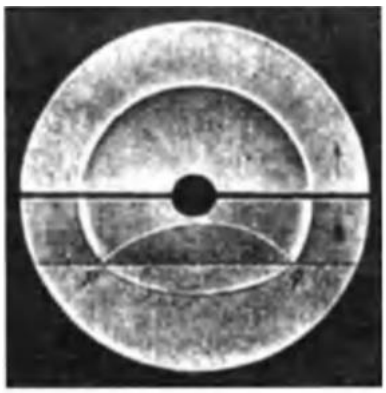

Fig. 31: Shock wave from an electrical spark in the air [52].

In the 20th century, the schlieren imaging technique was further developed to explore the motivation of shock in the air and study fluid dynamics.

Nowadays, the application of the schlieren imaging technique has a much more comprehensive range. It includes application in research of the phenomenon in solids, liquids and gases, combustion, material processing, microscopy, etc. [52].

2.6.1.2 Typical schlieren setups

There are various setups of the schlieren imaging technique for different purposes. In the research of combustion, Z-type Schlieren and single mirror schlieren are the most common setups.

Z-type schlieren system

Z-configuration parallel-light schlieren is the full name of the Z-type schlieren system. This setup contains a point light source, two parallel mirrors, a knife-edge and a digital camera. The point source is formed of a light, a condenser lens and a slit. The distance between the light source and mirror A is the focal length of the mirror. Lightray goes through the slit and is refracted by mirror A. The bent ray passes through the field of interest, and mirror B bends the light ray towards the digital camera. The distance between the two mirrors should be at least twice the focal length of the mirror. According to research, there is no apparent influence if the distance between the two mirrors is longer. A knife-edge is placed at the focal point to block part of the light [53]. Fig. 32 shows a typical Z-type schlieren system setup.

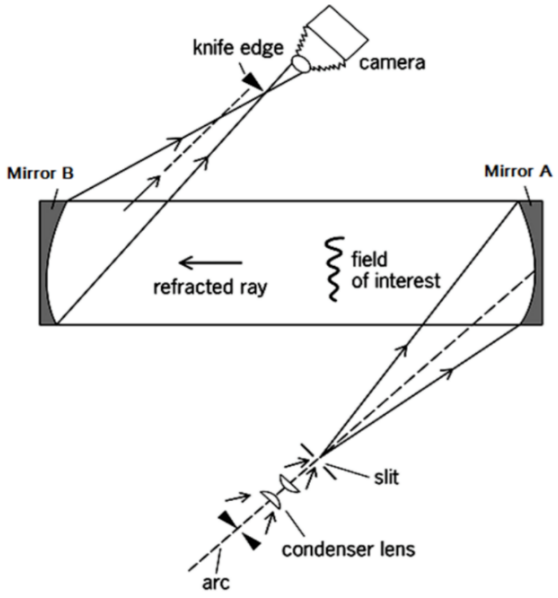

Fig. 32: Typical Z-type schlieren system setup [52].

Single mirror schlieren system

In terms of apparatus, the difference between the single mirror schlieren system with the Z-type setup is the number of mirrors and an additional beam splitter. As Fig. 33 shows, the testing area is in front of the mirror, and therefore, light rays pass through the testing area and are refracted directly by the mirror [54].

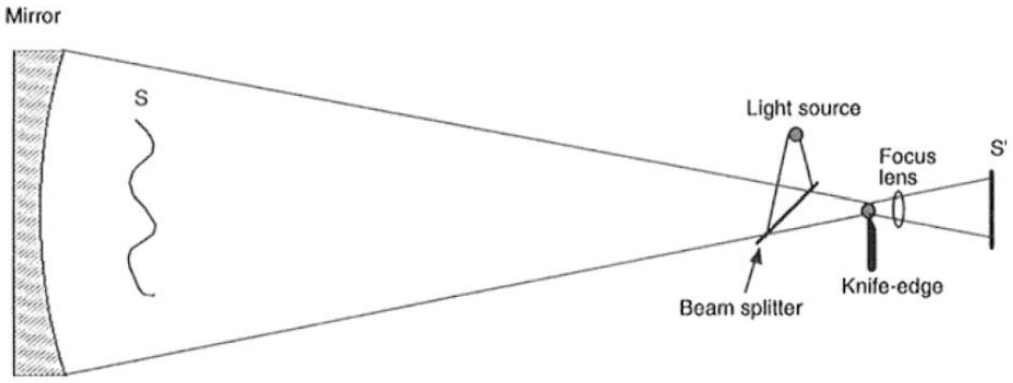

Fig. 33: Single mirror schlieren system setup [54].

Comparing To the Z-type schlieren system, the single mirror schlieren is more

sensitive, and the cost is cheaper. However, the Z-type schlieren system is more operational in a practical experiment.

2.6.2 Optical Spectrometer

The spectrum was firstly used to describe the dispersion phenomenon when white light passed a prism by Issac Newton in the 17th century [55]. A spectrometer is a device that measures the spectrum. The optical spectrometer is a device that measures the emission, absorption or fluorescence spectrum of a material [56].

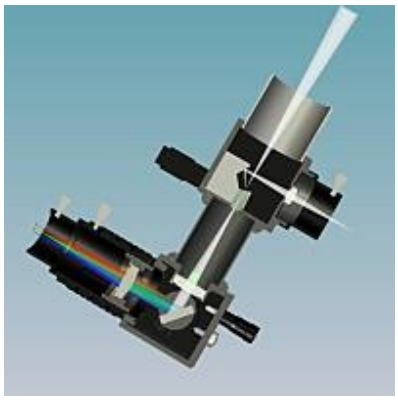

Fig. 34: DADOS slit spectrograph [57].

The spectral line is where the intensity of the local spectrum is higher. It is in the shape of a line due to it is the image of the slit.

There are several different optical spectrometers, including prism spectrometer, grating spectrometer, the Fourier-transform spectrometer, Fabry-Perot spectrometer, laser spectrometer etc. The grating spectrometer will be mainly discussed in this report.

A grating spectrometer uses the grating to disperse the light [56]. The figure below (Fig. 35) shows the layout of a diffraction grating spectrometer.

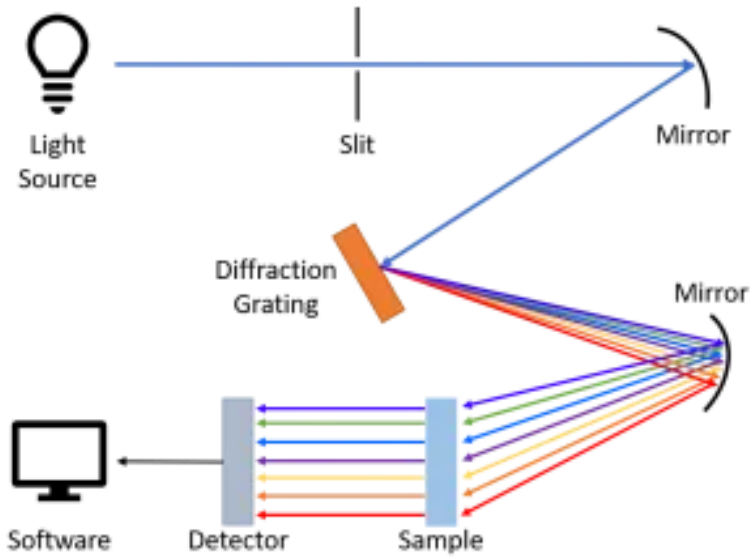

Fig. 35: Layout of a diffraction grating spectrometer [58].

A typical diffraction grating spectrometer includes an input slit, a diffraction grating, an output slit, a detector (light sensor) and some lenses. The light is convexed to go through the input slit, then passes the lense and diffracted by the diffraction grating. Finally, it is convexed again, passes the output slit, and reaches the detector. A spectrum of the light will then be projected on the detector.

As the most crucial part of the spectrometer, the diffraction grating has two main types. One is called reflection grating, and the other one is transmission grating. Both of them are plane gratings. Fig. 36 is the schematic diagram of the two types of plane diffraction gratings.

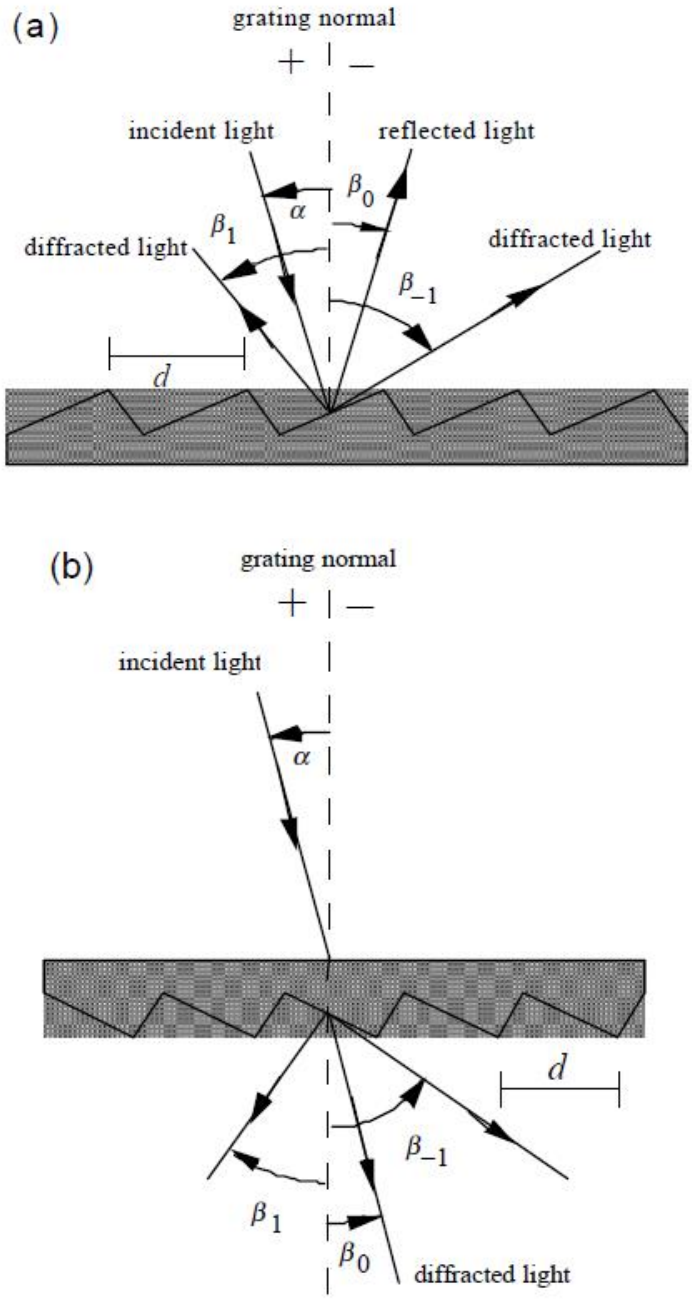

Fig. 36: Diffraction by a plane grating. (a) A reflection grating. (b) A transmission grating [59].

The difference between a reflection grating and a transmission grating is whether the incident and diffracted light rays lie on the same side of the grating.

In the figure, α is the incident light angle.

β_m is the diffraction light angle, where the subscript *m* represents the order of diffraction.

d is the groove spacing, also known as the pitch.

The following grating equations express the relations between the angles and the light wavelength:

$$\mathbf{m\lambda = d(sin\alpha + sin\beta)} \qquad \textbf{Equation. 12}$$

$$\mathbf{Gm\lambda = sin\alpha + sin\beta} \qquad \textbf{Equation. 13}$$

$$\mathbf{G = 1/d} \qquad \textbf{Equation. 14}$$

Where λ is the wavelength of the incident light.

G is the groove frequency/density, or "grooves per millimetre".

m is an integer multiple.

Equation. 12 and Equation. 13 can only be applied when the incident and diffracted light are both perpendicular to the grooves. In other cases, the equation is modified as below:

$$\mathbf{Gm\lambda = cos\varepsilon(sin\alpha + sin\beta)} \qquad \textbf{Equation. 15}$$

ε is the angle between the plane perpendicular to the grooves and the path of the incident light.

When $\varepsilon \neq 0$, the case is defined as conical diffraction [59].

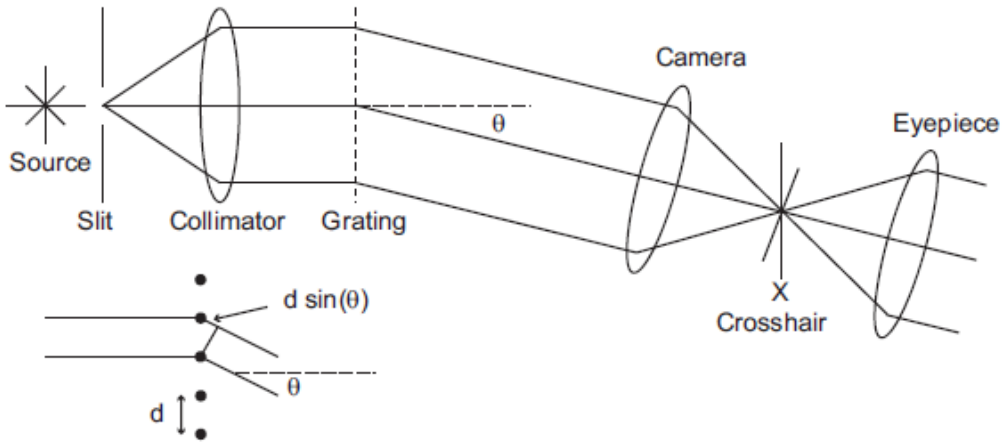

Fig. 37: The schematic diagram of the planar diffraction grating spectrometer [60].

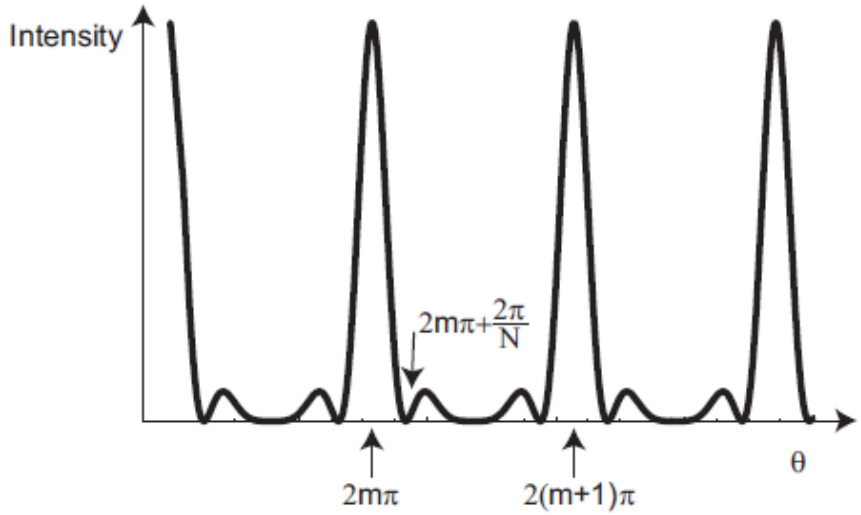

Fig. 38: The diffraction pattern for N=4 slits [60].

According to the diffraction spectrometer theory, the phase difference between two adjacent light paths could be calculated as:

$$\textbf{phase difference} = \textbf{path difference} \times \frac{2\pi}{\lambda} = 2\pi m \qquad \textbf{Equation. 16}$$

$$\textbf{path difference} = d\sin\theta \qquad \textbf{Equation. 17}$$

Hence, Equation. 16 becomes:

$$\frac{2\pi}{\lambda} dsin\theta = 2\pi m$$ **Equation. 18**

Simplified as:

$$\mathbf{dsin\theta = m\lambda}$$ **Equation. 19**

θ is the diffraction angle of the light.

The resolving power of a diffraction spectrometer is the ability of the grating to distinguish the difference between two adjacent spectral lines.

$$\mathbf{R} = \frac{\boldsymbol{\lambda}}{\Delta\boldsymbol{\lambda}}$$ **Equation. 20**

Where R is the resolving power.

$\Delta\lambda$ is the limit of resolution.

The resolving power is limited by the difference of wavelengths of two equal intensity lines that could be separated.

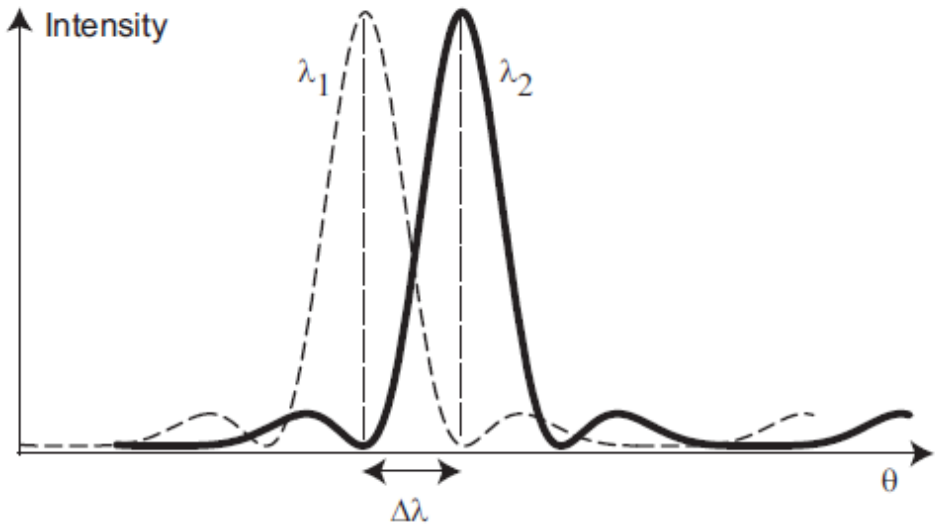

Fig. 39: Resolution of a diffraction grating [60].

The relationship between the phase angle of the first minimum (ϕ) and the number of illuminated slits (N) is expressed as:

$$\boldsymbol{\phi = 2\pi m + \frac{2\pi}{N}} \qquad \textbf{Equation. 21}$$

Also, the resolving power can be worked out when the minimum of one diffraction pattern and the maximum of another diffraction pattern is at the same place.

As shown in Fig. 39,

$$\boldsymbol{\lambda_2 = \lambda - \Delta\lambda} \qquad \textbf{Equation. 22}$$

The minimum occurs at the angle θ when it satisfies:

$$\boldsymbol{\frac{2\pi}{\lambda_2} d\ sin\theta = 2\pi m + \frac{2\pi}{N}} \qquad \textbf{Equation. 23}$$

Simplified as

$$\boldsymbol{d sin\theta = m\lambda_2 + \frac{\lambda_2}{N}} \qquad \textbf{Equation. 24}$$

Combining Equation. 19 and Equation. 24, it becomes:

$$\boldsymbol{m\lambda = m\lambda_2 + \frac{\lambda_2}{N}} \qquad \textbf{Equation. 25}$$

As $\Delta\lambda$ is far smaller than λ, the theoretical value of the resolving power of a planar diffraction grating is given by [60]:

$$\boldsymbol{R = \frac{\lambda}{\Delta\lambda} = mN} \qquad \textbf{Equation. 26}$$

2.6.3 Camera

The history of the camera can be traced back to the 1820s. The first 'photo' was captured by Joseph N. Niepce in 1827. Then in 1837, Daguerre invented the first camera, which could capture clear black and white images. The camera was made of a wooden box and a lens. However, the camera could not copy the image [61].

Fig. 40: The camera invented by Daguerre in 1837 [61].

Willam Henry Fox Talbot improved and invented the calotype camera in 1839. The calotype camera can record the original image with its negative image on paper. Then the positive image could be obtained by shining light through the negative image. The advantage of this type of camera is that it can make copies of the original image [61].

Fig. 41: Negative and positive images [62].

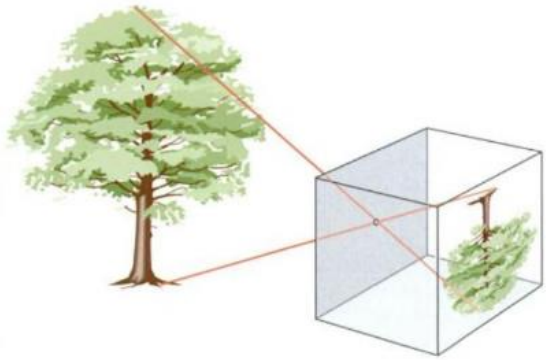

Fig. 42: The working principle of camera [63].

When the reflected light of an object passes the pinhole, an upside-down image of the object will be cast onto the wall of the black box. This optical principle is the basic operation principle of the camera [63].

2.6.3.1 Film camera

A traditional film camera, as its name suggests, uses film to capture images. The film was made of plastic and plated with a silver halide crystal layer. Different colour sensitive layers will be applied in a colour film. Typical layers including a blue sensitive layer on the top, a yellow filter layer, followed by a green-blue sensitive layer and a red-blue sensitive layer. When the film is exposed to light, a chemical reaction will be triggered, and a latent image is captured. Then the latent image can be developed into a negative by convert the silver halide into metallic silver. Then the negative could be reversed to a positive image [64] [65].

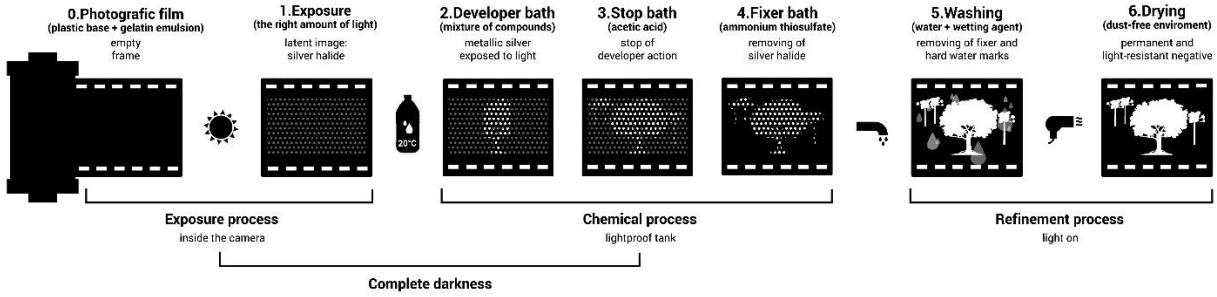

Fig. 43: Film developing process [66].

Comparing with digital camera, film camera has a better performance in black-and-white images. It has a higher light and dark variation; hence more details can be recorded in black and white photography [67]. However, a film camera would take a much longer exposure time than a digital camera when the light intensity is low. Moreover, the film camera could not change the white balance, which cause the colour of the image varies with the brands of the film [68].

2.6.3.2 Digital camera

With the development of digital technology, the digital camera has been taking the place of the traditional film camera in recent days. A digital camera uses electronic sensors to record the incoming lights and store the image into a digital computer file. When the shutter button is pressed, sensors inside the digital camera record the colour sensed by each pixel. The electronic image sensor has two main types: the charge-coupled device (CCD) and the complementary MOS sensor (CMOS).

CCD Sensor

CCD is the abbreviation of Charge-Couple Device. It was invented by W. S. Boyle and G. E. Smith at Bell Telephone Laboratories in 1969 [69]. The technology of CCD is

based on the metal-oxide-semiconductor (MOS). When an image is projected onto the capacitor array, photons are converted into electrons, and an electric charge accumulates on the capacitors. The electric charge on each capacitor is proportional to the intensity of light incidence. Then each capacitor would transfer its charge to the neighbour capacitor. This transfer process is controlled by a control circuit. Once the last capacitor receives the charge, it moves the charge to a charge amplifier and an analog-digital converter (ADC). The charge would then be converted into a voltage and stored in the digital camera memory.

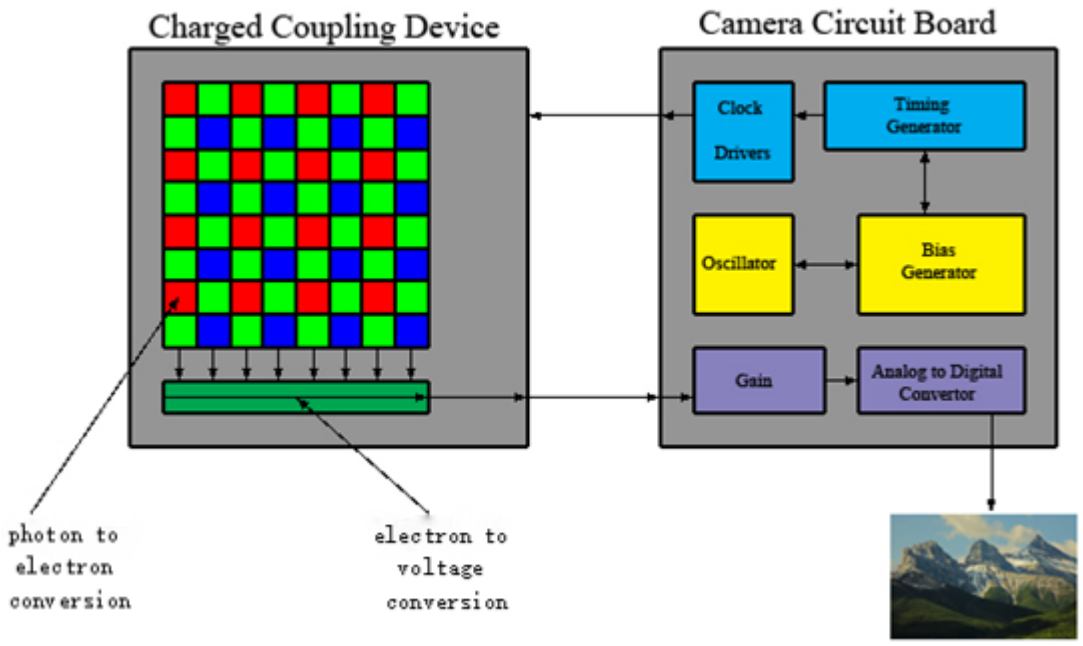

Fig. 44: CCD working principle [70].

CMOS sensors

CMOS stands for Complementary metal-oxide-semiconductor. It was invented by C. T. Sah and F. Wanlass of the Fairchild R & D Laboratory in 1963 [71]. The main difference between CMOS and CCD sensors is that each pixel has an amplifier in CMOS sensors. Besides, each column of capacitors has its own analog-digital

converter, and each pixel can be accessed individually.

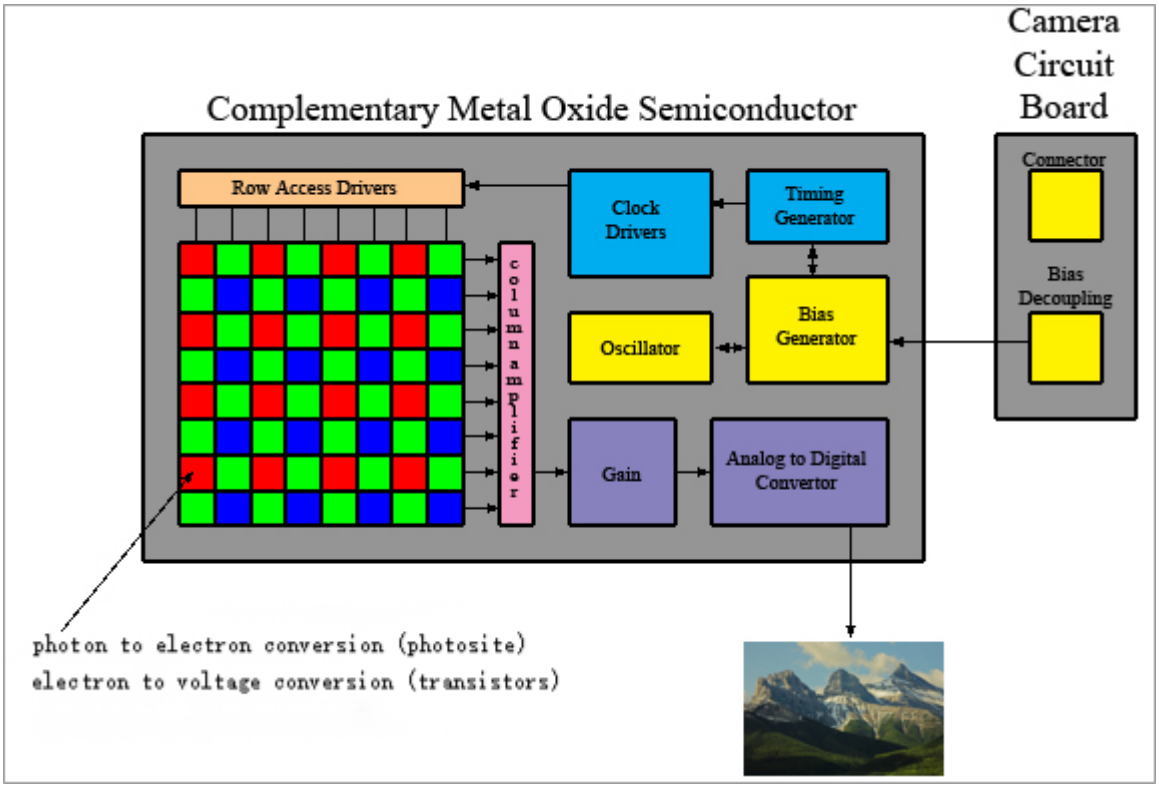

Fig. 45: CMOS sensor working principle [70].

Both CCD and CMOS sensors are based on the same method of converting light photons into an electrical signal. These two sensors have their own advantages and disadvantages. Comparing a modern CMOS sensor with a traditional CCD sensor, the modern CMOS sensors have a relatively lower sensitivity due to the multi-layer semiconductor materials. CMOS sensors also have a higher noise level due to the unevenness caused by the individual amplifier for each pixel. Fig. 46 is a signal to noise ratio (SNR) comparison of an IMX249 CMOS sensor and an ICX414 CCD sensor under low light conditions. It could be known from the figure that the CMOS sensor has a higher SNR than the CCD sensor at a low light level. However, at high lighting levels, the CMOS sensor has higher signal production than CCD sensors [72].

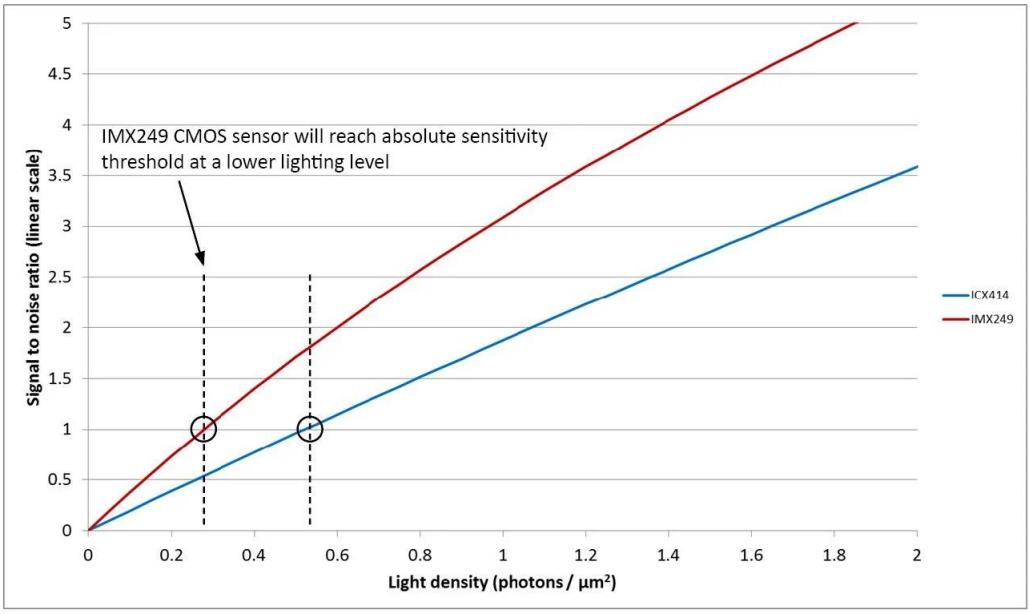

Fig. 46: IMX249 CMOS and ICX414 CCD sensors signal to noise ratio comparison under low light conditions [72].

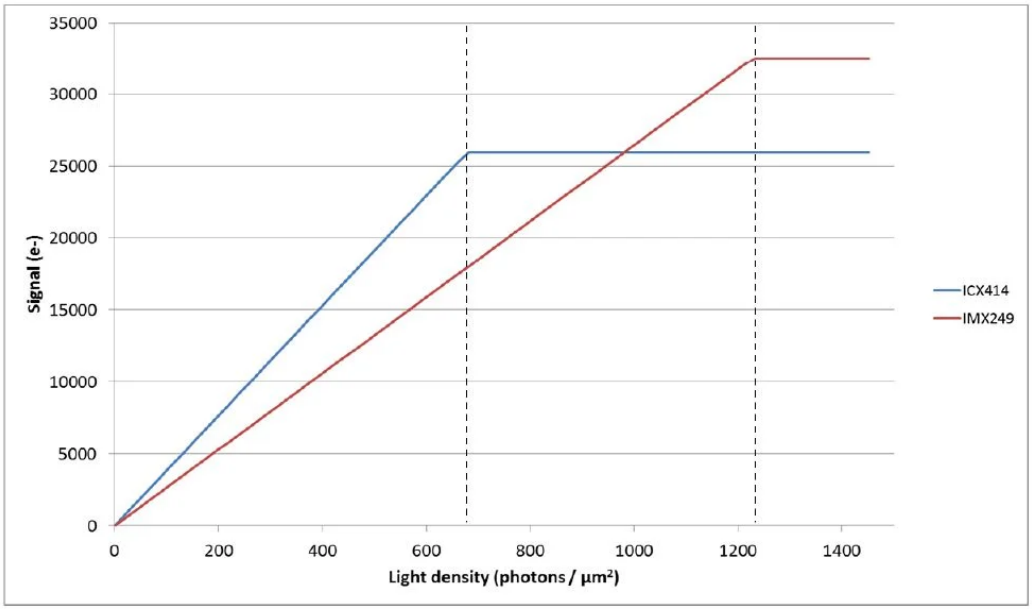

Fig. 47: IMX249 CMOS and ICX414 CCD sensors signal [72].

Besides, the CCD sensor would reach its saturation capacity at a lower light density compared to the CMOS sensor. Therefore, the CCD sensor camera would generate a brighter image than the CMOS sensor camera [72].

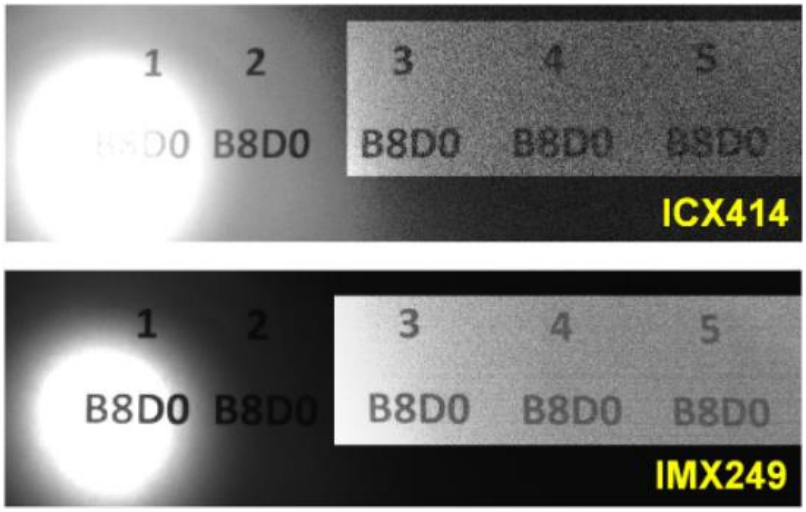

Fig. 48: Images captured by ICX414 CCD sensor and IMX249 CMOS sensor under different lighting conditions (the dark lighting conditions are enhanced for display) [72].

It could be noticed from the results in Fig. 48 that the CMOS sensor shows more details of the image compared to the CCD sensor. Under the high lighting levels, the image captured by the CCD camera is saturated, and the information can hardly be seen. While under the low lighting conditions, the noise level in the CCD sensor image is higher than the CMOS sensor image. Therefore, according to this report, the performance of modern CMOS sensors is better than the traditional CCD sensor under various lighting conditions [72].

2.6.3.3 RGB colour model

RGB colour model is commonly used in describing the colour in digital images. It enables different digital devices to know the colour information of images [73]. RGB is the initials of red, green and blue primary colours, respectively. A variety of colours could be obtained by adding these three colours in different proportions.

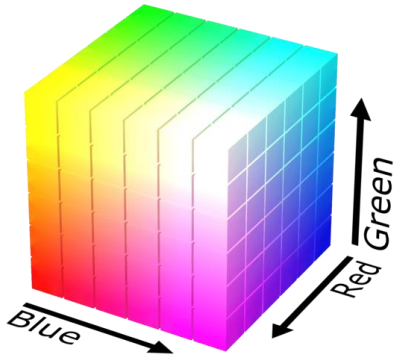

Fig. 49: RGB colour cube [74].

The RGB of the image is determined by red, green, and blue values. The value range of each primary colour is from 0 to 255. For example, RGB of white is (255, 255, 255) and black is (0, 0, 0). Also red could be represented as (255, 0, 0), green as (0, 255, 0) and blue as (0, 0, 255).

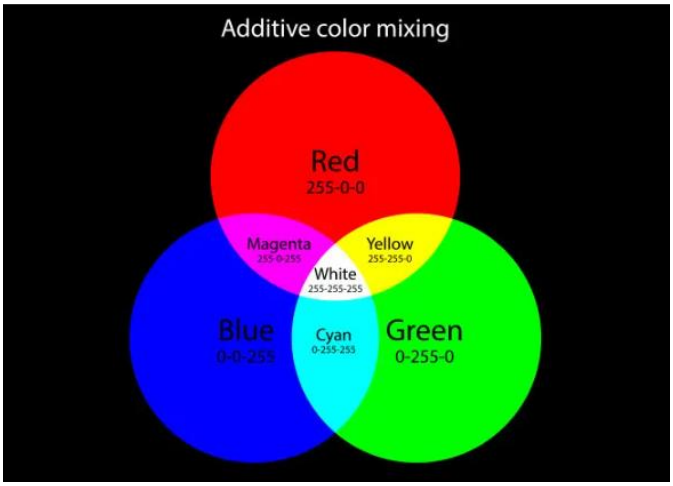

Fig. 50: Additive colour mixing [75].

2.6.3.4 Other image parameters

The brightness of an image depends on the exposure settings of the camera when the image is captured.

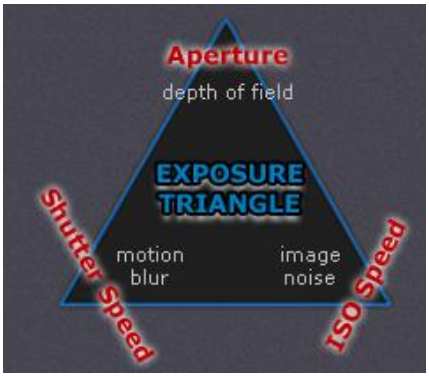

Fig. 51: The exposure triangle [76].

Exposure settings of an image include aperture, shutter speed and ISO speed. Aperture decides the area of the light that could enter the camera. Shutter speed is the speed of the shutter on and off, which determines the time of light entering the camera. The ISO speed controls the sensitivity of camera sensors.

2.6.3.5 High-speed camera

A high-speed camera is a camera that can capture images with high frame rates, and it can record events that happen within a microscopic timescale. Hence, phenomena with shortchanging time, such as material behaviours and mechanical events could be recorded and researched using high-speed cameras [77]. There are four categories of high-speed cameras based on the frame rates. The four categories are high speed (50-500 frames per second), very high speed (500-100,000 frames per second), ultra-high-speed (100,000-10 million frames per second), and super high speed (over 10 million frames per second) [78] [79].

The history of high-speed cameras can be traced back to 1878. The British photographer E. Muybridge captured a sequence of high-speed motion with 24 cameras attached to a shutter release system [80].

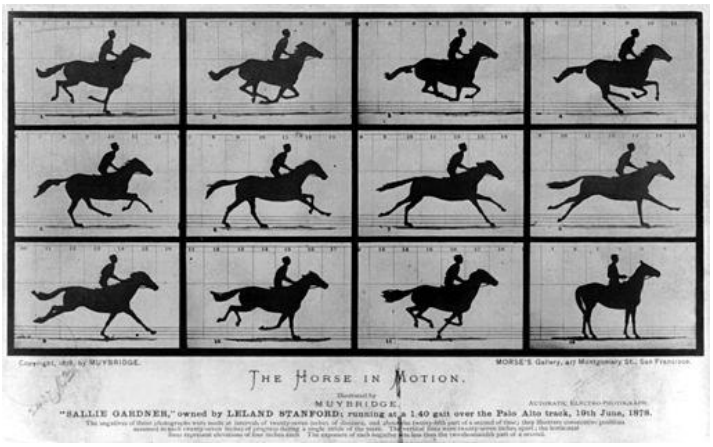

Fig. 52: High-speed image sequence ofr a house in motion captured by E. Muybridge [80].

In the 1930s, Bell Telephone Laboratories redesigned and produced a high-speed camera with 5000 frames per second (fps) and named it FASTAX. Then Wollensak Optical Company improved the camera by increasing the frame rate to 10,000 fps. A few years later, C. D. Miller developed a rotating mirror camera that theoretically could reach 1,000,000 fps [80].

Nowadays, high-speed cameras normally use either a CCD sensor or a CMOS sensor to record. A modern digital high-speed camera could capture images continuously with a set frame rate. A trigger is used to control the recording interval depending on the requirement. For example, the recording interval could be set as a specific time interval before or after the trigger signal [81]. The utilisation of triggers can also synchronize multiple cameras together to give various kinds of information in the same event.

2.7 Conclusion

In conclusion, this chapter gives the background information related to the research project, including the basic information about hydrogen, three types of gaseous flames, hydrogen combustion and visualization methods used in this project. In the following chapters, details of experiments and their results will be presented, and their results will be analysed and discussed.

Chapter 3: Hydrogen-air diffusion flame ignition visualisation

3.1 Introduction

Although hydrogen could be a superior replacement for petroleum and natural gas, using hydrogen as fuel still faces enormous safety issues. Hydrogen has a wide range of flammability and only needs low energy to be ignited [7]. Hence the possibility of accidental fire and explosion is higher than in other gaseous fuels. Therefore, the mechanism of hydrogen-air diffusion flame ignition should be studied in detail. Among all the research, it could be noticed that the colour of hydrogen diffusion flame is various in different cases. Flame colour could give plenty information of combustion process, which is worth researching.

In this chapter, the ignition process of a hydrogen diffusion flame will be researched. Ultra-high purity hydrogen gas was filled in a soak or distilled water bubble and ignited by an electrical spark. The ignition process was monitored and recorded using a schlieren imaging system and a high-speed camera. The High-speed camera provides the flame colour information, and the schlieren imaging system

shows the flow behaviour of confined hydrogen. The RGB channel values of the flame images will be worked out. The ratio of the red channel value to the other channel values will be calculated and compared. Therefore, the difference between the flame colours could be shown. Possible explanations for the difference will be given as well.

3.2 Methodology

To study the ignition behaviour of hydrogen, the main idea is to capture the process of hydrogen bubble ignition with the high-speed camera and the schlieren imaging technique. In the research, soap bubbles filled with pure hydrogen were generated on the top of a plastic funnelled stand. Besides the soap bubble, distilled water bubbles were also researched as a comparison. Electrical sparks were generated just above the bubble. Hence, the hydrogen bubble could be ignited by the spark. schlieren imaging system and high-speed camera were trigged simultaneously to capture the whole ignition process.

In addition to the ignition behaviour of the hydrogen-air diffusion flame, the colour of the flame will also be analysed. In order to identify the flame colour in the image, red, green and blue channel values of the flame will be found by using a Python algorithm. The script identifies the flame location in the images and extracts the RGB values of all pixels in the flame area. Then the average and median value of the RGB channels could be calculated. The average and median value of the RGB channels of the soapy and distilled water hydrogen bubble flames can be analysed and compared.

3.3 Experiment preparation and set-up

3.3.1 Preparation of Hydrogen Bubbles

Soapy bubble

In this experiment, soapy water was used to generate soapy bubbles. Soapy water was a mixture of soap liquid and water with a ratio of 2:1.

The following ingredients (Table. 5) were used in the preparation of the soap liquid:

Aqua	Surfactants	Benzisothiazolinone (C_7H_5NOS)
Methylisothiazolinone (C_4H_5NOS)	Phenoxyethanol $(C_8H_{10}O_2)$	Limonene $C_{10}H_{16}$
Sodium Laureth Sulfate $(CH_3(CH_2)_{10}CH_2(OCH_2CH_2)_nOSO_3Na)$	Cocamidopropyl Betaine $(C_{19}H_{38}N_2O_3)$	Sodium Chloride $(NaCl)$
Glycerin $(C_3H_8O_3)$	Polyquaternium-7 $((C_8H_{16}CIN)_n(C_3H_5NO)_m)$	Lactic Acid $(C_3H_6O_3)$
Sodium Benzoate $(C_7H_5NaO_2)$	Tetrasodium Glutamate Diacetate $(C_9H_9NNa_4O_8)$	Diethylamino Hydroxybenzoyl Hexyl Benzoate $(C_{24}H_{31}NO_4)$
Ethylhexyl Methoxycinnamate $(C_{18}H_{26}O_3)$	Hexyl Cinnamal $(C_{15}H_{20}O)$	Linalool $(C_{10}H_{18}O)$
Alpa-Isomethyl Ionone $(C_{14}H_{22}O)$	Citronellol $(C_{10}H_{22}O)$	CI 42051

Table. 5: Soap liquid ingredients.

According to the ingredients, the main elements contained in the soap liquid used for the experiment include: C, N, O, H, S and Na.

A plastic gas pipe was connected to the hydrogen gas cylinder to provide hydrogen flow. The flow rate used in this experiment to generate the bubble was 60 ml/min. Before generating bubbles, hydrogen was exhausted directly from the pipe for a few minutes. So, the hydrogen in the bubble could be ensured to be pure (99.9995% purity).

One end of the hydrogen pipe was dipped into the soapy water to blow bubbles. Then the pipe was moved to the plastic funneled stand; hence a hydrogen bubble would be generated on the top of the stand. The hydrogen bubbles used in this experiment were approximately 17 mm in diameter.

Distilled water bubble

The distilled water bubbles were generated by submerging the hydrogen gas pipe into a small tank filled with distilled water. The tank was rinsed with distilled water for several minutes before being filled to ensure its purity. The hydrogen flow rate was the same as generating the soapy bubble, which is 60 ml/min. The distilled water bubbles would stand on the water surface for a few minutes after being blown. The size of the bubble used in the experiment was 17 mm in diameter as well.

3.3.2 Experiment set-up

In the experiment, a z-type schlieren imaging setup was used, and direct images of the experiment process were captured simultaneously. Once the hydrogen bubble was generated, the electric spark generator would be switched on and generate electric sparks. A schematic diagram of the experimental setup is shown in Fig. 53 below.

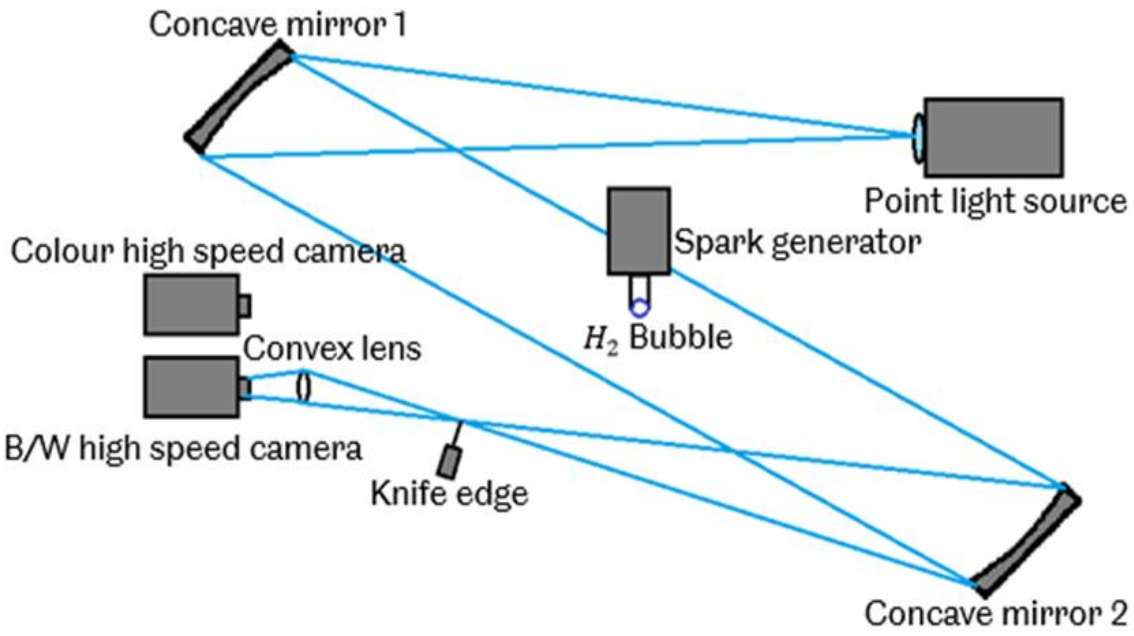

Fig. 53: Hydrogen bubble ignition experimental set-up.

High-speed camera

There were two different high-speed cameras engaged in this experiment. One is coloured, and the other one is monochrome. A Colour high-speed camera was used to capture the ignition process directly, while the monochrome camera was used to record the schlieren image of the same process. Two high-speed cameras were synchronized to make sure they recorded the same process.

The model of the colour high-speed camera used in this experiment is Photron FASTCAM SA4. It could reach a minimum exposure time of 16.7 ms and a highest frame rate of 500,000 fps. The frame rate used in the experiment to record the hydrogen bubble ignition process directly was 10,000 fps, and the shutter speed was 1/10,000 s. The main specification of the model is listed in Table. 6.

Model	FASTCAM SA4	
Image Sensor	CMOS	
Sensor Resolution	1024×1024 pixels	
Frame rate	Full frame	3600 fps max
	Frame rate Segment (500K)	500,000 fps max
	Frame rate Segment (500K)	216,000 fps max
Recording Colour Depth	Monochrome	12 bit
	Colour	RGB, each 12 bit (Bayer
Shutter Method	Electronic shutter	
Recording Method	IC memory	

Table. 6: Specification of colour high-speed camera FASTCAM SA4 [82].

Fig. 54: Photron FASTCAM SA4 high-speed camera [82].

The response of the Photron FASTCAM SA4 high-speed camera is shown in Fig. 55. The red, green and blue curves in the image represent the response of the red, green and blue channels of the camera, respectively. The intensity of the blue channel peaks at around 470 nm, the green channel at around 540 nm, and the red channel at about 620 nm.

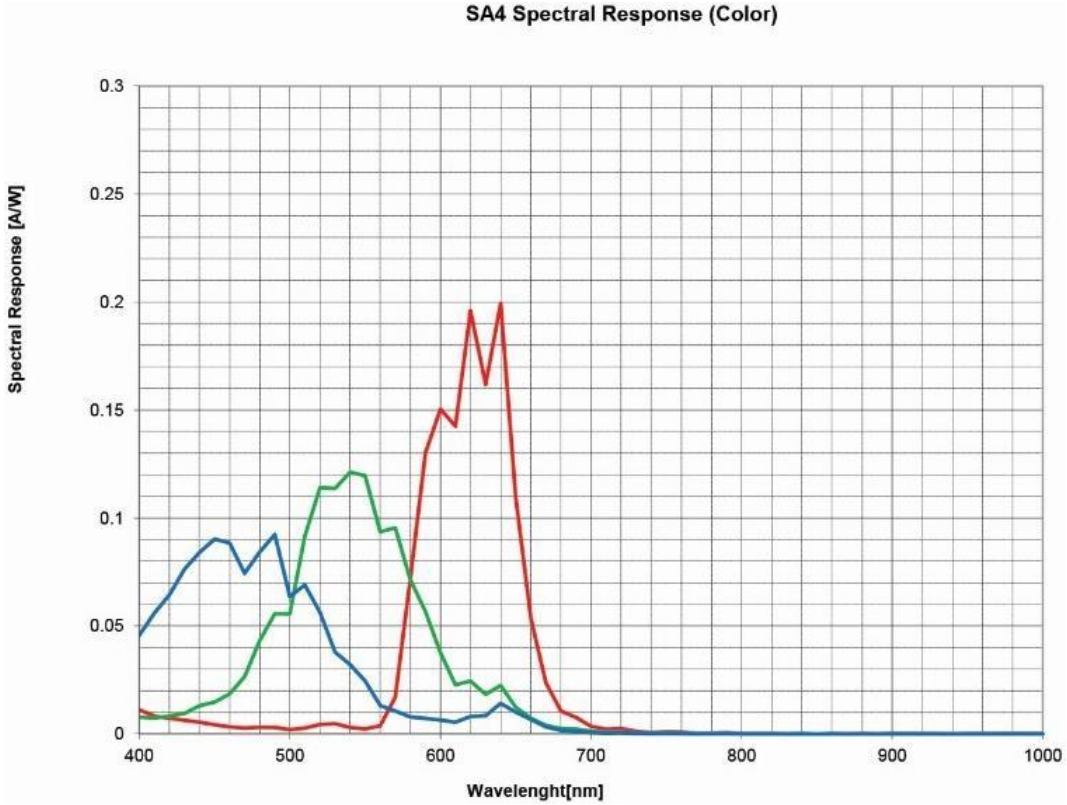

Fig. 55: The response of Photron FASTCAM SA4 high-speed camera [83].

The high-speed camera used in the schlieren imaging system was a Phantom V210 monochrome high-speed camera. The camera could reach a time resolution of 40 ns and a frame rate of over 2000 fps at 1280×800 pixels resolution. The highest frame rate is 300,000 fps at 128×8 pixels resolution [84]. In this experiment, the frame rate used was 10,000 fps.

Fig. 56: Phantom V210 high-speed camera [84].

Schlieren imaging system

A Z-type schlieren imaging system was used in this experiment. A Xenon light bulb was placed inside a black box, and the light came out from the small hole on one side of the box. However, it still was not an ideal point light source. Therefore, a convex lens was added in front of the small hole, making the light turn into a point source at the lens focus.

Two sets of concave mirrors were used in the experiment for different purposes. The first set was used for a relatively large image range to show the whole behaviour of hydrogen ignition. The concave mirrors used in this experiment have a 10 ft focal length (304.8 cm); thus, the distance from the light source to the concave mirror 1 was 10 ft. Moreover, the distance between two concave mirrors was 20 ft (equals 609.6 cm). The second set of mirrors was used to focus on the bubble and the spark area to show the details of ignition better. The focal length of the mirrors is 70 cm.

The point light source was first irradiated on the concave mirror 1 and then reflected through the experimental area and reached concave mirror 2. After that, the light reflected by the concave mirror 2 would emit on the high-speed camera CMOS sensor. A knife-edge made by a blade was added before the light reached the CMOS, and it blocked part of the light reflected by the concave mirror 2; hence contrast of the image could be enhanced. Besides, a convex lens was placed in front of the camera CMOS to focus the light.

3.4 Results and discussions

In this section, the schlieren image and direct image captured by the high-speed cameras will be shown. The ignition process of the hydrogen bubbles will be analysed and discussed. The colour of the visible flame will be identified with their RGB values in the images. The differences and similarities between the soapy and distilled water hydrogen bubble flame will be shown in the results. Furthermore, the possible reasons for the difference flame colour will be given.

3.4.1 Schlieren imaging results

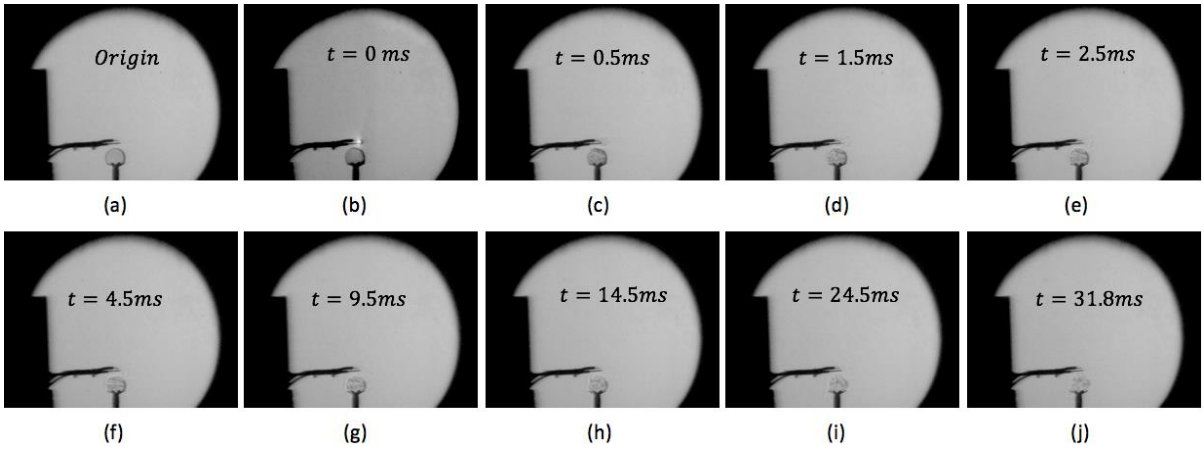

Fig. 57: Schlieren images of soapy hydrogen captured before ignition, captured by Phamton V210 monochrome high-speed camera at 10000 fps, t= time from the first spark.

In the experiments, two electric sparks were generated one after the other. The second spark was set to be generated at around 40 ms after the first one. The adoption of this time interval for the two electric sparks aimed to facilitate the detailed high-speed capture of the bubble. This time interval distinctly separated the

moments of two sparks. It allowed for observing the process by which the hydrogen gas diffuses into the surrounding air between ruptured and ignited. The diffusion processes of hydrogen gas from both the soapy bubbles and distilled water bubbles were similar.

Fig. 57 is the schlieren image of a soapy hydrogen bubble after the first and before the second spark. The images were captured at 10000 fps. It could be seen in Fig. 57 (b) that an intense flash appeared at the front end of the electric spark generator, which is the first spark. Then the bubble still held its shape within 0.5 ms after the spark. From 1.5 ms of the spark, the soapy bubble started to break from the top. After the bubble burst, the pure hydrogen was released from the soapy bubble and diffused evenly into the surrounding atmosphere.

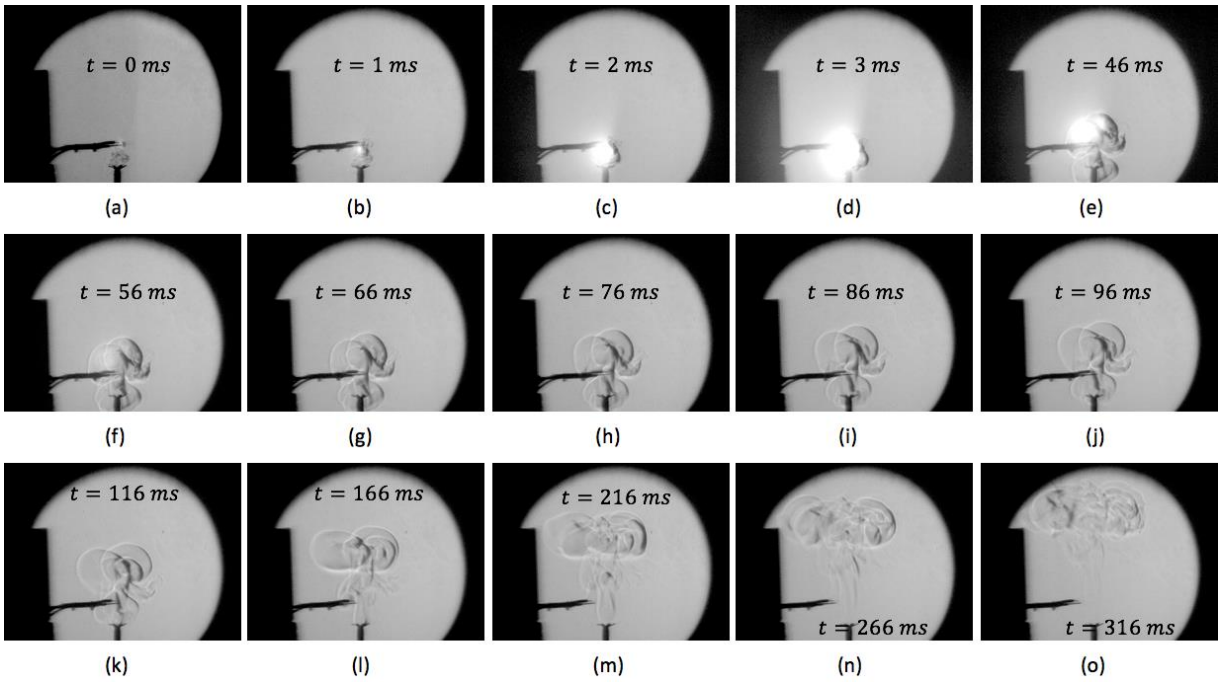

Fig. 58: Schlieren images of a soapy hydrogen bubble ignition process, captured by Phamton V210 monochrome high-speed camera at 10000 fps, $t =$ time from second spark.

It can be seen in Fig. 58 that when the second spark is generated, the hydrogen has not diffused to the surroundings in large quantities. The gas mass was ignited 1 ms after the spark, as shown in Fig. 58 (b). After being ignited, the gas flow propagated in all directions and travelled in the shape of circles. Approximately 56 ms after the ignition, the flow started to move upwards.

Visible flame only existed within the first 60 ms after the second spark. The bright flashes in Fig. 58 (b-f) are visible light from the flame. After 60 ms, there was no visible flame recorded. However, the high-temperature gas mass still existed and kept propagating. Then at about 116 ms after the ignition, the flow front began to propagate along the horizontal plane.

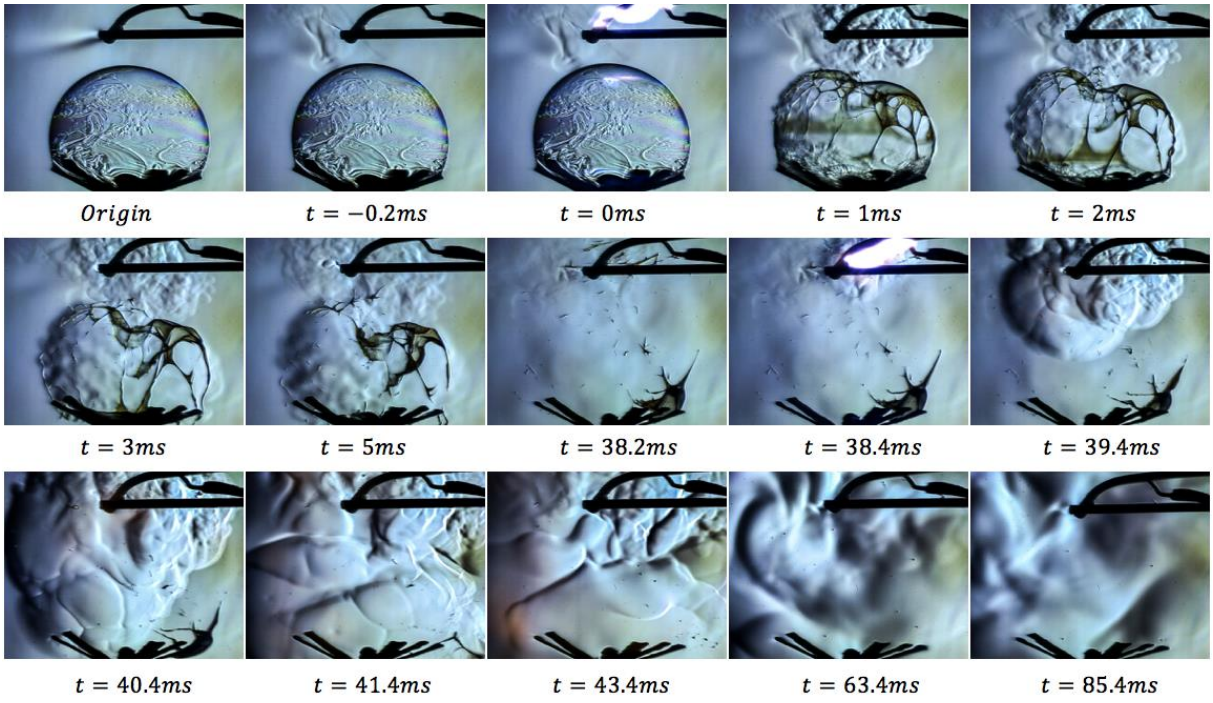

Fig. 59: Schlieren images of a soapy hydrogen bubble ignition process, captured by Photron FASTCAM SA4 colour high-speed camera at 5000 fps, t= time from the first spark.

The set of mirrors captured a relatively large testing area so that it could show a more comprehensive process of the ignition and subsequent combustion. However, due to the large shooting area, the details of the ignition moment could barely be seen in these images. Hence a set of smaller concave mirrors was used to focus on capturing the area around the bubble. Fig. 59 is the schlieren images of a hydrogen bubble ignition process captured by Photron FASTCAM SA4 colour high-speed camera at 5000 fps.

As shown in Fig. 59, before the second spark, the air around the electric spark generator tip was disturbed slightly. The disturbance was caused by the movement of the tip. When the first spark was generated, an intense fluctuated air mass appeared at the generator tip. The disturbed air mass was heated to a high temperature by the electric spark. The heated air then propagated around and burst the bubble. After the bubble was broken, the hydrogen in the bubble diffused around. At 38.4 ms after the first spark, a second spark was generated, and the hydrogen-air mixture was ignited at the position of the spark. It could be noticed that after the mixture was ignited, its propagation rate was much higher than before.

In this experiment, two different sets of mirrors were used. Fig. 58 shows the schlieren images captured using larger mirrors (focal length 304.8 cm), while Fig. 59 was captured by smaller mirrors (focal length 70 cm), resulting in different testing area sizes. The schlieren images obtained with the smaller mirror focus on capturing the process of bubbles being ruptured by the first electric spark and ignited by the second electric spark. On the other hand, the schlieren images obtained with the larger mirror capture the propagation of the ignited gas after the bubble is ignited. As

a result, the schlieren images obtained with the smaller mirror did not capture the entire flame, as thus the flame emission captured in Fig. 59 is much less compared to Fig. 58.

3.4.2 High-speed imaging

In this section, the images of soapy and distilled water hydrogen bubbles will be shown and discussed. The flame behaviour and colour at the ignition will be analysed. Furthermore, the difference between a soapy bubble and distilled water bubbles will be compared.

Fig. 60 is the high-speed imaging of a soapy bubble ignition process. The images were captured by Photron FASTCAM SA 4 at 10000 fps. As can be seen from the image, the visible flame appeared at the location of the spark. Then the flame propagated from the outer layer into the inner part of the hydrogen-air mixture. The brighter the colour of the flame, the more intense the combustion reaction was. 26 ms after the second spark, the visible flame began to move upwards and started to dim until it disappeared at 56 ms. Compared with the images captured by schlieren, it can be seen that the shape of the visible flame is consistent with the shape of the gas flow.

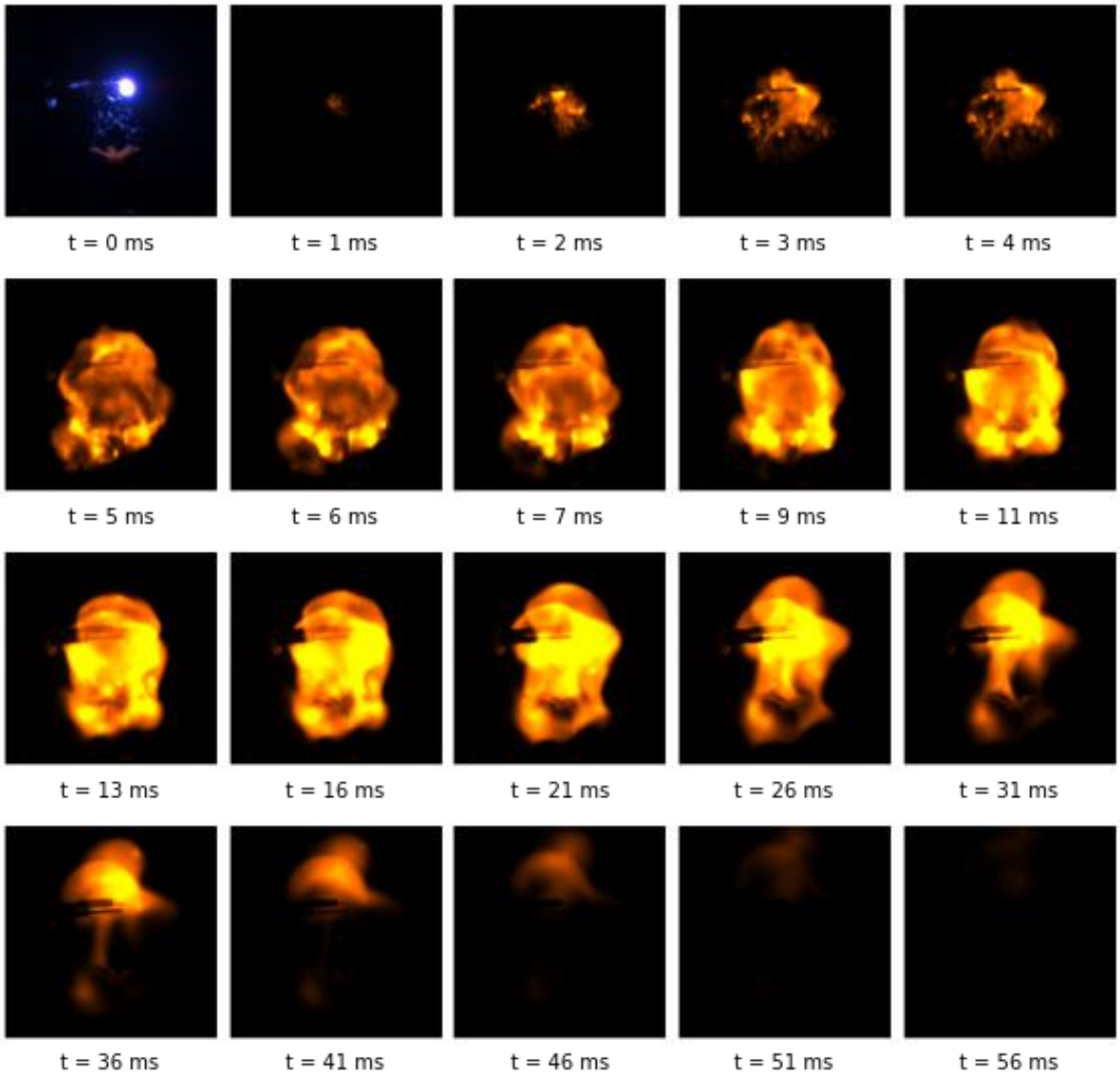

Fig. 60: High-speed camera images of soapy hydrogen bubble ignition, captured by Photron FASTCAM SA 4 at 10000 fps, t = time from the second spark.

Besides the soapy hydrogen bubble, distilled water hydrogen bubble ignition process was also recorded by the same high-speed camera at the same frame rate. Similar to the soapy hydrogen bubble flame, the distilled water hydrogen bubble flame was also started from the location of the spark, and then the visible flame propagated around and disappeared at 11 ms after the ignition.

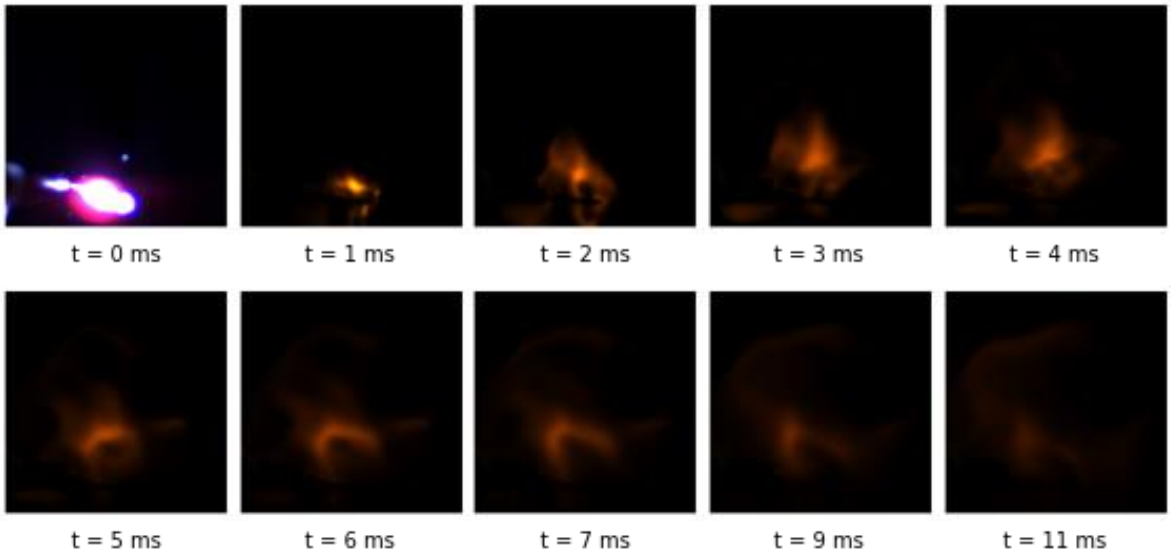

Fig. 61: High-speed camera images of distilled water hydrogen bubble ignition, captured by Photron FASTCAM SA 4 at 10000 fps, t = time from second spark.

It could be seen in Fig. 61 that the colour of the flame was different from the colour of the soapy hydrogen bubble flame. The colour of the soapy hydrogen bubble flame was red at first, then gradually became bright yellow as the combustion reaction intensified and finally turned red again until it disappeared. However, the distilled water hydrogen bubble has a red flame all the time. The flame colour of the distilled water hydrogen bubble was redder, while the flame colour of the soapy bubble was more yellow. As the soapy bubble was made from the soapy solution, which contains a large amount of sodium, the yellow colour of the flame might be the emission of sodium. At the same time, the distilled water hydrogen bubble was only made of distilled water; hence the colour of the distilled water bubble should be the actual colour of the hydrogen-air diffusion flame colour.

The colour of the image can be determined by the values of the RGB channels, so the change in the ratio of the three channel values can be used to verify the trend of

the flame colour. Therefore, in order to study the change of the flame colour more intuitively, the RGB values of the flame images, especially the red channel values, were analysed and compared.

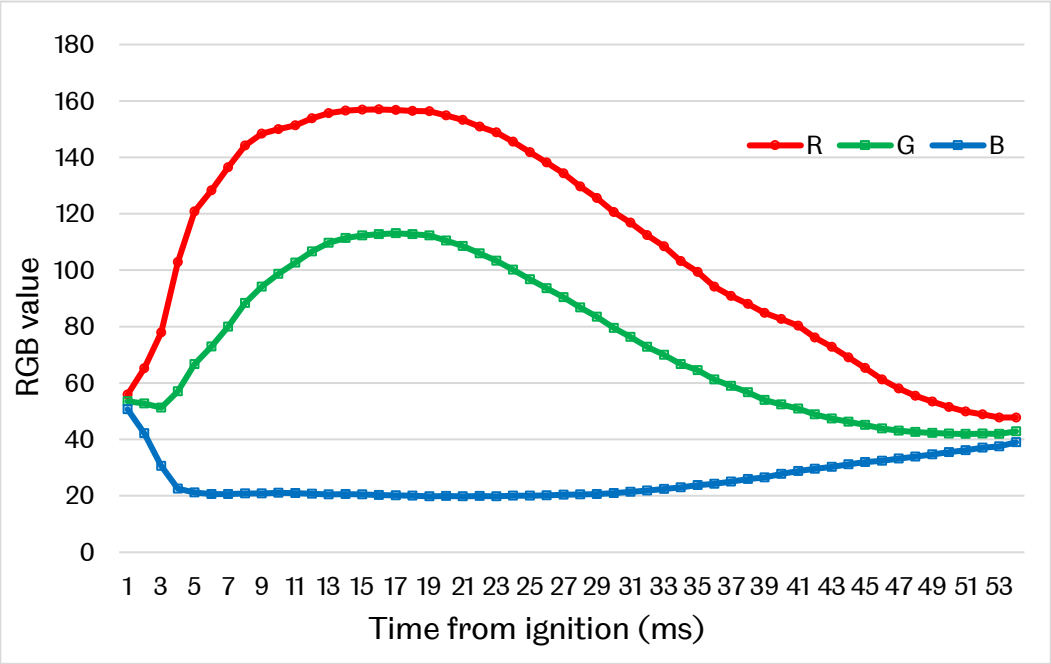

Fig. 62: Average RGB value of the soapy hydrogen bubble flame.

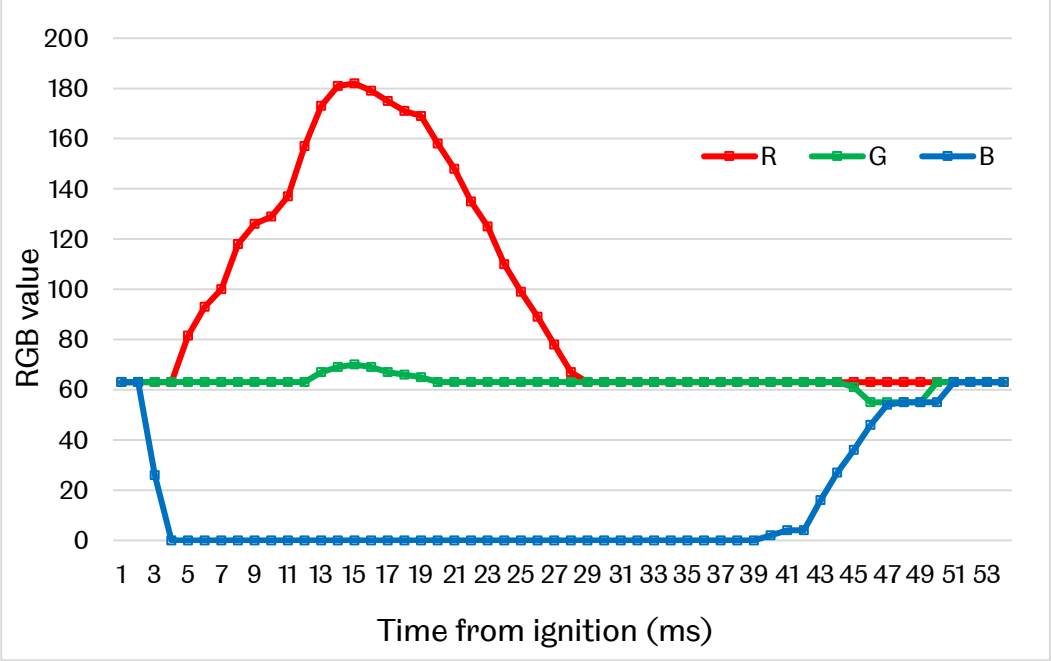

Fig. 63: Median RGB value of the soapy hydrogen bubble flame.

The average and median RGB values of the soapy hydrogen bubble were presented in Fig. 62 and Fig. 63. The time range is 0 to 53 ms from the ignition, during which the flame is visible. The average red channel values are higher than the green and blue channel values over this time frame, and the median value of the red channel is also higher than the other two channels between the 5-29 ms range. At 16 ms after being ignited, both the average and median values of the red channel are at their highest, which are 157 and 179, respectively. Then the value of the red channel begins to decrease gradually until the values of the RGB three channels are the same. It can be found in Fig. 60 that the soapy hydrogen bubble burnt most intensely at 16 ms, which matches the RGB channel trend.

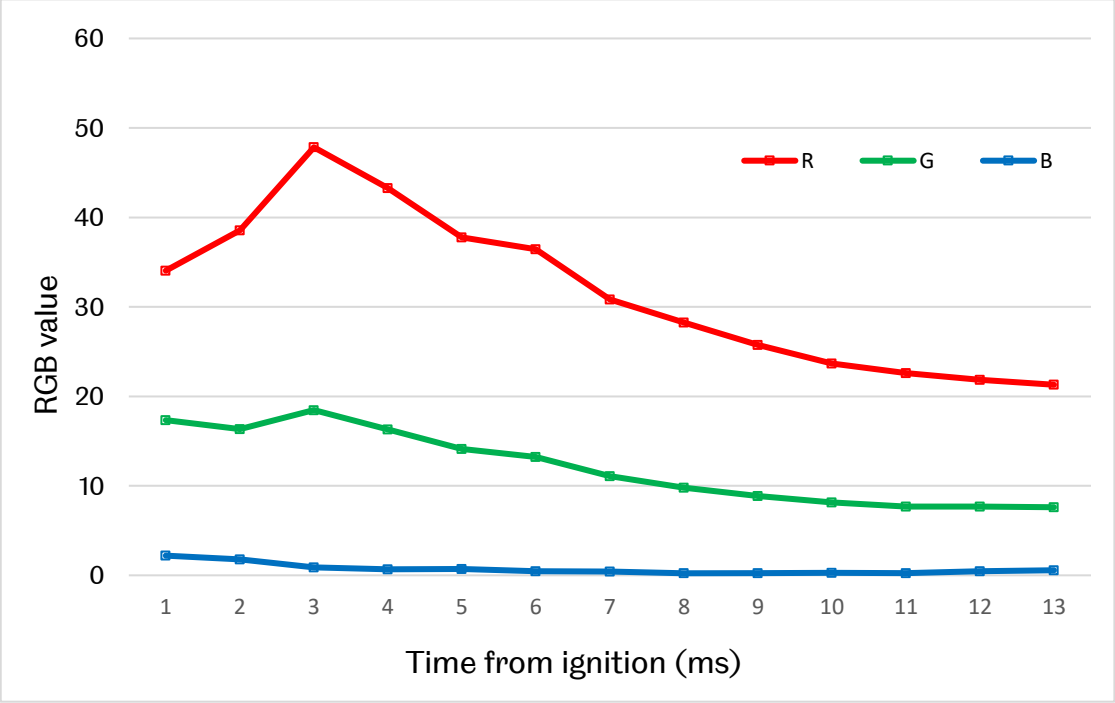

Fig. 64: Average RGB values of the distilled water hydrogen bubble flame.

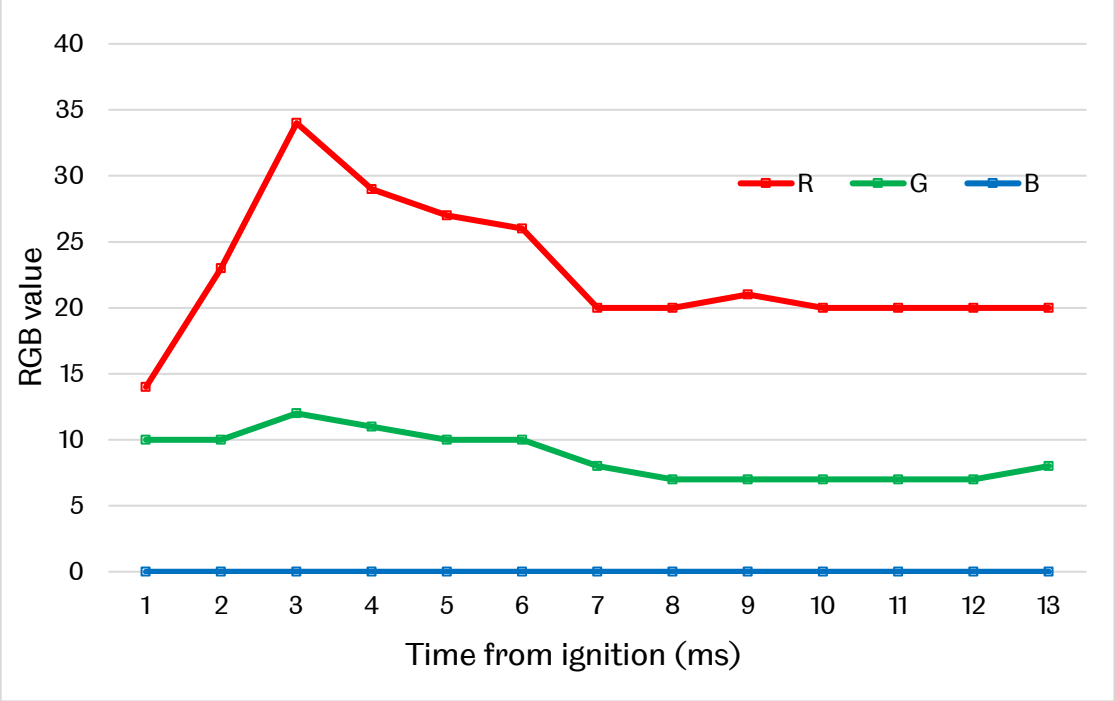

Fig. 65: Median RGB values of the distilled water hydrogen bubble flame.

The average and median RGB values of the distilled water hydrogen bubble flame images were also shown in Fig. 64 and Fig. 65. Similar to the soapy hydrogen bubble flame, the values of the average and median R channel of the flame images are higher than the G and B channels during the whole combustion process. Both the highest average and median red channel values appear at 3 ms after the ignition, which matches the direct image of the flame. The highest average and median values of the red channel are 48 and 37, respectively.

Although the average and median red channel values of the soapy bubble hydrogen flame are higher than the values of the distilled water hydrogen bubble flame, the colour of the flame is determined by the ratio of RGB channel values. Therefore, in order to compare the colour of the flame, the ratio of the RGB channels should be calculated. Since it could be found from the high-speed camera images

that the bubble flames show red and yellow colours, the ratio of the red channel is mainly analysed.

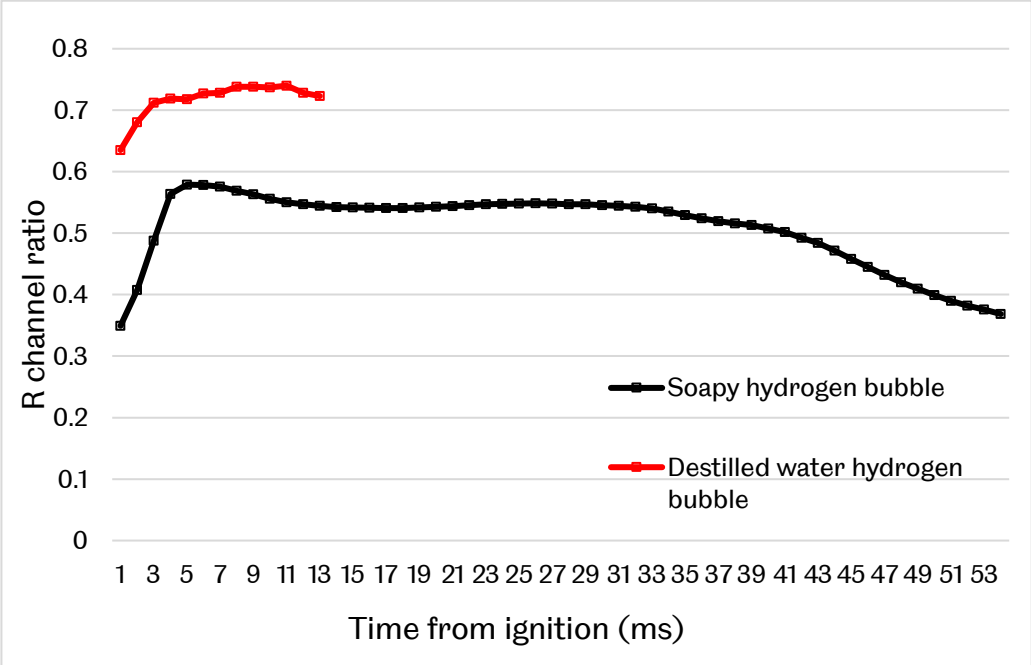

Fig. 66: Average R channel ratio of the hydrogen bubble flames.

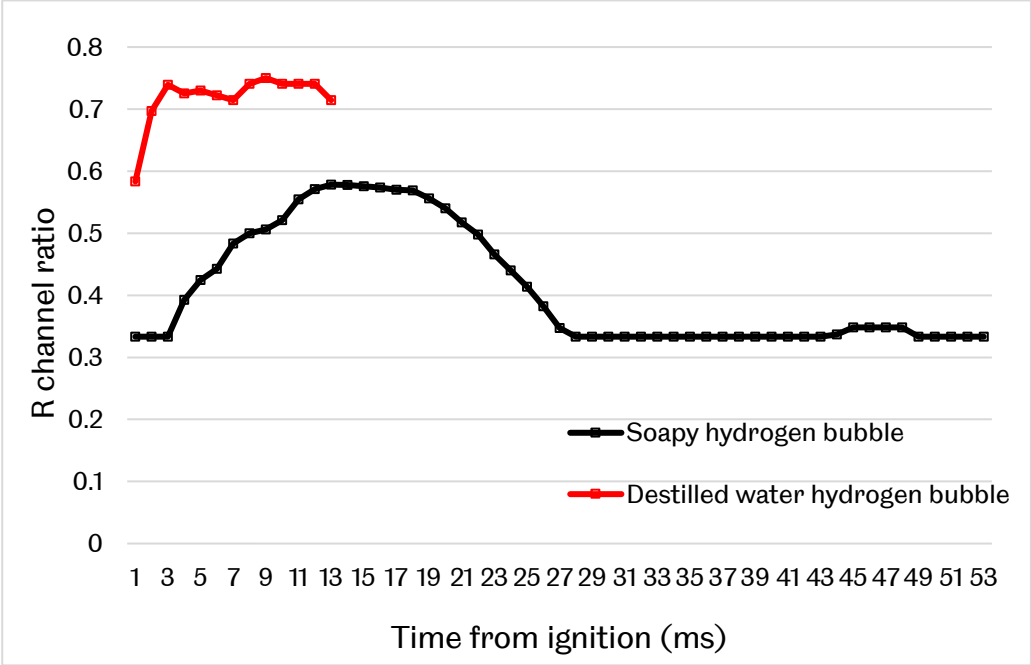

Fig. 67: Median R channel ratio of the hydrogen bubble flames.

Fig. 66 and Fig. 67 show the ratio of the average and mean value of the red channel. It could be seen that the red channel ratio of the distilled hydrogen bubble is higher than the soapy hydrogen bubble, and this means that the former flame is more reddish than the latter. The highest ratios of the average and median red channel values reach 0.738 and 0.730 for the distilled water hydrogen bubble flame, while the ratios are only 0.569 and 0.578 for the soapy hydrogen bubble flame. Besides, the lowest red channel ratio of the distilled water hydrogen flame is higher than the highest red channel ratio of the soapy hydrogen bubble flame. Therefore, it can be determined that the flame colour of distilled water hydrogen bubble flame is redder than that of the soapy hydrogen bubble throughout the whole combustion process.

As mentioned in section 3.3.1, the soapy bubble was made of soapy water; hence a certain amount of sodium may be involved in the combustion process. Sodium has two strong emission lines at 589.0 nm and 589.6 nm, which emit yellow light. In contrast, no other substances participated in the reaction in the distilled water hydrogen bubble combustion except water, hydrogen, and air. Therefore, the flame colour of the distilled water hydrogen bubble should be more close to the hydrogen-air diffusion flame colour. Meanwhile, the presence of sodium causes the flame colour of hydrogen to be more yellowish.

3.5 Conclusion

This chapter mainly introduces the research on the ignition behaviour and flame colour of pure hydrogen bubbles. Two different types of bubbles were used in the experiment in which, one was made of soapy water, and the other one was made of

distilled water. Both types of the bubble were filled with high purity hydrogen. The behaviour of the bubble was recorded by using the schlieren imaging technique and high-speed imaging technique.

From the schlieren images, it could be seen that the hydrogen bubble was broken when the first spark was generated, but it was not ignited. The hydrogen was released from the burst bubble and diffused with the surrounding air. When the second spark was generated, the mixture of hydrogen and air was ignited, and a visible flame could be seen. The visible flame only existed for 56 ms, and after it disappeared, the high-temperature gas continued to propagate. At 116 ms from the second spark, the gas started to propagate along the horizontal plane.

The visible flame was captured by the high-speed colour camera, and the frame rate was set to be the same as the schlieren imaging camera. The average and median RGB values of the two flames were analysed, and the ratios of the red channel value were also compared. The red channel values of both soapy and distilled water hydrogen bubble flame were higher than the other two channels. The ratio of the red channel value of the distilled water hydrogen bubble was higher than the ratio of the soapy hydrogen bubble flame. Therefore, it could be concluded that the soapy and distilled water hydrogen bubble produced different flame colours. The distilled water hydrogen bubble flame was more reddish, while the soapy hydrogen bubble flame was more yellowish compared to each other. The existence of sodium in the soapy hydrogen bubble might be the leading cause of the yellow flame.

However, the RGB channel analysis of the flame images can only be used to compare the flame colour, and details of the hydrogen-air diffusion flame colour

could not be obtained. Therefore, the spectrum of a hydrogen-air diffusion flame was captured by a spectrograph, and further analysis of the flame colour will be discussed in the following chapters (Chapter 5 and Chapter 6).

Chapter 4: Hydrogen-air diffusion flame direct imaging

4.1 Introduction

It was shown in the previous chapter that the hydrogen-air diffusion flame during the ignition process is reddish. By comparison of the soapy and distilled water hydrogen flame bubbles, the influence of sodium on the reddish flame colour of the hydrogen diffusion flame is excluded. However, it is not clear whether the flame colour of hydrogen is the same during the stable combustion process.

In order to further analyse the flame colour of hydrogen, images of hydrogen-air diffusion flames under different co-flow conditions will be captured by a DSLR camera and analysed. Besides, a narrow band $H-\alpha$ filter will be used to determine the presence of $H-\alpha$ in the hydrogen diffusion flame.

In this chapter, the experiment method and setup will be introduced. Different types and flow rate co-flows will be added to the hydrogen-air diffusion flame. The images of these hydrogen flames will be captured, and their RGB values will be measured using the Python algorithm.

4.2 Methodology and setup

The method used in this experiment is direct imaging. A Canon EOS 1200D DSLR camera captures the images of hydrogen diffusion flame. Same as the method used in the previous chapter, RGB values in the images will be extracted by the Python algorithm. The Red value ratio of the RGB channels will be compared. Differences between the hydrogen-air diffusion flames with different co-flow conditions will be discussed. Fig. 68 is the schematic diagram of the experimental setup.

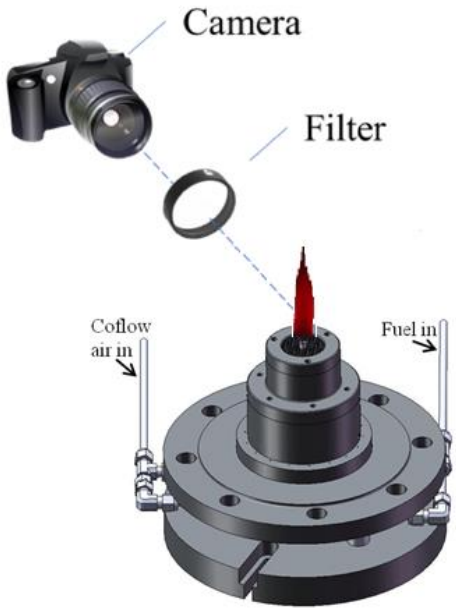

Fig. 68: The schematic diagram of the experimental setup.

There were two types of co-flow gas used in this experiment: air and oxygen. The oxygen used in the experiment was from BOC Industrial Gases UK and was research-grade N5.5, which is 99.9995% purity. The air used in the experiment was compressed air from outside the laboratory building. The hydrogen used in this experiment was research-grade N5.5 from BOC Industry Gases UK as well. The

pressure in the gas bottles was 200 Bar. The Gauge pressure of all gases is 1 bar.

The flow control system was designed and made at the University of Sheffield. Flow meters were Caché Uniflux Variable Area Flowmeters. The measuring range of hydrogen and air is 0-10 l/min and 0-13 l/min, respectively. While no oxygen flow meter is available, the measurement of oxygen flow rate is carried out utilising air flow meters. The actual oxygen flow rate could be converted by the following equation:

$$\boldsymbol{q_{oxygen} = q_{air}\sqrt{\frac{\rho_{air}}{\rho_{oxygen}}}} \qquad \textbf{Equation. 27}$$

Where, $\boldsymbol{q_{oxygen}}$ is the actual flow rate of Oxygen, $\boldsymbol{q_{air}}$ is the reading of the air flow meter, $\boldsymbol{\rho_{air}}$ and $\boldsymbol{\rho_{oxygen}}$ are the density of oxygen and air, respectively.

According to [85] [86], the density of air and oxygen at 20℃, 1 ATM condition is $1.205\ kg/m^3$ and $1.314\ kg/m^3$. Oxygen and hydrogen flow rates used in the hydrogen diffusion flame with oxygen co-flow experiment are listed below (Table. 7).

Hydrogen diffusion flame with oxygen co-flow

Hydrogen flow rate (l/min)	Oxygen flow rate (l/min)	Air flow meter reading (l/min)
3.00	0.30	0.32
3.00	0.55	0.58

Table. 7: Flow rates used in the hydrogen diffusion flame with oxygen co-flow.

Air and hydrogen flow rates used in the hydrogen diffusion flame with air co-flow

experiment are listed as follows (Table. 8):

Hydrogen diffusion flame with air co-flow	
Hydrogen flow rate (l/min)	Air flow rate (l/min)
3.00	6.50
3.00	13.00

Table. 8: Flow rates used in the hydrogen diffusion flame with air co-flow flow rate.

Same as the previous experiment, all the gases used were released from the gas pipelines for a while prior to the experiments. Thus, the gases trapped in the pipelines would be evacuated and replaced by the experiment gases. This operation could reduce the influence of irrelevant gases on the experiment.

The burner used in this experiment was a tailor-made Swagelok burner. This burner was used for both the hydrogen diffusion flame and co-flowed flames. It contains a fuel outlet nozzle, which is surrounded by a co-flow outlet. The size of the fuel nozzle is 6 mm in diameter.

The image below (Fig. 69) is the schematic diagram of the burner. It contains two gas inlets, one for the fuel and the other for the co-flow gas. Fuel gas enters the nozzle while co-flow enters the honeycomb. Hence in this experiment, hydrogen gas flow through the fuel nozzle, which is in the middle of the burner. Air and oxygen flow through the honeycomb when co-flow is required. The honeycomb design helps stabilise the flame and reduces the risk of flashbacks.

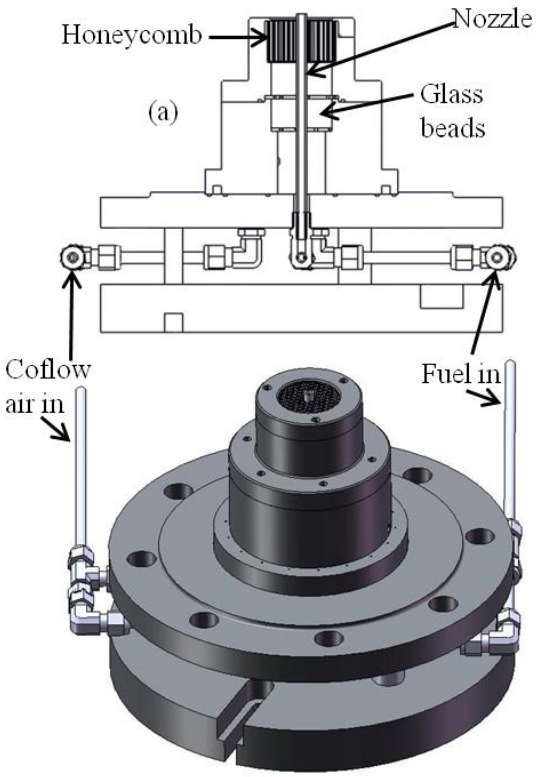

Fig. 69: The schematic diagram of the Swagelok burner used in this experiment [87].

The camera used in this experiment was a Canon EOS 1200D DSLR camera. The lens used was a Canon zoom lens EF-5 with an 18-55 mm focus length. The resolution of the images captured was 6000 × 4000 pixels. The exposure time was 1/40 second (40 fps), and the ISO speed was 800. All the flame images were taken under the same camera settings, except the images with the narrowband filter.

Fig. 70：Cannon EOS 1200D camera with EF-5 18-55 mm lens [88].

Besides, a narrowband $H-\alpha$ filter is also applied in the experiment to verify the existence of $H-\alpha$. The filter used was a $50 \times 50 \times 3$ mm Baader H-alpha 7 nm CCD narrowband filter, model Baader Planetarium 2458383R.

Fig. 71: Badder H-alpha 7 nm CCD narrowband filter [89].

The filter has a half-width of 7 nm, which means the band of the filter is $656.28 \pm 3.5\ nm$. It was mounted on the lens when images were captured.

4.3 Direct images of hydrogen-air diffusion flame under different co-flow conditions

In this sub-section, the images of hydrogen-air diffusion flame under different co-flow conditions will be presented, and their RGB values will be analysed and compared.

The images of hydrogen flames captured by the DSLR camera are shown in Fig. 72 The images were taken with 1/40 s exposure time.

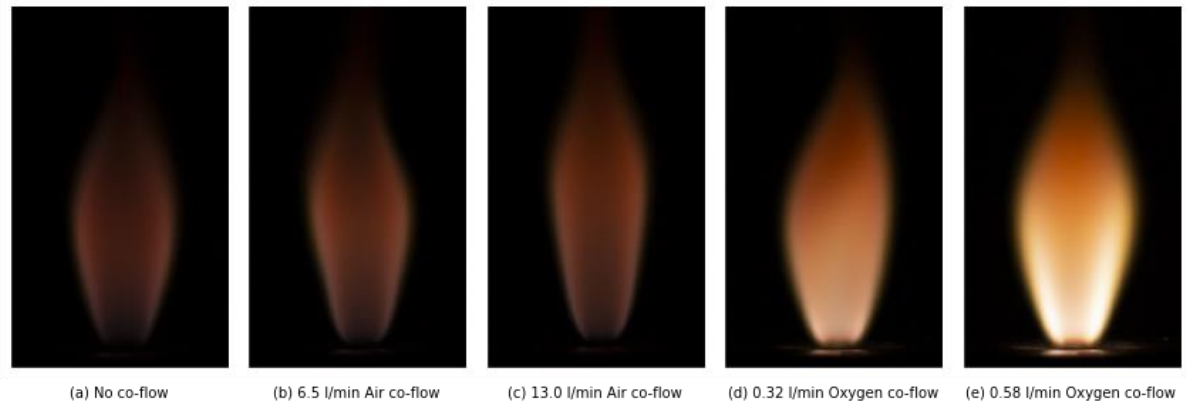

Fig. 72: Direct images of hydrogen-air diffusion under different co-flow conditions: (a) no co-flow; (b) 6.5 l/min air co-flow; (c) 13 l/min air co-flow; (d) 0.30 l/min oxygen co-flow; (e) 0.55 l/min oxygen co-flow.

It could be noticed from Fig. 72 that the length of the flames is positively correlated with the flow rate of the co-flow. The colour of the hydrogen diffusion flame without co-flow (Fig. 72 (a)) is faint reddish, and the outer layer of the flame is more obvious than the inner layer. The colours of the flame with air co-flows (Fig. 72 (b)(c)) are similar to the flame without co-flow, which is also faint reddish. The difference is that the flame with the air co-flow is slightly brighter. At the same time, the higher the co-flow rate, the longer and thinner the flame. The flame shapes with oxygen co-flows are basically the same as the flame without co-flow; however, their colours are very different. Flames with oxygen co-flows are noticeably brighter and more vibrant in colour.

In order to study the colours of hydrogen-air diffusion flame under different co-flow conditions, the average and mean RGB values of their image were figured out as a method to determine the colour of the flames. The RGB values are listed below.

Co-flow condition	Average			Median		
	R	G	B	R	G	B
No co-flow	46.89	23.66	17.76	47	24	17
6.5 l/min air	57.91	29.98	19.86	59	30	18
13 l/min air	59.57	29.78	18.14	63	31	16
0.30 l/min oxygen	112.43	68.25	39.73	114	57	24
0.55 l/min oxygen	138.29	99.17	60.48	148	80	30

Table. 9: RGB channel values of the hydrogen diffusion flames under different co-flow conditions.

From Table. 9, it can be found that the trend of average and median RGB values are the same. The highest average and median RGB values appear in the image of 0.55 l/min oxygen co-flow flame. The higher the RGB values, the brighter the flame in the image, which matches the previous conclusion from Fig. 72. Also, as the flow rate of the co-flow increases, the values of RGB will increase. However, the specific values of RGB channels can only determine the brightness of the flame. The flame colour is associated with the RGB value ratios. Hence, the proportions of the red channel are compared due to the red bias of the hydrogen flame colour.

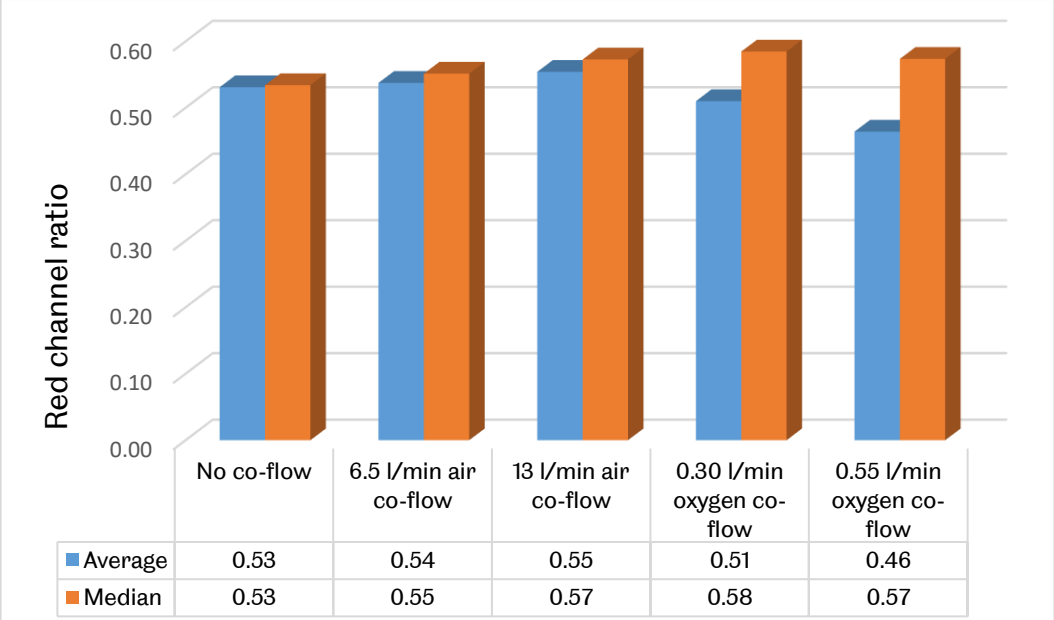

Fig. 73: Red channel ratio of hydrogen diffusion flames under different co-flow conditions.

A higher red channel ratio means that the colour of the flame is more reddish. It can be obtained from Fig. 73 that the highest average red channel ratio is the flame with 13 l/min air co-flow, and the highest median red channel ratio appears in the flame with 0.30 l/min oxygen co-flow. Comparing with the average values, the median values may be more representative of the overall colour of the flame. Hence the flame with 13 l/min air co-flow, 0.30 l/min oxygen co-flow and 0.55 l/min oxygen co-flow would have basically the same level of red. In contrast, the hydrogen flame without co-flow has the lowest red channel ratio, which means the redness of the image is the least. However, the species or elements that cause the reddish colour of the hydrogen diffusion flames are still unknown.

4.4 Narrowband filtered hydrogen-air diffusion flame

$H-\alpha$ has an emission line at 656.26 nm, which locates in the wavelength range of the red colour band. Hence, the existence of $H-\alpha$ in the hydrogen diffusion flame is highly possible. To verify the hypothesis, a narrowband $H-\alpha$ filter was used to allow the wavelength of 652.78 nm to 659.78 nm to pass only to visualize the hydrogen flame. The flame images were compared with the unfiltered images. The images of diffusion hydrogen flame captured from experiments are presented in Fig. 74.

Fig. 74: Hydrogen-air diffusion flame from a Bunsen burner. Left: unfiltered; Right: filtered.

In detail, Fig. 74 (Left) shows unfiltered hydrogen flame with 1/15 second exposure time, and Fig. 74 (Right) shows the hydrogen flame with 4 seconds exposure time after applying the narrowband $H-\alpha$ filter. It can be seen that the reddish flame is clearly shown in the filtered image. Hence the hydrogen diffusion flame must have emission lines in the wavelength range of 652.78 nm to 659.78 nm. The sodium double lines are out of the range of the $H-\alpha$ filter used in this experiment.

Therefore, the reddish colour of hydrogen-air diffusion flame could be caused by the emission of $H-\alpha$.

4.5 Conclusion

This chapter shows the images of the hydrogen-air diffusion flames under different co-flow conditions. The flame colours were compared by analysing their RGB values. In general, stable hydrogen flames have reddish flame colour, similar to the hydrogen ignition flame described in the previous chapter.

In this experiment, 5 cases of the co-flow condition were tested and analysed. They are hydrogen flames with no co-flow; 6.5 l/min air co-flow; 13 l/min air co-flow; 0.30 l/min oxygen co-flow; and 0.55 l/min oxygen co-flow. Among these flames, the flames with co-flows are brighter than the flame without co-flow. The brightness of the flame increases with the flow rate of the same type of co-flow. The flames with oxygen co-flows are brighter than the air co-flowed flames. By analysing the RGB channel values of the flame images, it can be found that the ratios of red channel values of these hydrogen diffusion flames are all higher than 0.5. Therefore, the hydrogen diffusion flames appear to be reddish from the RGB analysis.

The presence of the $H-\alpha$ emission line is a possible cause of the reddish flame colour of hydrogen. As a possible reason for such reddish colour appearing in the hydrogen flame, the narrowband $H-\alpha$ filter was used in this experiment to validate the existence of $H-\alpha$. An image of the hydrogen diffusion flame was captured with the filter mounted on the camera lens. The image indicated that there are emission lines exist in the range of 652.78 nm and 659.78 nm. Thus, the possibility of the

presence of $H-\alpha$ in hydrogen-air diffusion flame is high.

In order to further verify the existence of $H-\alpha$ in the hydrogen diffusion flame and identify the sources of the reddish flame colour, spectra of the hydrogen diffusion flames will be presented in the following two chapters. In this research, the most interesting wavelength range is 590 nm to 700 nm, which is the red light band, and 650 nm to 660 nm, where the $H-\alpha$ emission line presents. The species or elements that have possible contributions to the hydrogen spectra will be discussed.

Chapter 5: Hydrogen-air diffusion flame spectrum analysis

5.1 Introduction

However, the species or elements that cause the reddish flame colour are still not identified. The research on the flame colour of hydrogen diffusion flame is significant, and it helps study the fundamental properties of hydrogen and provides a theoretical basis for future applications.

This chapter mainly describes the experiment and results of the hydrogen-air diffusion flame spectrum. The methodology and setup of the experiment will also be explained. The equipment used in the experiment, including spectrograph, burner, DSLR camera, hydrogen, etc., will be introduced. Moreover, possible problems in the experiment and their solutions will be discussed.

In addition, a Chemkin model of the hydrogen-air diffusion flame has also been developed, which simulates the concentration of H, O, and OH radicals within the flame as well as the flame temperature. These resules will be presented in this Chapter.

Furthermore, the spectrum of hydrogen-air diffusion flame will be shown in this chapter. The emission peaks with high intensity will be analysed, and species and elements that may cause these emission peaks will also be discussed. Hence factors affecting flame colour could also be found.

5.2 Chemkin Model

In this Chemkin model, the mole fraction of H, O, and OH and the temperature of the hydrogen diffusion flame were simulated. The hydrogen gas flow rate used in this model was the same as that used in the experiment, which is $6\ l/min$. The inner diameter of the fuel nozzle was 6 mm. According to Cheng [90], the hydrogen diffusion flame reaction zone width was about 4 mm, therefore, in this model, the adopted reaction zone width was 4 mm. The following figures are the mole fraction of species in this simulation.

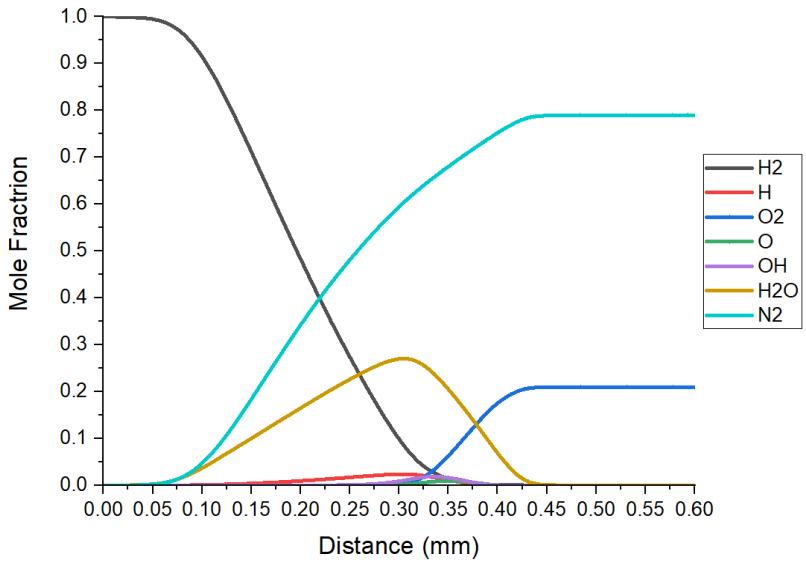

Fig. 75: Mole fraction of species in the hydrogen-air diffusion flame simulated by Chemkin.

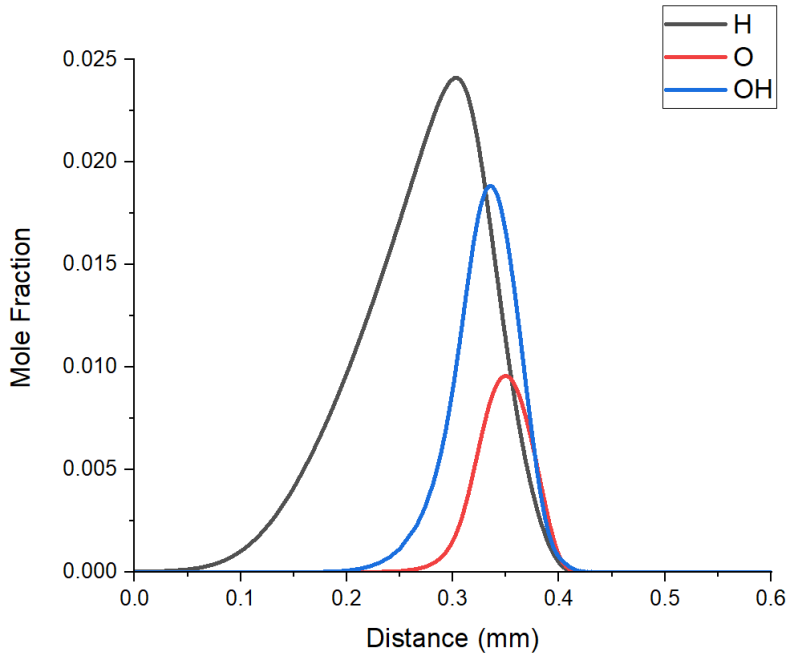

Fig. 76: Mole Fraction of H, O, and OH radicals in the hydrogen-air diffusion flame simulated by Chemkin.

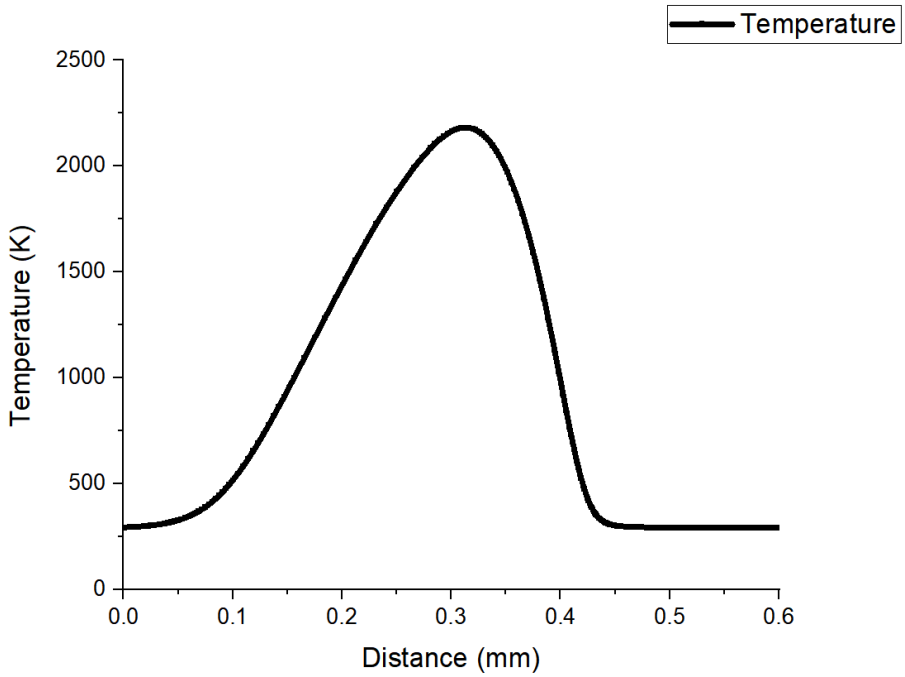

Fig. 77: Temperature profile of the hydrogen-air diffusion flame simulated by Chemkin.

Fig. 75 indicates that in the hydrogen-air diffusion flame, the mole fraction of hydrogen gradually decreases from 1 to 0, while the mole fractions of nitrogen and water increase from 0 to about 0.79 and 0.21, respectively. Meanwhile, the mole fraction of H, O, and OH radicals reach their maximum values in the reaction zone, tends to the fuel side.

Combining the information from Fig. 76 and Fig. 77, it can be observed that with the increased temperature, the mole fractions of H, O, and OH radicals all increase. The maximum mole fraction of H radical occurs at the highest temperature, while the maximum mole fraction of O and OH radicals lags behind the maximum temperature. As the temperature gradually decreases, maximum values of O and OH radical mole fraction appear. Table. 10 shows the maximum values of the hydrogen-air diffusion flame temperature and radicals mole fraction.

Flame temperature	2182.0 K
H radical mole fraction	0.0241
O radical mole fraction	0.0096
OH radical mole fraction	0.01885
H_2O mole fraction	0.2706

Table. 10: Simulated maximum values of temperature and radical mole fraction in the hydrogen-air diffusion flame.

5.3 Methodology

It is a direct and effective method to analyse the flame spectrum to further investigate the colour of the hygrogen-air diffusion flame. A fibre optical spectrometer was tried in the experiment; however, its highest integration time is too short. The fibre optical spectrometer could record only sodium lines in the hydrogen-air diffusion flame due to their high intensity. Also, it was hard to distinguish weak signals from background noise. Therefore, a spectrograph was used in this work to analyse the flame spectrum. The spectrograph has been used in light wavelength analyses, physics and astronomical studies etc., over the past few decades [91]. The spectrograph is not limited by the integration time, so weak emission lines can be distinguished from the background noise and recorded. Furthermore, spectral lines on grainy images are easier to identify and process. Therefore, the spectrograph would be appropriate for resolving low light emission lines.

Regarding hydrogen combustion under the ambient air condition, several substances are expected to be produced in the process. Hence finding out which substances are participated in the combustion reaction and investigating the light they emit are necessary for analysing the hydrogen flame colour.

When a monochromatic light projects into the spectrograph, mounted-in diffraction grating diffracts the light into various angles depending on their wavelength. The spectrum of the flame could be obtained based on this principle. The data processing and calibration method are as follows: The spectrum was

captured by a camera and recorded in raw format (ARW) to preserve its quality. It is observed that sodium was present in all the studied cases due to its minute presence in the ambient air, resulting in two spectrum lines with relatively significant intensity in the measurements. The theoretical values (in terms of frequency) of these two lines are adopted as a benchmark for calibrating the spectrum samples, i.e., to estimate the frequencies associated with other measured spectrum peaks. Besides, in order to better confirm the involvement of these substances, co-flow was also added as a comparison.

The occurrence of sodium double lines is due to electron transition from different states. The transition from $P_{3/2}$ state to *S* state emits the line at 588.99 nm, and the transition from $P_{1/2}$ state to *S* state emits the line at 589.59 nm [38].

The above mentioned analytical procedures are carried out using a computer program written in Python [92] and third third-party open-source libraries (NumPy [93], scipy [94] and skimage [95] that are well-validated and widely applied in scientific studies. Fig. 78 depicts explains the primary procedures of the Python program.

The Python processing algorithms have high repeatability and accuracy, but some unavoidable errors still exist. One of the primary error sources is considered to be the post-processing of raw measurements. In the Python processing algorithms, Sodium doublet lines were used for calibration. The separation distance between the two lines is 0.597 nm (equivalent to 16 pixels in the image).

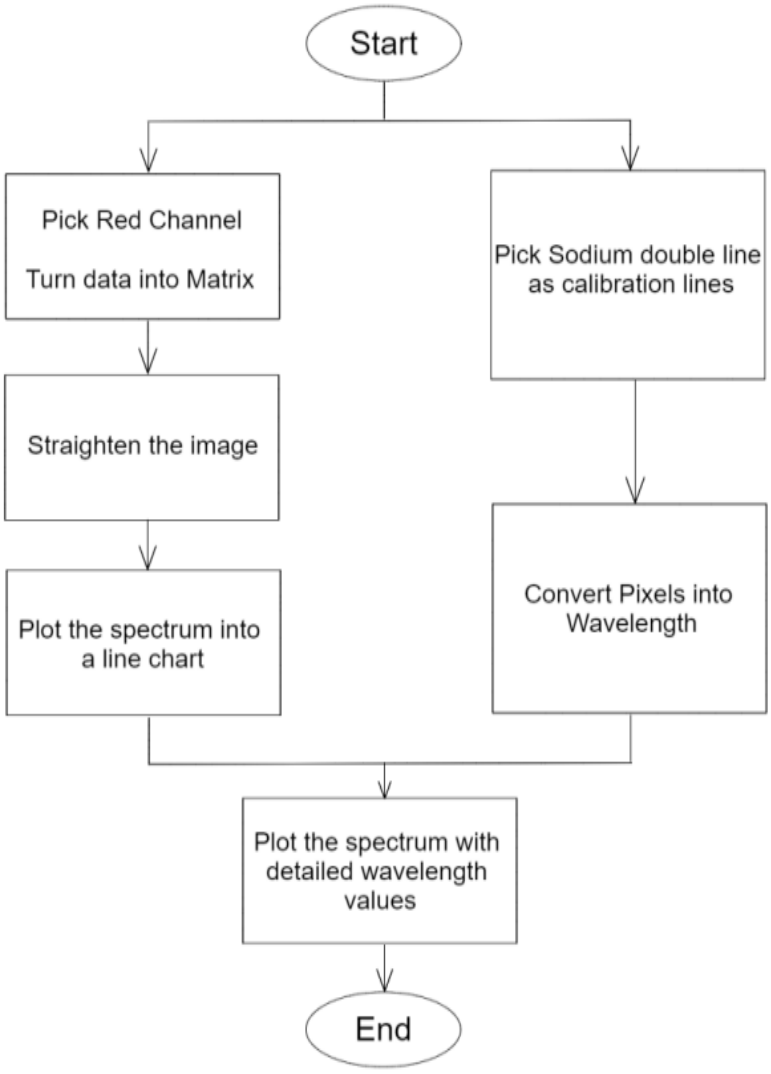

Fig. 78: Key analysis procedures of Python processing algorithms.

The main error comes from the spectrum lines. The width of each line is 16 pixels. So that the error can be worked out as:

$$error\ 1 = \left[\frac{1}{15} - \frac{1}{32+17}\right] \times 0.597 = 0.0276\ nm$$

The error also comes from the difference between the exact position and the adjacent position of each pixel. In this case, the separation distance between the two peaks can be within 17 pixels. Hence, the error could be calculated as:

$$error\ 2 = \left(\frac{1}{15} - \frac{1}{17}\right) \times 0.597 = 0.0047\ nm$$

Therefore, the error for the experiment can be determined at approximately $\pm$0.032 nm.

In addition, to ensure the accuracy of the experiment, the gas was flown through the whole system before ignition for five minutes. It ensures that all the other gas remaining in the system, especially the flow control system, is evacuated and replaced by the experiment gas.

After the wavelength values of these spectral lines are calculated, they are compared with the spectral line database to identify the substances. Hence the substances that contribute to the colour of the hydrogen flame can be estimated.

An extended exposure time of 20 minutes was applied for each experiment trial when the hydrogen flame spectrum was measured to enhance the sampled data.

According to W. F. Barrett, defined in 1872 [1], the hydrogen flame is “reddish-brown”, and the colour of hydrogen flame is red to the naked eye. Therefore, this experiment mainly focuses on analysing the spectral lines in the range of 590 nm to 700 nm.

5.4 Experiment Set-up

Equipment used in this experiment includes burners of different nozzle sizes, a spectrograph, a DLSR camera, a flow control system and fuels. In this sub-section, details of the equipment mentioned above will be shown. Fig. 79 shows the

experimental setup.

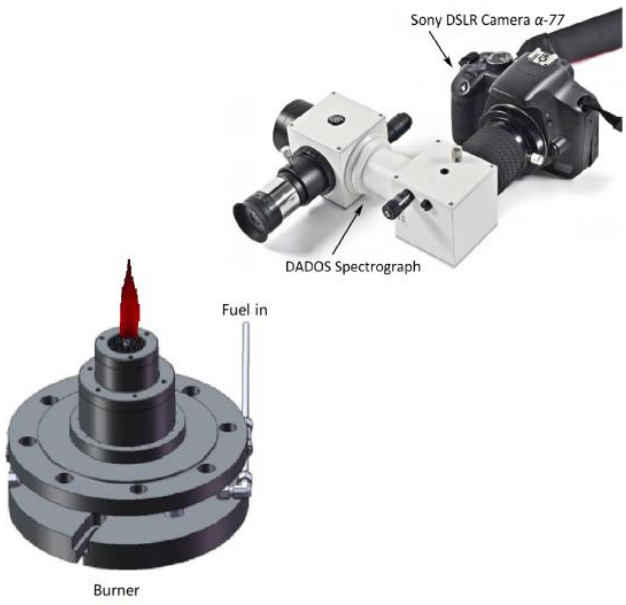

Fig. 79: Hydrogen diffusion flame experimental setup.

Plastic gas pipes were connected to the flow control system, including gas flow meters and a mixing chamber. The gauge controlled the pressure of the gas, and the gas flow rate was controlled by the gas flow meter. Then the gas flew to the burner through another gas pipe. After the gas flow was stable, the gas was ignited at the nozzle of the burner. The burner used in this experiment was the same burner as the previous experiment (Swagelok burner).

The spectrograph nosepiece was set towards the flame, and the focuser was connected to the DSLR camera. The distance between the spectrograph nosepiece and the flame is 10 cm.

All the experiments were carried out in a dark room environment to ensure the accuracy of the spectrum. In the following sub-sections, details of this equipment and gases will be described.

5.4.1 Spectrograph

The spectrograph used in this experiment is a DADOS slit spectrograph manufactured by Badder Planetarium. The spectral resolution of this grating is 4400, and the line resolution is 1.5 Angstroms. This device is designed to be used for obtaining the spectra of various light sources, and in this experiment, it was used to capture the spectra of different flames.

Fig. 80: DADOS slit sepctrograph [57].

The main parts of the spectrograph contain a nosepiece, a slit illuminator, a slit viewer port, a slit viewer port locking screw, a focuser, a focuser locking screw and a grating angle locking screw.

There are three gratings to be chosen from, which are 200, 900 and 1200 lines per mm. More lines per mm mean higher resolution. The default grating is 200 l/mm; however, the resolution was too low to get the accurate spectral value. Hence in this experiment, 1200 l/mm grating was chosen.

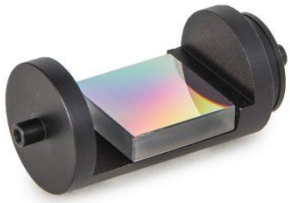

Fig. 81: DADOS 1200 lines/mm diffraction grating [96].

Besides, there are three slits, which are 25 μm, 35 μm and 50 μm. The size of the slits determines the amount of light incident onto the grating. The following image shows an example of the spectrum obtained from these three slits.

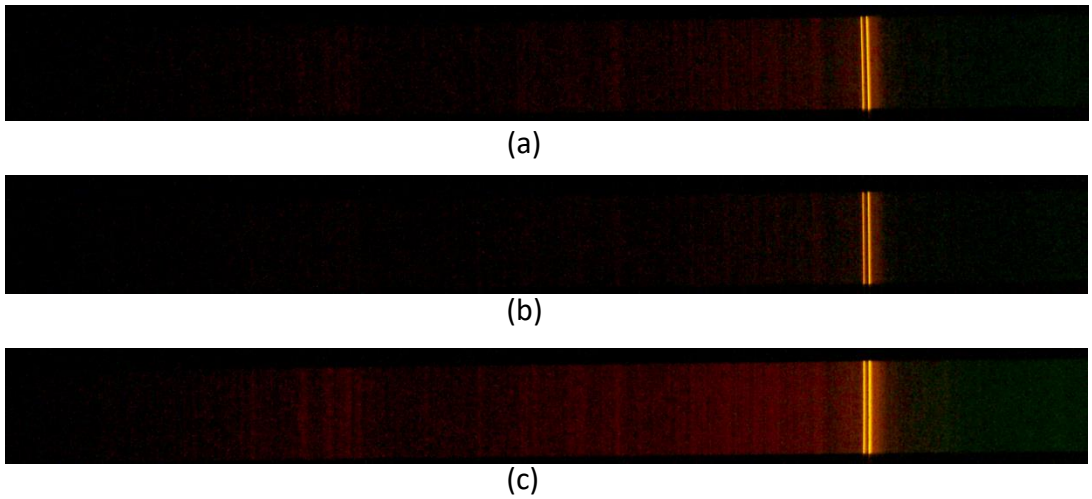

Fig. 82: Different slits size hydrogen diffusion flame spectrum. (a) 25 μm width slit; (b) 35 μm width slit; (c) 50 μm width slit.

Fig. 82(a) is slits of 35 μm, Fig. 82(b) is 25 μm, and Fig. 82(c) is 50 μm. It is evident that the spectral lines are more intense with the 50 μm slit. Hence, the 50 μm slit was used to obtain the spectrum in this experiment.

5.4.2 Camera

The DSLR camera enrolled in this experiment is a Sony $\alpha - 77$ camera. The ISO range of this camera is from 100 to 16000, and the sensor is a 24.3 megapixel Exmor APS-C HD CMOS sensor. The shutter speed range is 1/8000 to 30 seconds. However, an extra remote shutter release is connected to allow a longer exposure time. The spectral resolution of our CMOS camera is 0.035 nm (6000×4000 pixels). In this experiment, a spectrograph was directly connected to the camera; hence no lens was required. The exposure time of each trial is 20 minutes.

Fig. 83: Sony $\alpha - 77$ camera with a SSM lens [97].

5.5 Problems

Although the experiment was designed scientifically and carefully, various problems still remain in the actual practice. This sub-section will discuss these problems and their measures or solutions.

5.5.1 Gas purity

In this experiment, the purity of the gases used is critical, and any kind of

impurities in the gas will affect the result. Although the hydrogen used in this experiment was research-grade high purity, it could get contaminated in the gas pipes, flow control system or equipment. In order to make sure the gas purity, measurements had been taken prior to the experiment.

First is the cleanness of the equipment. The gas pipes used for connecting the gas gauge and the burners were brand new plastic gas pipes. The lab was new, all gas pipelines were built in the building to connect the gas gauge in the lab, and the outdoor gas bottle was new and made of stainless steel. Besides, each component of the burners used was cleaned carefully with an ultrasonic cleaner. After ultrasonically cleaning, these components were also rinsed with distilled water and air-dried. Besides, the flow control system was also kept clean. The hydrogen flow meter was new and was not used for other gas.

Second, the gas was released before the experiment to eliminate the gas left in the gas pipeline before. Also, before each trial, the experimental gas will be discharged for a period of time according to the equivalent ration and flow rate required for the experiment. Such measures ensure the purity of the gas during the experiment.

5.5.2 Darkroom environment

The spectrograph is very sensitive to light, and the intervention of any other light source will affect the final result primarily. Therefore, this experiment requires to be carried out in a completely dark environment to eliminate the influence of other light in the lab.

The experiment was carried out in an enclosed laboratory with no windows to ensure accuracy. However, there were still some light sources that could not be turned off or avoided. For example, the indicator light of the gas sensors and light from the door gap. In order to avoid the influence of these lights, a black fireproof insulation cloth was used to block them. Because all the interfering light sources came from the same direction, the black cloth was set between the experiment set-up and the interfering light sources. After taking such measures, a spectrum was taken under the same conditions as the experiment to ensure no spectrum lines in the captured image. Hence a darkroom environment was created.

5.5.3 Camera noise and Signal-to-noise ratio (SNR)

Because of the long exposure in the experiment, the digital camera generates noise due to overheating. Although the image will be processed for noise reduction in the later stage, reducing the noise during the shooting process will reduce the workload. In order to solve the problem of camera overheating, the camera was turned off for 20 minutes between each trail and allowed to cool down, which significantly reduced the noise generated by the camera.

The camera used in this experiment is a CMOS sensor camera. Its spectral resolution is 0.035 nm (6000×4000 pixels), which allows using sodium double lines for calibration. A longer spectral integration time would let more light incidents into the spectrograph. However, the noise would increase parallelly. Several exposure times were tried to find the appropriate spectral integration time that can achieve enough image signal intensity with an acceptable signal-to-noise ratio. Hence, the spectral integration time chosen in the experiment was a balance of image signal

intensity and signal-to-noise ratio.

5.5.4 Wavelength conversion

The reflection of light in different media is different; hence the wavelength of light is different in the air and vacuum. Ciddor Equation provides a way to convert wavelength between air and vacuum.

The following paragraph with equations (3)-(13) will list and explain the steps of the Ciddor Equation [98] [99] [100].

Step 1: *To convert vacuum wavelength λ into mm.*

$$\boldsymbol{S = 1/\lambda^2} \qquad \textbf{Equation. 28}$$

Step 2: r_{as} *and* r_{vs} *are intermediate results depend on S.* $k_0 = 238.0185$, $k_1 = 5792105$, $k_2 = 57.362$, $k_3 = 167917$; $w_0 = 295.235$, $w_1 = 2.6422$, $w_2 = -0.03238$, $w_3 = 0.004028$.

$$\boldsymbol{r_{as} = 10^{-8} \times [k_1/(k_0 - S) + k_3/(k_2 - S)]} \qquad \textbf{Equation. 29}$$

$$\boldsymbol{r_{vs} = 1.022 \times 10^{-8}[w_0 + w_1 S + w_2 S^2 + w_3 S^3]} \qquad \textbf{Equation. 30}$$

Step 3: XCO_2 *is the* CO_2 *concentration.*

$$\boldsymbol{M_a = 0.0289635 + 1.02011 \times 10^{-8}(XCO_2 - 400)} \qquad \textbf{Equation. 31}$$

$$\boldsymbol{r_{axs} = r_{as} \times [1 + 5.34 \times 10^{-7}(xco_2 - 450)]} \qquad \textbf{Equation. 32}$$

Step 4: Get the compressibility and density components. T *is the temperature in Kelvin,* t *is the temperature in degrees Celsius.* $a_0 = 1.58123 \times 10^{-6}$, $a_1 =$

-2.9331×10^{-8}, $a_2 = 1.1043 \times 10^{-10}$; $b_0 = 5.707 \times 10^{-6}$, $b_1 = -2.051 \times 10^{-8}$; $c_0 = 1.9898 \times 10^{-4}$, $c_1 = -2.376 \times 10^{-6}$.

$$Z_m = 1 - (p/T)[a_0 + a_1 t + a_2 t^2 + (b_0 + b_1 t)x_v + (c_0 + c_1 t)xv^2] + (p/T)^2(d + exv^2) \quad \textbf{Equation. 33}$$

$$\rho_{axs} = p_{R1} M_a / (Z_a R T_{R1}) \quad \textbf{Equation. 34}$$

$$\rho_v = x_v p M_v / (Z_m R T) \quad \textbf{Equation. 35}$$

$$\rho_a = (1 - x_v) p M_a / (Z_m R T) \quad \textbf{Equation. 36}$$

Step 5: Calculation of the index of refraction n.

$$n = 1 + (\rho_a/\rho_{axs}) r_{axs} + (p_a/p_{axs}) r_{vs} \quad \textbf{Equation. 37}$$

Step 6: Convert λ_{vacuum} to λ_{air}.

$$\lambda_{air} = \lambda_{vacuum} / n \quad \textbf{Equation. 38}$$

All the wavelength conversions between vacuum and air are under the condition of 20 ℃, 101.325 kPa, 50% relative humidity and 450 micromoles per mole carbon dioxide content.

5.6 Hydrogen-air diffusion flame spectrum

The spectrum of hydrogen diffusion flame is presented in Fig. 85. The spectrum focuses on the light wavelength ranging from 570 nm to 700 nm. The two most intense peaks were determined as 588.99 nm and 589.59 nm, which are considered

to be the Sodium doublet lines. Fig. 84 is the sodium double lines in the hydrogen-air diffusion flame spectrum.

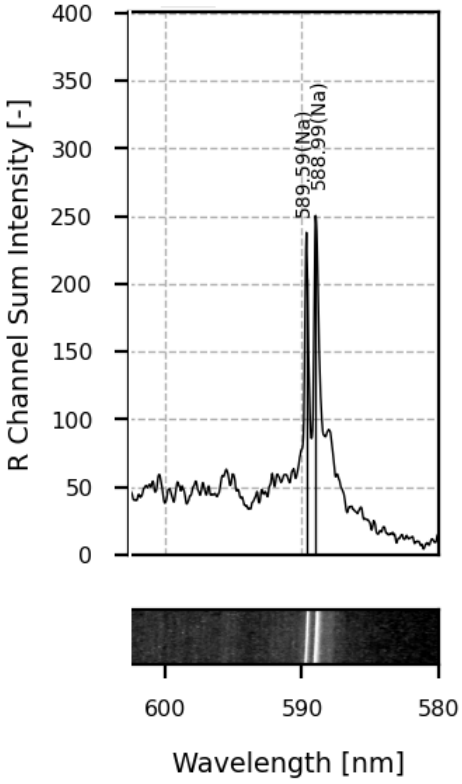

Fig. 84: Sodium double lines in the hydrogen-air diffusion flame spectrum.

As shown in Fig. 84, the full width at half maximum intensity (FWHM) of the sodium double line at 588.99 nm is measured to be 0.31 nm, and 0.41 nm for the line at 589.59 nm.

According to the Doppler broadening, the FWHM can be calculated following:

$$\Delta\lambda_{1/2}^{D} = (7.16 \times 10^{-7})\lambda(\frac{T}{M})^{1/2} \qquad \textbf{Equation. 39}$$

Where T is the temperature of the emitters in Kelvin, and M is the atomic weight in atomic mass unit (amu).

For the resonance broadening, the FWHM can be estimated as:

$$\Delta\lambda_{1/2}^{R} \simeq 8.6 \times 10^{-30}(g_i/g_k)^{1/2}\lambda^2\lambda_r f_r N_i \qquad \textbf{Equation. 40}$$

Where λ is the wavelength of the emission line, λ_r and f_r are the oscillator strength and wavelength of the resonance line, g_i and g_k are the statistical weights of its upper and lower levels, and N_i is the ground state number density.

The broadening sodium doublets can be estimated according to the equations above as a several angstroms and are positively correlated to the flame temperature.

Besides the sodium double line, a cluster of emission lines is observed in the range of 595 nm to 615 nm, as shown in Fig. 85 with a blue rectangle. The other cluster of emission lines exists in the range of 620 nm to 635 nm, which is indicated in the green rectangle. However, it is unknown what material(s) these emission lines correspond to, and they are not reported in the literature. Four distinctive emission lines are observed at a higher frequency range in Fig. 85, ranging from 650 nm to 660 nm. This is highlighted in a white rectangle in Fig. 85. All the spectral lines are located in the red-light range.

Fig. 85: Hydrogen-air diffusion flame spectrum. Blue box: 590 nm to 620 nm; Green box: 620 nm to 650 nm; White box: 650 nm to 660 nm; Yellow box: 660 nm to 700 nm.

As the values of the sodium double lines are known, the values obtained from these two lines were used to get the values of other peaks. The values in the red-light zone were calculated and analysed. The emission lines were divided into two regions

for analysis. As shown in Fig. 85, The cluster of emission lines was shown in the blue box, and the other four distinctive emission lines in the higher wavelength were indicated in the white box.

5.6.1 Emission lines in the range of 590 nm to 620nm

As shown in Fig. 86, there are 13 strong emission lines in the range of 590 nm to 620 nm. They are indicated in the spectrum below with the blue rectangle.

Fig. 86: Spectrum of hydrogen-air diffusion flame in the range of 590 nm to 620 nm (Blue boxed).

The observed emission lines are as follows: 595.044 nm, 595.604 nm, 597.247 nm, 597.769 nm, 599.039 nm, 600.532 nm, 602.997 nm, 604.303 nm, 606.693 nm, 607.290 nm, 609.605 nm, 610.651 nm, and 612.854 nm.

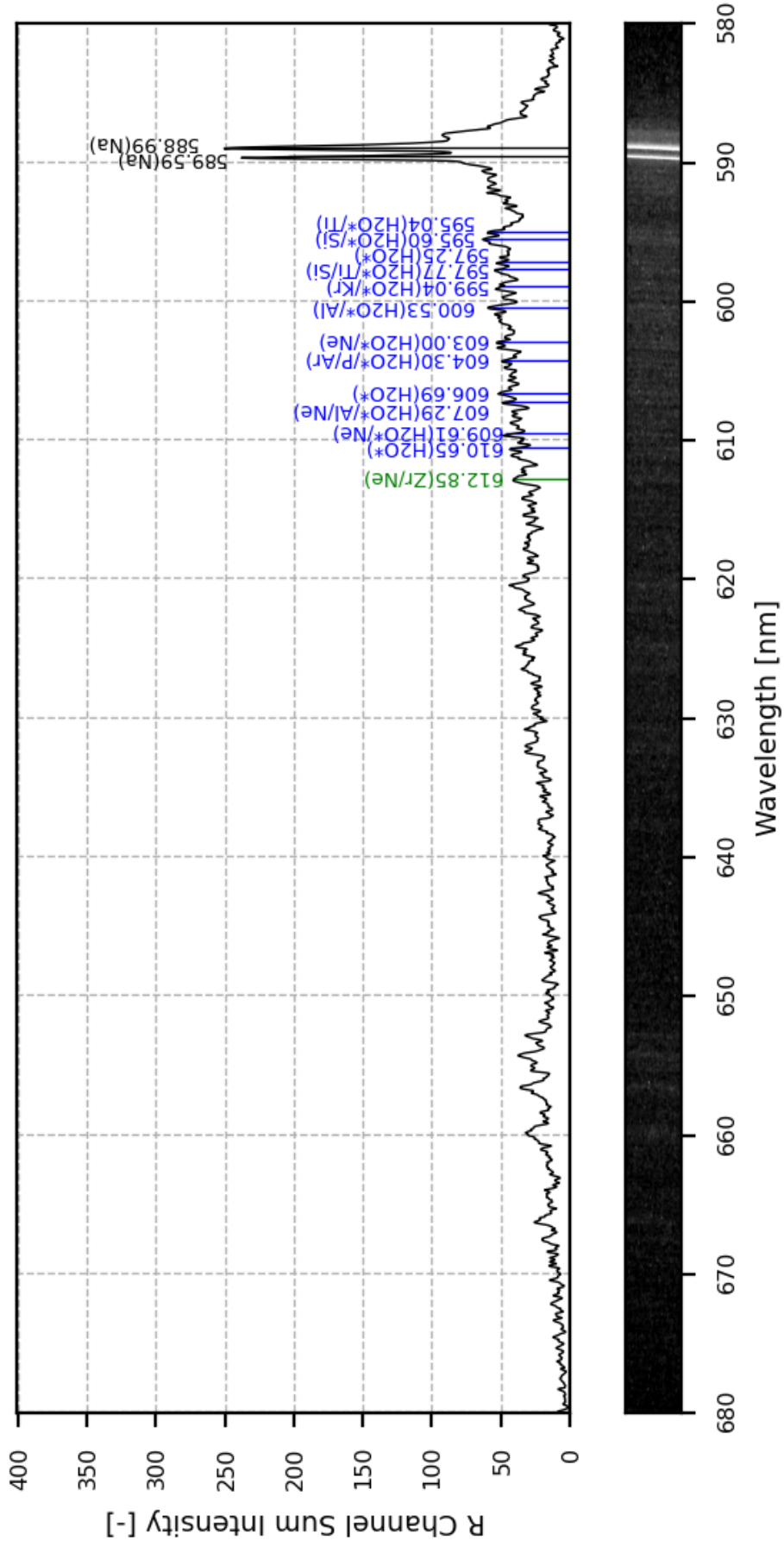

Fig. 87: Hydrogen-air diffusion flame spectrum plot in the range of 590 nm to 620 nm.

These lines are compared to the HITRAN and NIST database to find the possible species that contribute to the red colour of hydrogen diffusion flame. According to the HITRAN database, H_2O, H_2, O_2, OH and NO have emission lines in this wavelength range. Table. 11 list the strong emission lines and the intensity of these species close to the experimental emission lines. The intensity is defined for a single molecule per unit volume at the temperature of 296 K [101]. Wavelengths provided by HITRAN are collected under vacuum conditions. Due to the experiments being conducted in the atmosphere, all the HITRAN wavelengths are converted into wavelengths in air.

Experimental emission line wavelength (nm)	**Species**	**Wavelength in Vacuum (nm)**	**Wavelength in Air(nm)**	**Intensity (cm^{-1}/ ($molecule \cdot cm^{-2}$))**
595.044	**H_2O**	**595.081**	**594.919**	**1.87×10^{-24}**
	H_2O	595.147	594.985	7.05×10^{-25}
	H_2O	595.198	595.036	5.73×10^{-25}
595.604	H_2O	595. 800	595.638	5.86×10^{-25}
	H_2O	595.952	595.790	7.47×10^{-25}
	H_2O	**595.953**	**595.791**	**9.33×10^{-25}**
597.247	H_2O	597.171	597.009	7.44×10^{-25}
	H_2O	**597.300**	**597.138**	**9.97×10^{-25}**
	H_2O	597.675	597.513	9.91×10^{-25}
597.769	**H_2O**	**597.871**	**597.703**	**8.28×10^{-25}**
	H_2O	597.871	597.709	5.35×10^{-25}
	H_2O	597.945	597.782	6.25×10^{-25}
599.039	H_2O	599.094	598.931	5.40×10^{-25}
	H_2O	599.227	599.064	2.37×10^{-25}

	$\boldsymbol{H_2O}$	**599.250**	**599.087**	$\mathbf{6.30 \times 10^{-25}}$
600.532	H_2O	600.631	600.468	1.94×10^{-25}
	$\boldsymbol{H_2O}$	**600.655**	**600.492**	$\mathbf{6.09 \times 10^{-26}}$
602.997	$\boldsymbol{H_2O}$	**603.203**	**603.040**	$\mathbf{3.37 \times 10^{-26}}$
604.303	$\boldsymbol{H_2O}$	**604.533**	**604.369**	$\mathbf{2.18 \times 10^{-26}}$
606.693	$\boldsymbol{H_2O}$	**606.911**	**606.746**	$\mathbf{3.39 \times 10^{-27}}$
607.290	$\boldsymbol{H_2O}$	**607.480**	**607.315**	$\mathbf{2.19 \times 10^{-27}}$
609.605	$\boldsymbol{H_2O}$	**609.679**	**609.513**	$\mathbf{1.72 \times 10^{-27}}$
	H_2O	609.770	609.605	1.71×10^{-27}
610.651	$\boldsymbol{H_2O}$	**610.797**	**610.632**	$\mathbf{2.83 \times 10^{-27}}$

Table. 11: List of species with emission lines close to the experimental wavelength [6] [102].

It could be seen that water contributes to the red flame colour significantly. Almost all the strong emission lines in the range of 590 nm to 620 nm are due to water emission. The intensities of these water emission lines decrease as the wavelengths increase. However, the intensity data provided by HITRAN are based on the RGB three primary colour channels, while the data in the experiments are based on the red channel only. Hence the intensity of the emission lines indicated in the database is just for reference. H_2, O_2, OH, and NO also have emission lines in this wavelength range. However, the intensities of these emission lines are too low compared to emission lines of H_2O.

Apart from species involved in the combustion mechanism, the emission lines of metallic elements and atoms are also considered in this research. Table. 12 lists all the elements and atoms with emission lines close to the experimental lines. The

wavelength of these elements and atoms are from NIST database.

Experimental emission line wavelength (nm)	Elements	Wavelength in Air(nm)
595.044	TI	594.948
	I	595.025
	Cm	595.410
	Ti	**595.316**
595.604	Pm	595.642
	Au	595.697
	Si	**595.756**
597.247	**Xe**	**597.113**
	Tm	597.126
	Eu	597.275
	Ne	**597.627**
	Te	597.680
597.769	**Xe**	**597.646**
	Ti	**597.538**
	Si	**597.893**
599.039	Kr	599.222
	Eu	599.283
600.532	Sb	600.557
	Ce	600.586
	Al	**600.641**
602.997	Eu	602.900
	Ne	**602.997**
604.303	**P**	**604.312**
	Ar	**604.322**
	Ce	604.338
	Pm	604.339
606.693	Pm	606.906
	Sn	606.912
607.290	Ce	607.201

	Al	**607.320**
	Ne	**607.434**
	I	607.498
609.605	In	609.595
	Ne	**609.616**
	Xe	**609.759**
610.651	In	610.866
612.854	**Zr**	**612.746**
	I	612.749
	Ne	**612.845**
	Cs	612.861
	In	612.87
	In	612.94

Table. 12: Wavelength of elements in the range of 590 nm to 620 nm from NIST.

According to NIST, plenty of elements have similar emission lines to the hydrogen-air diffusion flame spectrum. However, not all these elements have the possibility of participating in hydrogen-air combustion. In the hydrogen combustion mechanism, only hydrogen and oxygen elements are involved in the reaction, and hence other elements participate in the reaction and generate emission lines that may arise only from impurities or other components in the air.

Impurities may come from the burner, nozzle, and connections. As mentioned in Chapter 3, the burner used in the experiments is made of cast iron, and the nozzle and connections are made of 304 stainless steel.

Cast iron contains carbon (C), silicon (Si), manganese (Mn), chromium (Cr), molybdenum (Mo), titanium (Ti), vanadium (V), sulfur (S), copper (Cu), nickel (Ni), and zirconium (Zr). Composites of 304 stainless steel include carbon (C), silicon (Si),

manganese (Mn), phosphorus (P), sulfur (S), chromium (Cr), and nickel (Ni).

The atmosphere of the Earth mainly contains nitrogen (N_2), oxygen (O_2), argon (Ar), carbon dioxide (CO_2), neon (Ne), helium (He), methane (CH_4), and krypton (Kr).

Therefore, Table. 13 combines all the possible species to overview the emission lines in the range of 590 nm to 620 nm.

Experimental emission line wavelength (nm)	**Species/Elements**	**Wavelength in Air (nm)**
595.044	H_2O	594.919
	Ti	595.316
595.604	Si	595.756
	H_2O	595.791
597.247	H_2O	597.138
597.769	Ti	597.538
	H_2O	597.703
	Si	597.893
599.039	H_2O	599.087
	Kr	599.222
600.532	H_2O	600.492
	Al	600.641
602.997	Ne	602.997
	H_2O	603.040
604.303	P	604.312
	Ar	604.322
	H_2O	604.369
606.693	H_2O	606.746
607.290	H_2O	607.315
	Al	607.320
	Ne	607.434
609.605	H_2O	609.513
	Ne	609.616

610.651	H_2O	610.632
612.854	Zr	612.746
	Ne	612.845

Table. 13: Possible species or elements contribute to the spectrum of a hydrogen-air diffusion flame from 590 nm to 620 nm.

In the wavelength of 590 nm to 620 nm, plenty of species and elements contribute to the red flame colour of hydrogen-air diffusion flame. H_2O is the primary source of the flame spectrum in this range. In addition to H_2O, titanium, silicon, aluminium, neon, phosphorus, argon, krypton, and zirconium also have strong emission lines. Hence these elements may take part in the hydrogen-air combustion.

5.6.2 Emission lines in the range of 620 nm to 650 nm

According to the spectrum, 7 relatively intense emission lines exist in the range of 620 nm to 650 nm. They are indicated in the green rectangle in Fig. 88. They are 620.433 nm, 622.188 nm, 624.839 nm, 626.445 nm, 630.813 nm, 632.008 nm, and 632.419 nm.

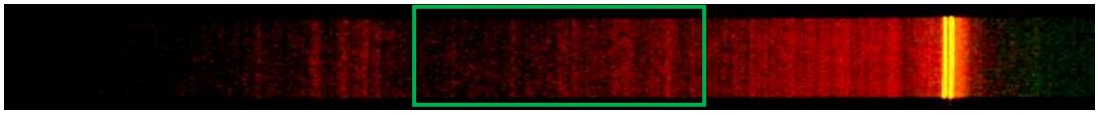

Fig. 88: Spectrum of hydrogen-air diffusion flame in the range of 620 nm to 650 nm (Green boxed).

The same research method was used to analyse the emission lines in the range of 620 nm to 650 nm. These 7 emission lines are compared to the species emission lines in the HITRAN database and elements emission lines in the NIST database.

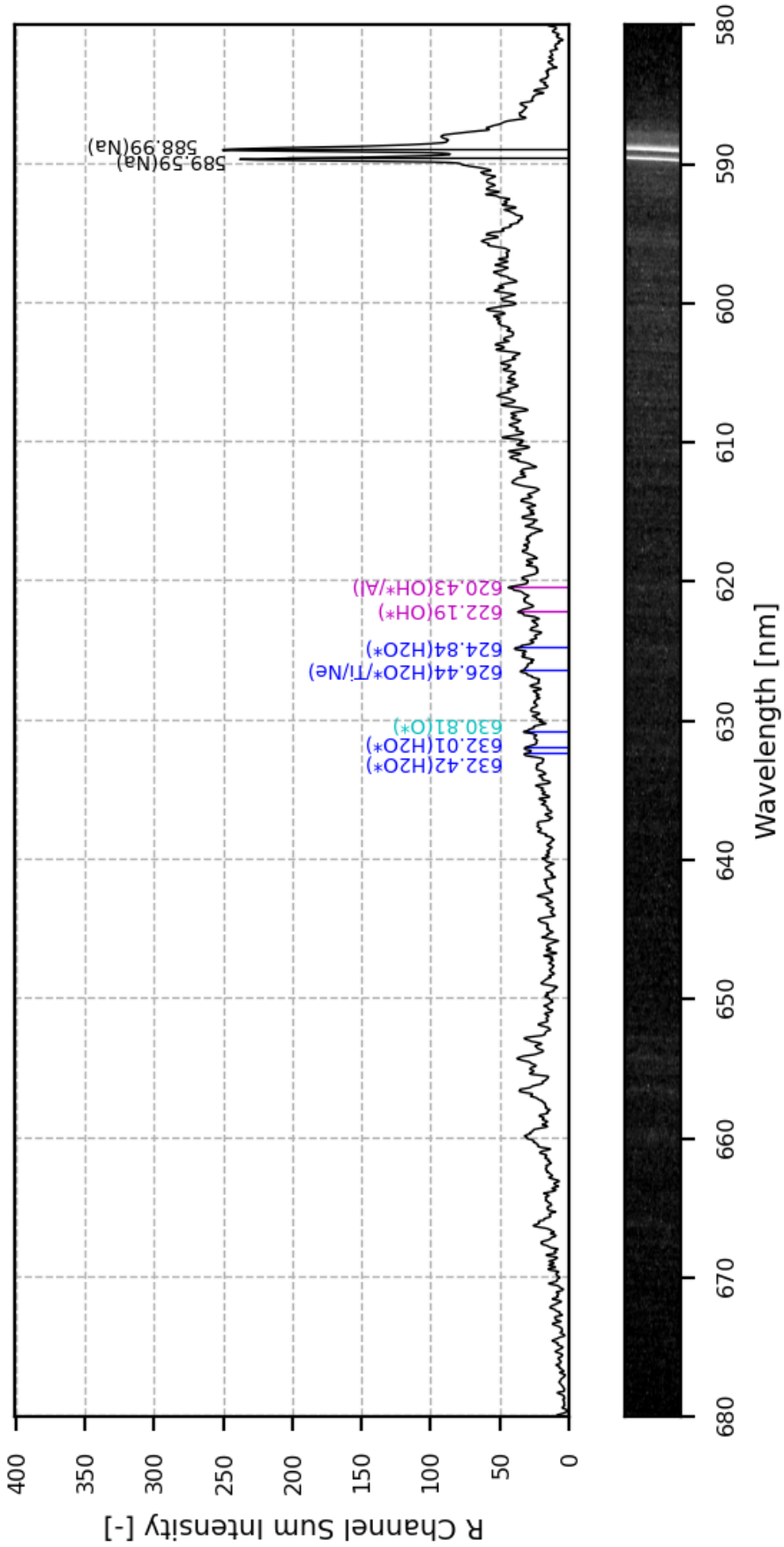

Fig. 89: Hydrogen-air diffusion flame spectrum plot in the range of 620 nm to 650 nm.

Experimental emission line wavelength (nm)	Species	Wavelength in Vacuum (nm)	Wavelength in Air (nm)	Intensity $(cm^{-1}/(molecule \cdot cm^{-2}))$
620.433	$\boldsymbol{OH}$	**620.440**	**620.272**	$\mathbf{1.42 \times 10^{-24}}$
	$\boldsymbol{OH}$	**620.447**	**620.278**	$\mathbf{1.42 \times 10^{-24}}$
	H_2O	620.589	620.421	1.54×10^{-27}
	H_2O	620.642	620.473	2.31×10^{-27}
622.188	H_2O	622.251	622.082	1.79×10^{-27}
	$\boldsymbol{OH}$	**622.343**	**622.174**	$\mathbf{1.51 \times 10^{-24}}$
	$\boldsymbol{OH}$	**622.355**	**622.186**	$\mathbf{1.51 \times 10^{-24}}$
624.839	$\boldsymbol{H_2O}$	**624.964**	**624.794**	$\mathbf{1.36 \times 10^{-26}}$
	H_2O	624.979	624.809	1.01×10^{-27}
	H_2O	625.000	624.830	7.34×10^{-27}
	H_2O	625.083	624.913	6.19×10^{-27}
626.445	H_2O	626.597	626.427	3.34×10^{-26}
	H_2O	626.601	626.430	2.25×10^{-26}
	$\boldsymbol{H_2O}$	**626.633**	**626.463**	$\mathbf{3.83 \times 10^{-26}}$
	H_2O	626.662	626.492	3.50×10^{-26}
630.813	O_2	630.755	630.584	1.40×10^{-26}
	$\boldsymbol{O_2}$	**630.831**	**630.660**	$\mathbf{1.53 \times 10^{-26}}$
	NO	630.855	630.683	2.46×10^{-29}
	NO	630.934	630.763	5.01×10^{-29}
	H_2O	631.006	630.835	9.05×10^{-27}
	H_2O	631.043	630.872	2.98×10^{-27}
	NO	631.063	630.892	2.66×10^{-29}
	O_2	631.163	630.992	1.08×10^{-26}
	O_2	631.238	631.067	1.16×10^{-26}
	OH	631.277	631.104	4.92×10^{-27}
	OH	631.275	631.106	4.80×10^{-27}
632.008	OH	632.015	631.843	1.90×10^{-27}
	OH	632.038	631.866	1.84×10^{-27}
	O_2	632.060	631.889	5.1×10^{-27}
	H_2O	632.268	632.096	1.17×10^{-26}

	O_2	632.134	631.962	5.47×10^{-27}
	H_2O	632.150	631.978	1.06×10^{-25}
	H_2O	632.161	631.989	1.35×10^{-25}
	H_2O	**632.169**	**631.997**	$\mathbf{3.15 \times 10^{-25}}$
632.419	NO	632.301	632.130	2.18×10^{-29}
	OH	632.332	632.160	5.75×10^{-26}
	OH	632.352	632.181	5.73×10^{-26}
	NO	632.406	632.235	3.62×10^{-29}
	O_2	632.550	632.378	3.22×10^{-27}
	H_2O	**632.552**	**632.381**	$\mathbf{2.37 \times 10^{-25}}$
	H_2O	632.560	632.389	1.26×10^{-25}
	H_2O	632.566	632.395	1.28×10^{-25}
	NO	632.588	632.417	1.93×10^{-29}
	O_2	632.622	632.451	3.40×10^{-27}
	H_2O	632.649	632.477	1.86×10^{-27}
	H_2O	632.659	632.487	5.10×10^{-27}
	H_2O	632.685	632.513	2.16×10^{-26}
	NO	632.696	632.524	3.14×10^{-29}
	OH	632.832	632.660	8.44×10^{-26}
	OH	632.876	632.704	8.35×10^{-26}

Table. 14: List of species that participated in the hydrogen-air combustion with similar emission lines to the experiment spectrum in the range of 620 nm to 650 nm.

According to the data from the HITRAN database, H_2O, OH, O_2, NO have emission lines close to the experimental spectrum in the range of 620 nm to 635 nm. Water still plays a critical role in this wavelength range. It contributes to most of the emission lines. OH also contribute mainly to 620.433 nm and 622.188 nm. O_2 has the most vigorous intensity at 630.813 nm.

Moreover, the NIST database also gives information about elements that have

emission lines close to the experimental data.

Experimental emission line wavelength (nm)	Elements	Wavelength in Air (nm)
620.433	**620.146**	**Al**
	620.631	Rb
622.188	622.102	Er
	622.187	Lu
624.839	624.756	Fe
	624.993	La
626.445	**626.110**	**Ti**
	626.225	Eu
	626.650	**Ne**
630.813	630.729	K
	630.829	Pm
632.008	631.806	Xe
	631.837	Pt
632.419	632.236	Pr
	632.384	Pm
	632.658	Pt

Table. 15: List of elements have emission lines close to the experimental spectrum in the range of 620 nm to 650 nm.

Compared to the emission lines in the range of 590 nm to 620 nm, the contribution of these elements is less. According to the source of impurity and the composition of the atmosphere, the possible elements involved in the hydrogen-air combustion and emitted lights are aluminium, titanium, and neon in the range of 620 nm to 635 nm. Referring to the NIST database, aluminium has an emission line at 620.146 nm, which is close to 620.433 nm. Titanium has an emission line at 626.110 nm, and neon has an emission line at 626.650 nm, which is adjacent to 626.445 nm. Apart

from these three elements, other elements listed in Table. 15 should have no possibility of participating in the reaction.

Experimental emission line wavelength (nm)	Species/Elements	Wavelength in Air (nm)
620.433	Al	620.146
	OH	620.278
	OH	620.272
622.188	OH	622.174
	OH	622.186
624.839	H_2O	624.794
626.445	Ti	626.110
	H_2O	626.463
	Ne	626.650
630.813	H_2O	630.660
632.008	H_2O	631.997
632.419	H_2O	632.381

Table. 16: List of possible species or elements that have contributions to the hydrogen-air flame spectrum in the range of 620 nm to 650 nm.

In conclusion, the emission line at 620.433 nm might be due to the emission of aluminium and OH. The emission line at 622.188 nm might be caused by OH and H_2O might contributes to the emission line at 624.839 nm. For the emission line at 626.445 nm, there are three species and elements that might have contributions, which are H_2O, titanium and neon. For emission lines at 630.813 nm, 632.008 nm and 632.419 nm, H_2O might be the primary source.

5.6.3 Emission lines in the 650-670 nm range

It was calculated that the values of the four emission lines indicated in the white

box are 652.88 nm, 654.34 nm, 656.65 nm and 659.94 nm.

According to the records in the HITRAN molecular spectroscopic database [6], H_2 has three intensive emission lines in the range of 650 nm to 670 nm. They are 656.71 nm, 658.70 nm and 661.69 nm. Because the values in the HITRAN database are obtained under vacuum conditions, they need to be converted into values under air conditions. Referring to the National Institute of Standards and Technology (NIST) Engineering Metrology Toolbox, which is based on the Ciddor equation [102] [103]. According to the equations, these three emission lines are equivalent to the wavelength of 656.53 nm, 658.52 nm and 661.51 nm in air.

HITRAN (vacuum)(nm)	HITRAN (air)(nm)
656.71	656.53
658.70	658.52
661.69	661.51

Table. 17: Hydrogen emission line values in the range of 650 nm to 670 nm from HITRAN [6].

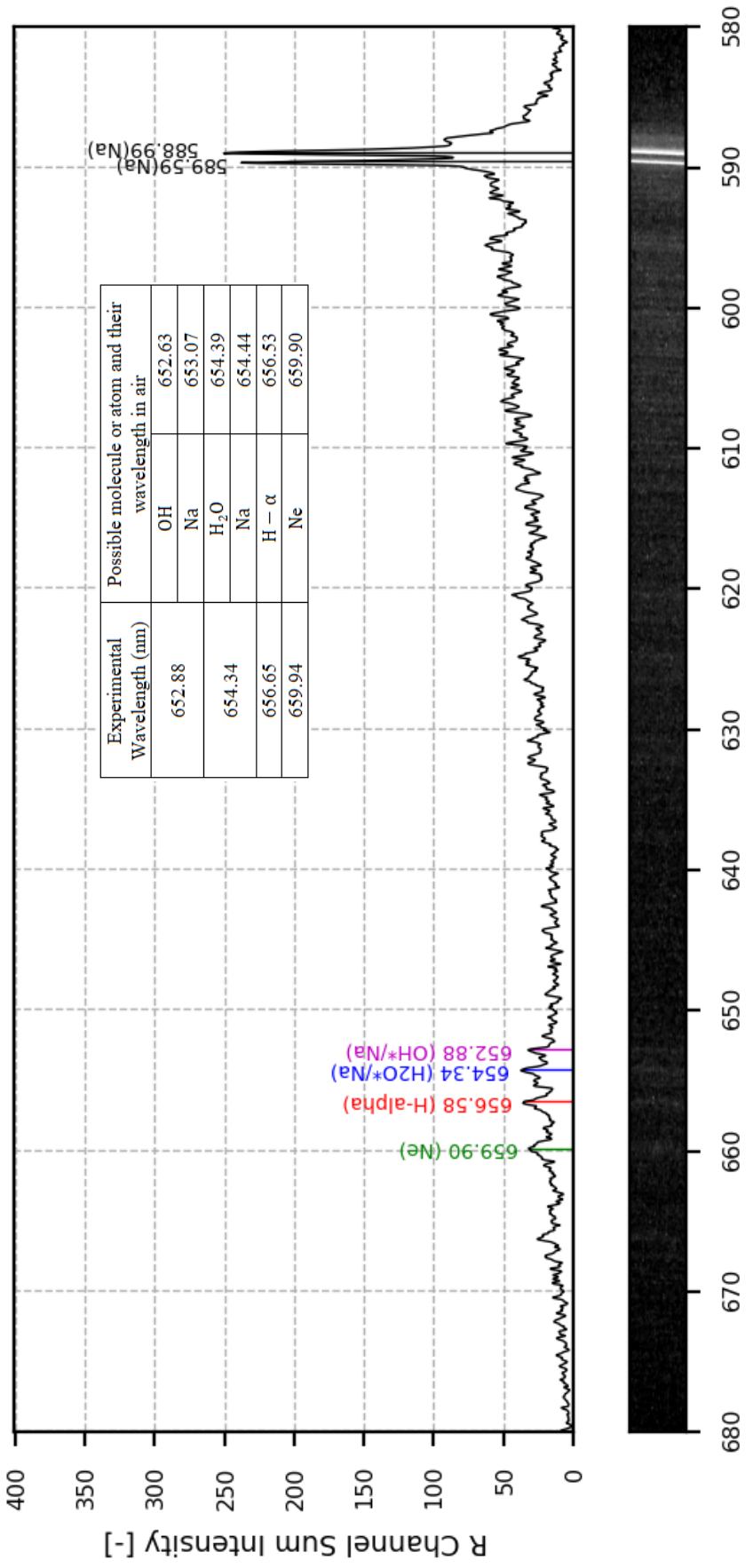

Fig. 90: Hydrogen-air diffusion flame spectrum plot in the range of 650 nm to 660 nm.

The emission band peaks at 656.65 nm match the wavelength of the emission band. The intensity of this emission line is the highest of the three lines. The intensity of emission lines at 658.52 nm (in the air) and 661.51 nm (in the air) provided by HITRAN are 10 times lower than the emission line at 656.53 nm (in the air) [6]. H radicals are abundant during combustion (see Table. 1: Chain reaction of hydrogen combustion [32]., 17 out of 28 elementary reactions with H radicals). Moreover, those excited H radicals may emit light when the electron falls back to the n=2 energy level. Therefore, it is highly likely for $H-\alpha$ to exist in a hydrogen flame. Besides, the intensity of the other two emission peaks is relatively low; hence there is no obvious emission peak in the spectrum.

In addition, the NIST database gives the emission lines of a hydrogen atom in the range of 650 nm to 660 nm.

Wavelength in air (nm)	Transition
656.271	$2P_{1/2}-3D_{3/2}$
656.272	$2P_{1/2}-3S_{1/2}$
656.285	$2P_{1/2}-3D_{3/2}$

Table. 18: Hydrogen atom emission lines between 650 nm and 660 nm from the NIST database [7] [104] [105].

The value of hydrogen emission lines given by HITRAN and NIST have a minor difference, which might be caused by different data collection methods. HITRAN database is a mixture of the experimental and calculated results, while NIST mainly focuses on the theoretical calculation and observation from the solar corona. It is considered that experimental results are usually more accurate, but the results given

by calculation are more completed. Therefore, these two lines might not be recorded in the NIST database.

The cause of the other three emission lines has not yet been explained by any research. However, after comparing the data in the HITRAN database and NIST database in detail, it was found that the emission lines match some relevant elements. In steady-state combustion, hydrogen reacts with oxygen in the air and produces water vapour as the only product [106].

In the mechanism of hydrogen-air combustion, H, H_2, O, O_2, OH, N_2, HO_2, H_2O, and H_2O_2 are involved. The emission spectra of these compositions between 650 nm and 670 nm are also considered. Referring to the HITRAN database, H_2O has three relevant high-intensity emission peaks in this range. They are 651.65 nm, 654.57 nm and 655.48 nm under vacuum conditions [6]. Converting to wavelength in ambient air, they are 651.48 nm, 654.39 nm and 655.30 nm, respectively. Among these three emission lines, 654.39 nm is very close to the value of 654.34 nm in the experimental hydrogen spectrum recorded.

Besides, OH also has two intense emission peaks. They are 652.81 nm and 652.92 nm in vacuum [6], which is equal to 652.63 nm and 652.74 nm in the air. These two peaks match 652.88 nm in the hydrogen-air flame spectrum. Except for H_2O and OH, the remaining species have no emission peaks in the range of 650 nm to 660 nm.

Molecule	In vacuum (nm)	In air (nm)
H_2O	651.65	651.48
OH	652.81	652.63
OH	652.92	652.74

H_2O	654.57	654.39
H_2O	655.48	655.30

Table. 19: High-intensity emission line wavelength in the range of 650 nm to 660 nm from HITRAN database.

In addition to the products produced in the reaction, pollutants in the environment may also contribute to the reddish colour of a hydrogen flame. Referring to the NIST database, Sodium has emission peaks at 653.07 nm and 654.44 nm in the air [7]. These two emission lines match the peaks at 652.88 nm and 654.34 nm. Besides, Nickel has an emission line at 659.90 nm in the air [7]. This emission line matches the peak at 659.94 nm in the experiment spectrum.

Atom	In air (nm)
Na	653.07
Na	654.44
Ne	659.90

Table. 20: High-intensity emission line wavelength near 656 nm from NIST.

5.6.4 Emission lines in the range of 660 nm to 700 nm

Besides the cluster of emission lines in the range of 595 nm to 635 nm and the four intense lines in the range of 650 nm to 660 nm, there are two strong lines between 660 nm and 700 nm, and they are 666.246 nm and 667.478 nm respectively. The same research method was applied to compare the emission lines of species and elements possibly involved in the hydrogen-air combustion process with the experimental emission lines.

Fig. 91: Spectrum of the hydrogen-air diffusion flame in the range of 660 nm to 700 nm (Yellow Boxed).

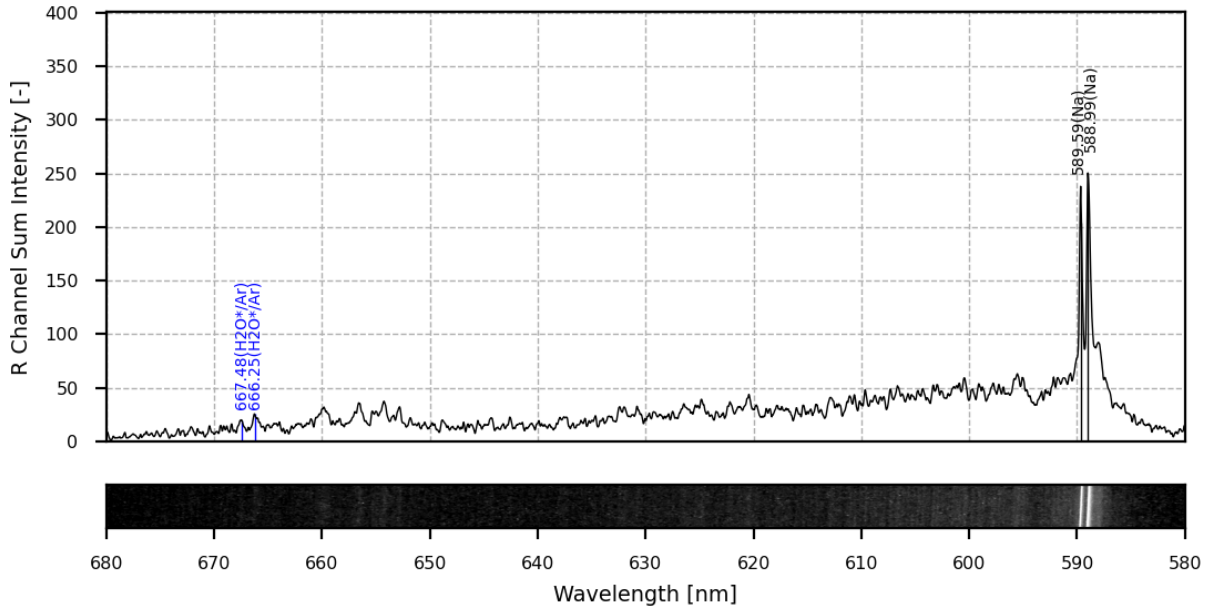

Fig. 92: Hydrogen-air diffusion flame spectrum plot in the range of 660 nm to 700 nm.

According to the HITRAN database, the only species that have intense emission lines within the range of 666 nm and 668 nm is H_2O. Apart from H_2O, OH, NO, and H_2 also have emission lines close to 666.246 nm and 667.478 nm. However, the intensity of these emission lines is much lower than H_2O, hence they are not included in the contribution.

There is an emission line of H_2O at 666.187 nm with the intensity of 6.37×10^{-26}, and 666.557 nm with the intensity of 4.46×10^{-26}. These two lines are close to the

experimental lines at 666.246 nm. H_2O also has an emission line at 667.112 nm with an intensity of 4.90×10^{-26}, which is close to 667.478 nm.

Besides the species, elements are considered as well. Table. 21 below lists all the elements with emission lines in the range of interest.

Experimental emission line wavelength (nm)	Elements	Wavelength in Air (nm)
666.246	Pm	666.168
	Ar	**666.636**
667.478	Ba	667.527
	Ar	**667.728**
	Pm	667.747
	Cf	667.790

Table. 21: List of elements with emission lines close to the experimental spectrum in the range of 660 nm to 700 nm.

As mentioned in section 5.6.1, the only element that might have contributed to the hydrogen-air flame emission lines in this range is argon from the atmosphere.

Experimental emission line wavelength (nm)	Elements	Wavelength in Air (nm)
666.246	H_2O	666.187
	H_2O	666.557
	Ar	666.636
667.478	H_2O	667.112
	Ar	667.728

Table. 22: List of possible species or elements that contribute to the hydrogen-air flame spectrum in the range of 660nm to 700 nm.

5.6.5 Integration of H_2O, OH, O and $H-\alpha$ peaks

In this section, an analysis of the intensity of H_2O, OH, O, and $H-\alpha$ in the red spectral region of the hydrogen diffusion flame is conducted. Based on the previously determined most probable species for each peak, the peaks identified as H_2O, OH, O, and $H-\alpha$ are integrated. Because the obtained emission lines in the experiment are determined by the values of each pixel in the red channel of the captured flame spectrum, the integration of these emission peaks represents the intensity of their R channel values. The integration of these R channel values is positively correlated with the intensity of the emission peaks.

Experimental emission line wavelength (nm)	Value of integrati-on	Experimental emission line wavelength (nm)	Value of integrati-on	Experimental emission line wavelength (nm)	Value of integrati-on
595.04	20.9234	**595.6**	31.2446	**597.25**	20.1291
597.77	26.2951	**599.04**	25.2884	**600.53**	17.9924
603.00	15.1004	**604.30**	13.9601	**606.69**	19.4754
607.29	22.9492	**609.61**	17.0091	**610.65**	14.5169
624.84	14.6967	**626.44**	9.9211	**632.01**	10.22
654.34	27.8274	**666.25**	13.6666	**667.48**	10.4282

Table. 23: Integration of experimental H_2O emission lines in the hydrogen-air diffusion flame.

Experimental emission line wavelength (nm)	Value of integration
620.43	30.1906
622.19	25.4031
652.88	16.7311

Table. 24: Integration of experimental OH emission lines in the hydrogen-air diffusion flame.

Table. 23 and Table. 24 shows the integration of the H_2O and OH emission lines in the experimental hydrogen-air diffusion flame. To obtain the total intensity of the emission lines caused by H_2O and OH in the spectral range of 590 nm to 700 nm, the integrals for each emission line are summed. The total integration for H_2O lines is 331.64, and 72.32 for OH lines.

Additionally, the integration values of the O emission line at 630.81 mm and $H-\alpha$ emission line at 656.58 mm are 15.7617 and 44.6635 respectively.

5.7 Conclusion

In this chapter, details of the experimental setup have been discussed. The set-up contains a spectrograph, three burners, and a DSLR camera. The fuel gas used in this experiment was high purity hydrogen. The equipment settings used in the experiment include DSLR camera shuttle speed, ISO and exposure time. The methodology of this experiment has also been given. It contains the working principle of the spectrograph, the calculation of the spectrum and the match of these captured spectral lines with the substance. In addition, problems that may occur during the experiment and their solutions or measures taken are also described in this chapter. This experiment method is considered reasonable and accurate.

In conclusion, the hydrogen-air diffusion flame colour is affected by several species and elements. Among all the species that participate in the combustion process, H_2O, H_2, O_2, OH, and NO have contributions to the emission lines. Especially H_2O, it has a large number of emission lines in the red colour range according to the

HITRAN database. Moreover, other species might possibly participate in the reaction, including NO_2, N_2O, NO, O_3, HO_2, H_2O_2, NH_3, HNO_3, O, N_2 have no emission lines in this wavelength range.

In the wavelength of 590 nm to 620 nm, the main source of emission lines is H_2O. All the 13 emission lines (595.044 nm, 595.604 nm, 597.247 nm, 597.769 nm, 599.039 nm, 600.532 nm, 602.997 nm, 604.303 nm, 606.693 nm, 607.290 nm, 690.605 nm, 610.651 nm and 612.854 nm) might be caused by the emission of water vapour. Also, in the wavelength of 620 nm to 635 nm, there are 4 out of 7 emission lines might mainly be caused by H_2O, which are at 624.794 nm, 626.463 nm, 631.997 nm and 632.381 nm. Besides H_2O, OH and O_2 have strong emission lines at 620.272 nm, 620.278 nm, 622.174 nm, 622.186 nm, and 630.660 nm. There are two relative intense emission lines for emission lines in the range of 660 nm to 700 nm. H_2O might be one of the possible sources as well.

In addition to the species that participated in the combustion process, elements from the impurities and the atmosphere could also be involved in the reaction. By comparing with the NIST database, the possible elements that contribute to the spectrum were picked up and analysed. There are two main possible impurity sources, the cast iron made burner, and the 304 stainless steel made nozzle. Hence the elements contained in this equipment and atmosphere were considered to contribute to the experimental emission lines. These elements include titanium, silicon, neon, aluminium, phosphorus, argon, and zirconium.

In the wavelength range of 590 nm to 670 nm, there are many products or pollutants that produce emission peaks, resulting in the red flame of hydrogen. The

four emission lines ranging from 650 nm to 670 nm are identified in this study. The spectrum peak at 652.88 nm might be OH or sodium emission line. The peak at 654.34 nm might be H_2O or sodium emission line. The peak at 659.94 might be the emission line of Nickel, which may come from the stainless steel of the burner nozzle. The current hydrogen-air combustion mechanism does not consider any excited species, and the excited species should be investigated in the future because the emission band at 656.65 nm is highly possible to be $H-\alpha$. Although the colour of hydrogen diffusion flame is a complex combination, $H-\alpha$ emission high-possibly plays a non-negligible role in the faint reddish colour of a diffusion hydrogen flame. It also indicates that hydrogen atoms are very likely to be excited in the combustion process. Therefore, the mechanism could be improved with further study on the topic of excited hydrogen atoms.

The observation of $H-\alpha$ emission supplies a possibility for a new diagnostic method in terms of the combustion of hydrogen-containing gaseous fuel. The intensity of the emission lines produced by $H-\alpha$ in a hydrogen-containing fuel flame can be used for diagnostics and monitoring purposes.

Chapter 6: Hydrogen-air diffusion flame with co-flow spectrum analysis

6.1 Introduction

The previous chapter focused on analysing the hydrogen-air diffusion flame spectrum in the range of 590 nm to 700 nm. The possible species or elements which may cause the emission lines in the wavelength range were listed. To further verify these emission lines, air and oxygen co-flow with different flow rates were added to the hydrogen-air diffusion flame.

The addition of air and oxygen co-flow would cause some part of the flame combust similar to the condition of stoichiometric premixed flame. It would lead to an increase to the local temperature of the flame. According to I. Glassman *et al*., a premixed flame would have a highest temperature under the stoichiometric condition. Furthermore, at the stochiometric mixture, the flame temperature is affected by the oxidizers. The flame temperature of hydrogen/air mixture at stochiometry is approximately 2300 K , while the flame temperature of hydrogen/oxygen mixture is 3080 K [107]. When oxygen is used as a co-flow, the

temperature of the hydrogen diffusion would be higher than that of the flame with air co-flow. Higher flame temperature might result in more species and elements being excited and emitted. Therefore, the spectra of hydrogen diffusion flame with air and oxygen co-flow are studied.

In this chapter, the Chemkin model of hydrogen-air diffusion flame with air co-flows have been developed. The spectrum of the hydrogen-air diffusion flame with air and oxygen co-flow will be captured using the same experimental methodology and setups as in the previous chapter. Since there was no co-flow involved in the previous hydrogen-air diffusion flame, the settings of the co-flow used in this experiment will be introduced in this chapter. The spectrum of the flame with co-flow will be analysed and compared with the spectrum of the hydrogen diffusion flame. According to the combustion mechanism of hydrogen, the emission lines of species that participate in the reaction in this wavelength band are compared with these four emission lines. The data of the emission lines of the species are collected from the HITRAN database and converted into the wavelength in the air according to Ciddor's equations. Besides the species involved in the combustion mechanism, elements with emission lines close to those of the hydrogen-air diffusion flame with co-flows will also be analysed whether they might be involved in the reaction. The wavelength of the elements is referred to in the NIST database. The similarities and differences between these spectra will be discussed.

6.2 Chemkin model

In this section, the Chemkin models of the hydrogen-air diffusion flame with different air co-flow conditions will be shown. The parameters used in the simulation are the same as those of the non-co-flow hydrogen diffusion flame metioned in the previous chapter. The highest temperature and mole fraction of radicals of the co-flowed flame will be compared with the no co-flow flame.

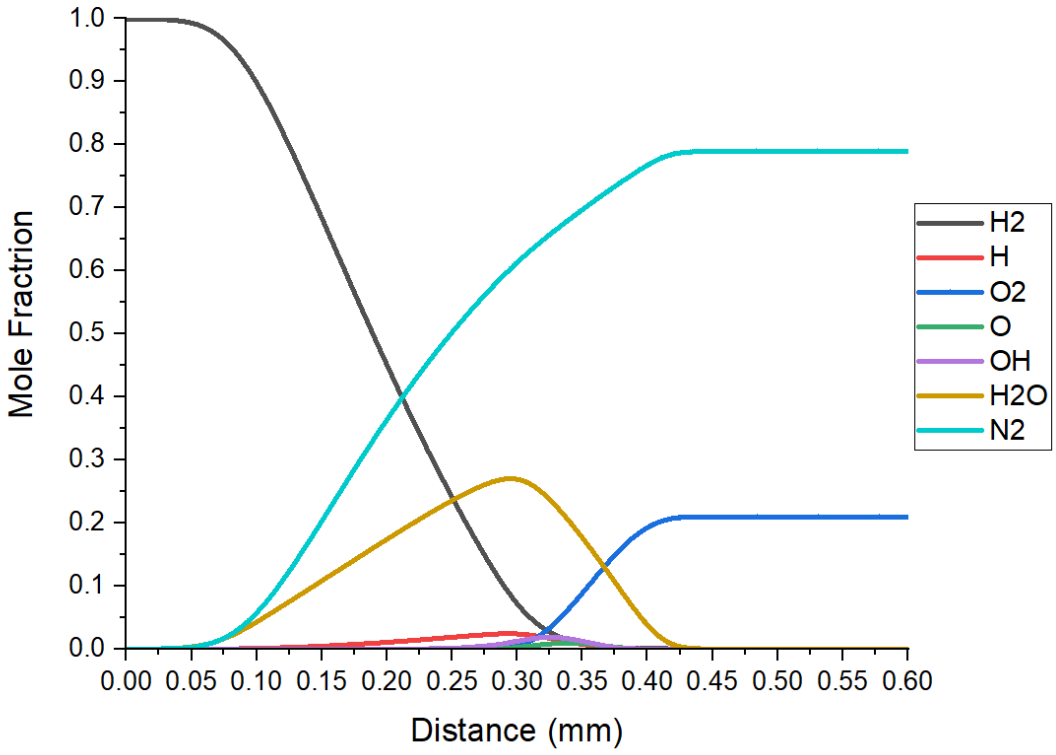

Fig. 93: Mole fraction of species in the hydrogen-air diffusion flame with $6.5\ l/min$ air co-flow simulated by CHEMKIN.

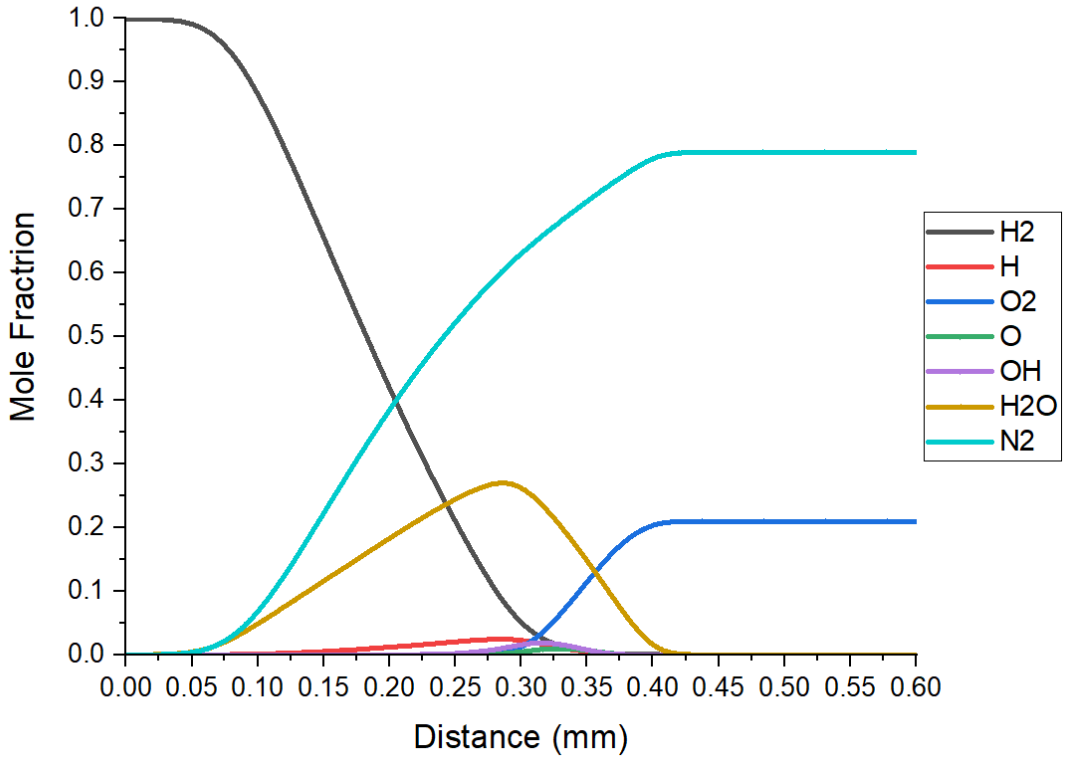

Fig. 94: Mole fraction of species in the hydrogen-air diffusion flame with $13\ l/min$ air co-flow simulated by CHEMKIN.

The mole fraction of species in hydrogen diffusion flames under different air co-flow conditions are shown in Fig. 93 and Fig. 94. The variations in mole fraction of each substance in the flame reaction zone follow a similar trend to that of a non-co-flow hydrogen diffusion flame.

Fig. 95, Fig. 96, and Fig. 97 respectively show the comparisons of mole fraction distributions of H, O and OH radicals in the hydrogen-air diffusion flame under different air co-flow conditions.

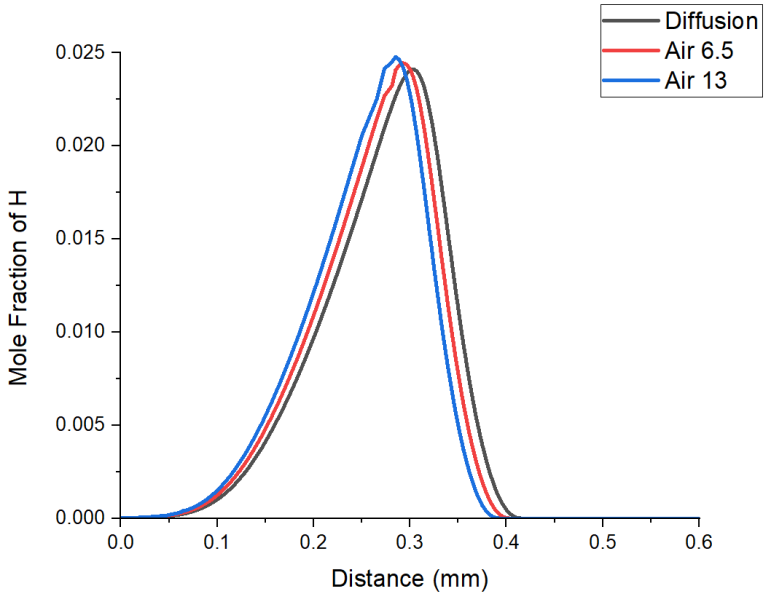

Fig. 95: The comparison of H radical mole fraction in hydrogen diffusion flame with different co-flow conditions.

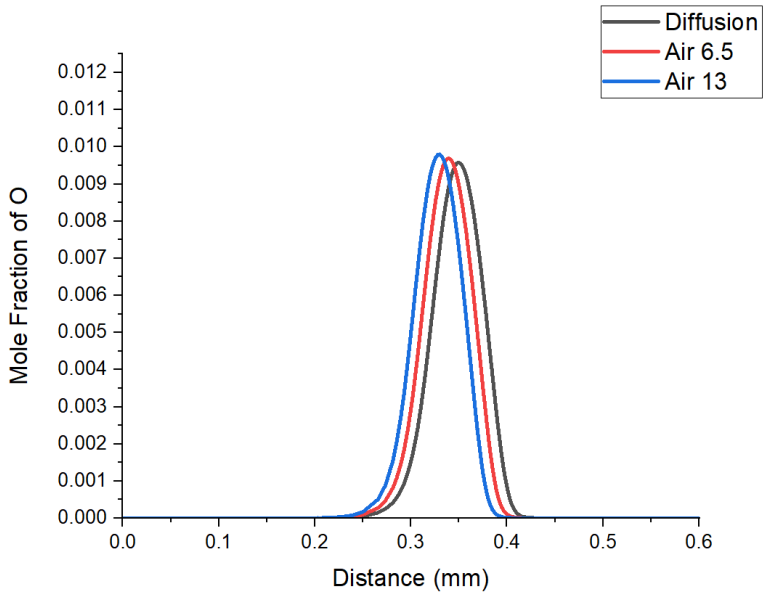

Fig. 96: The comparison of O radical mole fraction in hydrogen diffusion flame with different co-flow conditions.

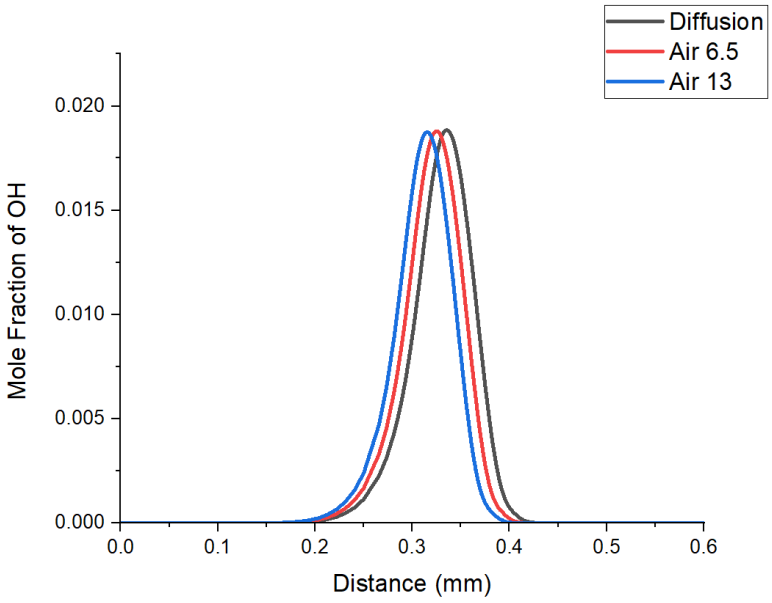

Fig. 97: The comparison of OH radical mole fraction in hydrogen diffusion flame with different co-flow conditions.

It can be observed that in the presence of air co-flow, the mole fraction of H and O radicals in the hydrogen-air diffusion flame are higher compared to the flame without co-flow. The mole fractions of H and O radicals are highest at the $13\ l/min$ air co-flow flame and lower at the $6.5\ l/min$ air co-flow flame, while the non-co-flow flame has the lowest. However, the maximum mole fraction of OH radical remains relatively consistent across the three co-flow conditions.

Table. 25 is the simulated maximum values of temperature and radical mole fraction in the hydrogen-air diffusion flame with different air co-flow conditions. It can be observed that the temperature of the non-co-flow hydrogen-air diffusion flame is higher compared to the air co-flow flames. The air co-flow rate and the flame temperature exhibit a negative correlation. As the flow rate of air co-flow increases, the flame temperature decreases.

Flame type	Temperature (K)	H mole fraction	O mole fraction	OH mole fraction	H_2O mole fraction
Non-co-flow	2182.0	0.0241	0.0096	0.01885	0.2706
$\mathbf{6.5}\ \boldsymbol{l/min}$ air co-flow	2174.3	0.0245	0.0097	0.01879	0.2702
$\mathbf{13}\ \boldsymbol{l/min}$ air co-flow	2166.8	0.0248	0.0098	0.01874	0.2699

Table. 25: Simulated maximum values of temperature and radical mole fraction in the hydrogen-air diffusion flame with different air co-flow conditions.

6.3 Spectrum of hydrogen-air diffusion flame with air co-flow at 6.5 l/min

In this section, the spectra of hydrogen-air diffusion flame with air co-flow at 6.5 l/min $(10.83\ m^3/s)$ in the wavelength range of 590 nm to 700 nm will be shown and analysed.

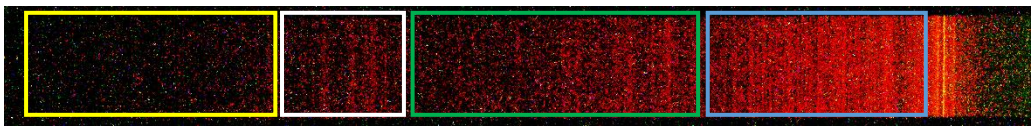

Fig. 98: Spectrum of the hydrogen-air diffusion flame with 6.5 l/min air co-flow in the wavelength of 590 nm to 700 nm.

Fig. 98 is the spectrum of the hydrogen-air diffusion flame with 6.5 l/min air co-flow. In order to present the results more clearly, the spectrum of this wavelength range will be divided into four parts for analysis. The parts are shown in different colour boxes in the figure.

6.3.1 Emission lines in the range of 590 nm to 620 nm

In this sub-section, the emission lines from 590 nm to 620 nm will be analysed. This part of the spectrum is indicated in a blue box in the spectrum. The possible elements and species that might contribute to the emission lines will be identified and listed.

It could be noticed from the spectrum plot (Fig. 99) that the double lines of sodium have the highest intensity in the image. However, their relative intensities become weaker compared to the hydrogen-air diffusion flame spectrum. There are 13 strong emission lines in the wavelength range of 590 nm to 620 nm. These emission lines are 591.27 nm, 595.49 nm, 597.28 nm, 598.67 nm, 600.42 nm, 603.33 nm, 604.71 nm, 606.66 nm, 608.82 nm, 609.64 nm, 611.06 nm, 612.82 nm and 617.71 nm.

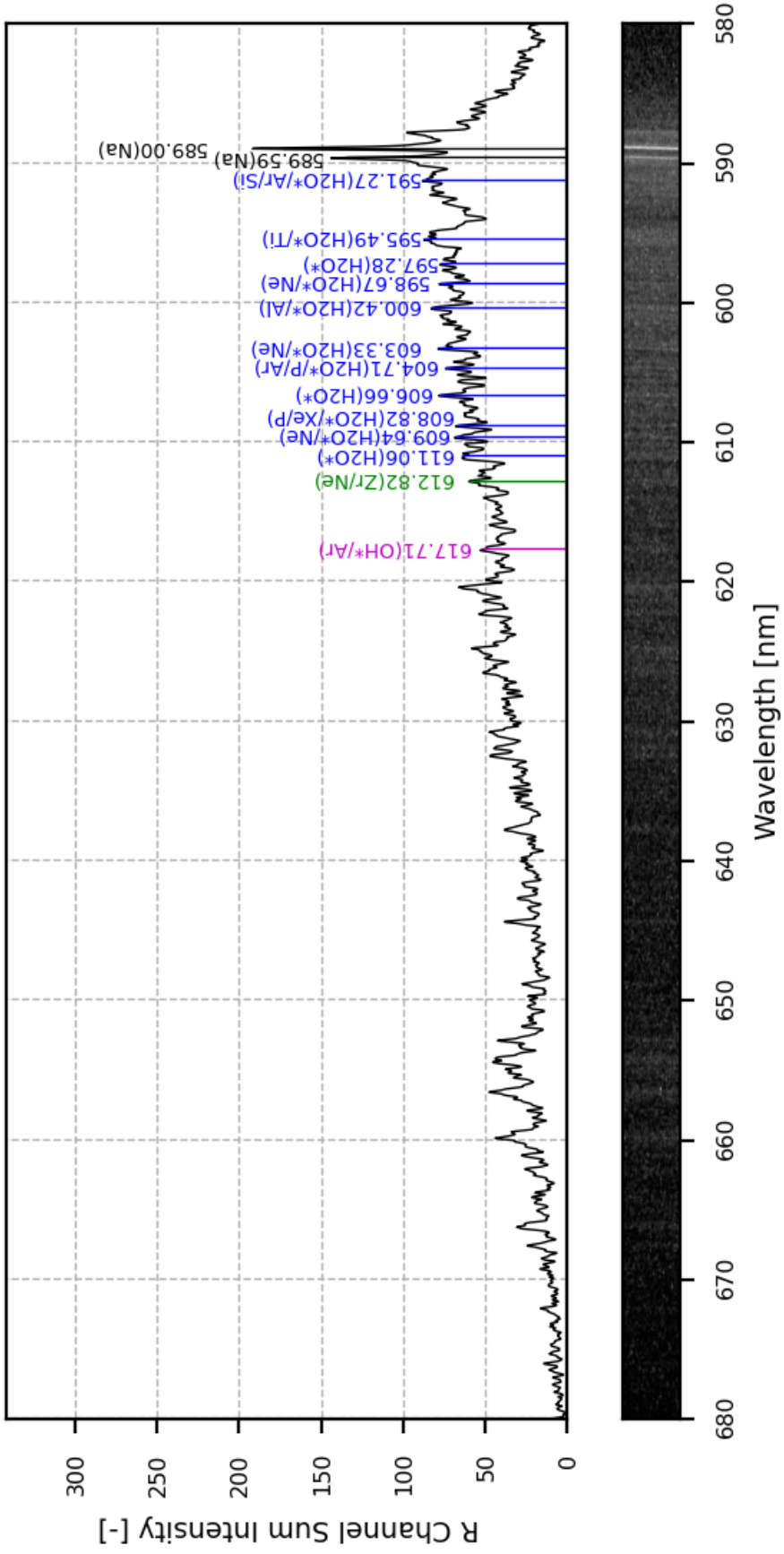

Fig. 99: Hydrogen-air diffusion flame with 6.5 l/min air co-flow spectrum plot in the wavelength of 590 nm to 620 nm.

Compared to the hydrogen-air diffusion flame spectrum, there are four new emission lines, which are 591.27 nm, 598.67 nm, 608.82 nm and 617.71 nm. Species and elements with similar emission lines are listed in the tables below.

Experimental emission line wavelength (nm)	Species	Wavelength in Vacuum (nm)	Wavelength in Air (nm)	Intensity $(cm^{-1}/(molecule \cdot cm^{-2}))$
591.27	H_2O	591.43	591.27	3.64×10^{-25}
598.67	H_2O	598.87	598.70	4.04×10^{-25}
608.82	H_2O	609.02	608.86	2.46×10^{-27}
617.71	OH	617.81	617.64	1.07×10^{-24}
	OH	617.79	617.63	1.07×10^{-24}

Table. 26: List of species with their emission lines close to the extra experimental emission lines in the range of 590 nm to 620 nm.

Experimental emission line wavelength (nm)	Elements	Wavelength in Air (nm)
591.27	**Ar**	**591.21**
	Si	**591.52**
	U	591.54
	In	591.54
598.67	Pr	598.61
	Pr	598.71
	Pr	598.73
	Ne	**598.79**
608.82	Eu	608.38
	Tc	608.52
	P	**608.78**
	V	609.02
	Ce	609.32

	Xe	609.35
617.56	**Ar**	**617.23**
	Eu	617.31
	Xe	617.83
	Eu	617.88
	Xe	617.97

Table. 27: List of elements with their emission lines close to the extra experimental emission lines in the range of 590 nm to 620 nm.

The possible sources of contaminants may be attributed to the emission lines. These sources include the elements contained in the burner, which is made of cast iron; in the nozzle, which is made of stainless steel; and from the atmosphere. Therefore, the elements included in these contamination sources in Table. 28 are considered to be likely contributed to the flame colour.

Experimental emission line wavelength (nm)	Elements/Species	Wavelength in Air (nm)
591.27	Ar	591.21
	H_2O	591.27
	Si	591.52
598.67	H_2O	589.70
	Ne	598.79
608.82	P	608.78
	H_2O	608.82
617.56	Ar	617.23
	OH	617.63
	OH	617.64

Table. 28: List of elements and species with their emission lines close to the extra experimental emission lines in the range of 590 nm to 620 nm.

It can be noticed that the main species that contributed to these four extra emission lines are H_2O and OH. Due to the addition of air co-flow, when the hydrogen was released from the nozzle, the hydrogen on the outside would mix more with the air. Thus, the combustion of hydrogen-air diffusion flame would be more sufficiently with the air co-flow. As the product and indirect product of the hydrogen diffusion combustion, the production of H_2O and OH would be increased. Therefore, these four different emission lines in the air co-flow flame might become apparent due to this reason.

6.3.2 Emission lines in the range of 620 nm to 650 nm

Compared to the wavelength range of 590 nm to 620 nm, the number of emission lines in the range of 620 nm to 650 nm is less. They are indicated in the green square in Fig. 100.

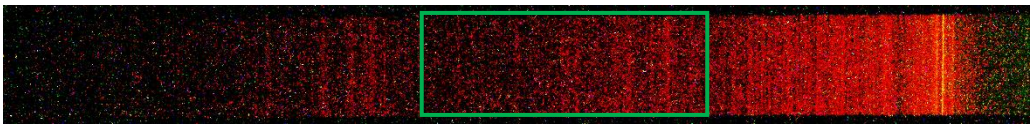

Fig. 100: Spectrum of the hydrogen-air diffusion flame with 6.5 l/min air co-flow in the wavelength of 620 nm to 650 nm.

There are 9 relative strong emission lines in the wavelength range of 620 nm to 650 nm of a hydrogen-diffusion flame with 6.5 l/min co-flow. These 9 emission lines are at 620.41 nm, 622.30 nm, 624.76 nm, 626.48 nm, 630.78 nm, 631.93 nm, 632.46 nm, 637.80 nm and 644.40 nm.

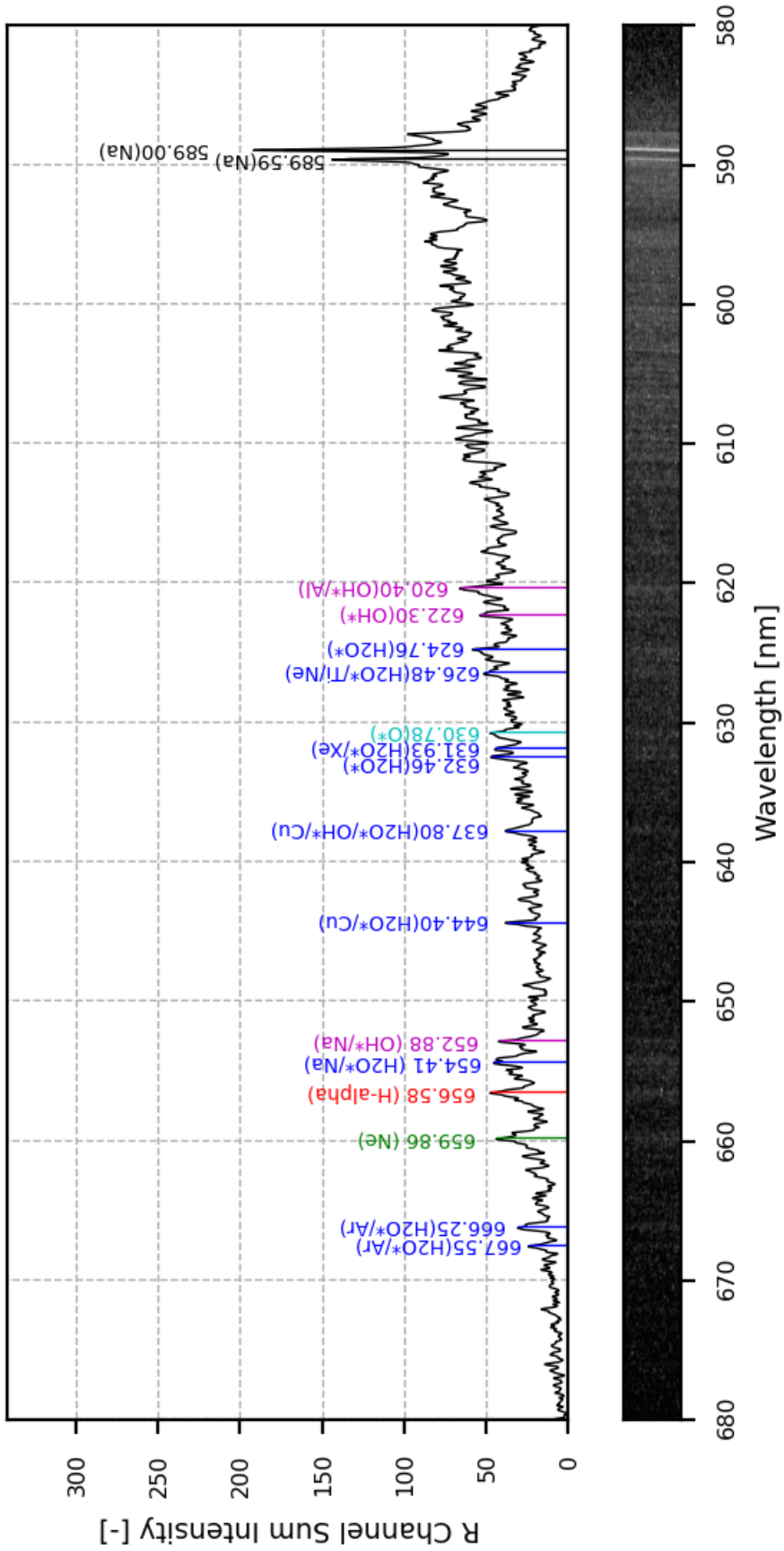

Fig. 101: Hydrogen-air diffusion flame with 6.5 l/min air co-flow spectrum plot in the wavelength of 620 nm to 700 nm.

Among these emission lines, there are three lines different from those of the hydrogen diffusion flame, and their wavelengths are 631.93 nm, 637.80 nm and 644.40 nm. These lines are very weak or absent in the hydrogen diffusion flame. By comparing to the HITRAN database and NIST database, the species and elements with emission lines close to the experimental lines are listed below.

Experimental emission line wavelength (nm)	**Species**	**Wavelength in Vacuum (nm)**	**Wavelength in Air (nm)**	**Intensity $(cm^{-1}/(molecule \cdot cm^{-2}))$**
631.93	$\boldsymbol{H_2O}$	**631.90**	**631.72**	$\mathbf{3.36 \times 10^{-25}}$
	$\boldsymbol{H_2O}$	**631.92**	**631.75**	$\mathbf{1.50 \times 10^{-25}}$
	O_2	632.06	631.89	5.16×10^{-27}
	OH	632.02	631.84	1.90×10^{-27}
	OH	632.04	631.87	1.84×10^{-27}
	OH	632.33	632.16	5.75×10^{-26}
	OH	632.35	632.18	5.73×10^{-26}
637.80	H_2O	637.97	637.80	4.99×10^{-27}
	H_2O	637.98	637.81	1.38×10^{-27}
	$\boldsymbol{H_2O}$	**637.99**	**637.82**	$\mathbf{9.87 \times 10^{-27}}$
	H_2O	638.00	637.83	3.99×10^{-27}
	OH	638.06	637.88	1.29×10^{-28}
	OH	638.08	637.91	1.25×10^{-28}
644.40	$\boldsymbol{H_2O}$	**644.54**	**644.36**	$\mathbf{1.37 \times 10^{-25}}$
	H_2O	644.57	644.40	5.72×10^{-27}
	H_2O	644.61	644.44	1.29×10^{-25}

Table. 29: List of species with their emission lines close to the extra experimental emission lines in the range of 620 nm to 650 nm.

Experimental emission line wavelength (nm)	Elements	Wavelength in Air (nm)
631.93	Xe	631.81
	Pt	631.84
637.80	Xe	637.53
	Cm	637.67
	Cu	**637.78**
	Pa	637.93
644.40	Se	644.43
	Ra	644.62
	Cu	**644.86**

Table. 30: List of elements with their emission lines close to the additional emission lines of hydrogen-air diffusion flame with 6.5 l/min air co-flow in the range of 620 nm to 650 nm.

Same as the previous analysis, all species and elements that may cause the emission in this wavelength range are listed in Table. 31.

Experimental emission line wavelength (nm)	Elements/Species	Wavelength in Air (nm)
631.93	H_2O	631.72
	H_2O	631.75
637.80	Cu	637.78
	H_2O	637.82
644.40	H_2O	644.36
	Cu	644.86

Table. 31: List of elements and species with their emission lines close to the extra experimental emission lines in the range of 620 nm to 650 nm.

Some species in Table. 30 are not listed in Table. 31, they have emission lines close to the experimental results, but their intensities are much lower than those of the selected species. Hence, their contributions to the hydrogen-air diffusion flame spectrum are not considered.

6.3.3 Emission lines in the range of 660 nm to 700 nm

The emission lines of hydrogen-air diffusion flame with 6.5 l/min air co-flow in the wavelength range of 660 nm to 700 nm are the same as the hydrogen-air diffusion flame. The two emission lines are 666.25 nm and 667.55 nm. As discussed in the previous chapter, these two emission lines are both contributed by H_2O and Ar.

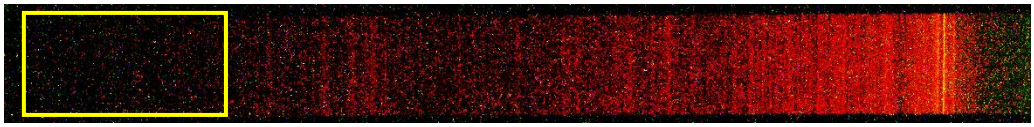

Fig. 102: Spectrum of the hydrogen-air diffusion flame with 6.5 l/min air co-flow in the wavelength of 660 nm to 700 nm (Yellow Boxed).

Compared to the emission lines in other wavelength ranges, the lines in the range of 660 nm to 700 nm are relatively weak.

6.3.4 Conclusion

To sum up, the addition of 6.5 l/min air co-flow has a limited influence on the hydrogen-air diffusion flame spectrum. In the range of 590 nm to 620 nm, there are 13 emission lines, of which 10 of them are considered the same as hydrogen diffusion flame. In the wavelength band of 620 nm to 650 nm, 9 emission lines exist, in which 6 lines are the same as hydrogen diffusion flame. In the range of 660 nm to 700 nm, the

two emission lines are determined to be the same as the diffusion flame without co-flow.

6.4 Spectrum of hydrogen-air diffusion flame with air co-flow at 13 l/min

In this sub-section, the spectrum of hydrogen-air diffusion flame with 13 l/min air co-flow will be shown and analysed. The spectra of hydrogen-air diffusion flame with air co-flows will be compared.

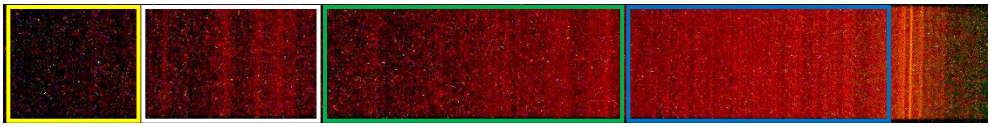

Fig. 103: Spectrum of the hydrogen-air diffusion flame with 13 l/min air co-flow in the wavelength of 660 nm to 700 nm.

6.4.1 Emission lines in the range of 590 nm to 620 nm

There are 15 emission lines in this wavelength range, of which 12 lines are the same as the emission lines of the hydrogen-air diffusion flame with 6.5 l/min air co-flow. The same lines are at 591.27 nm, 595.79 nm, 597.69 nm, 600.83 nm, 603.26 nm, 604.64 nm, 609.49 nm, 610.99 nm, 612.18 nm and 617.71 nm. Besides, there are 3 emission lines in addition to the 6.5 l/min air co-flow hydrogen flame. These lines are at 596.80 nm, 613.94 nm and 615.80 nm.

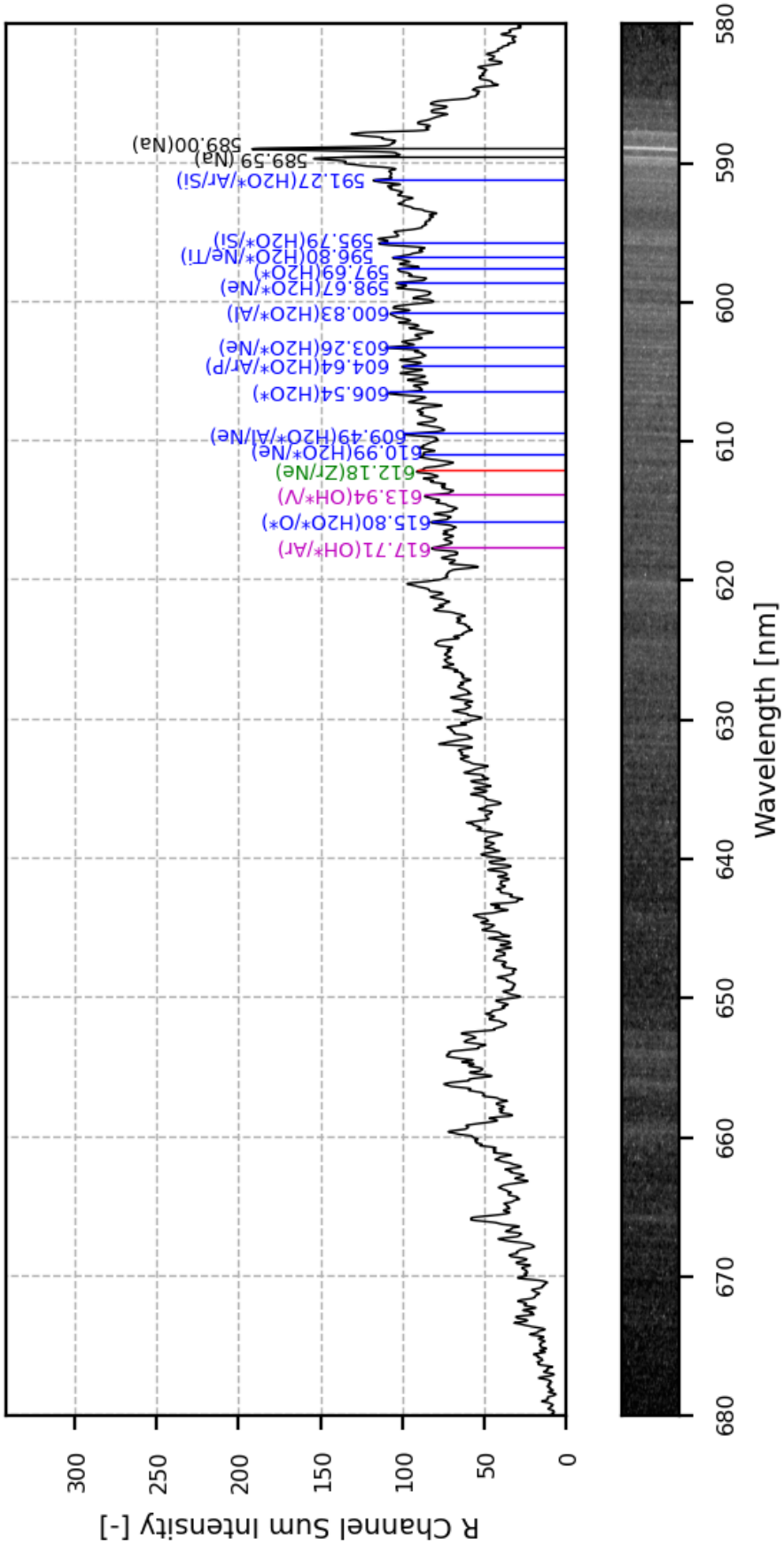

Fig. 104: Hydrogen-air diffusion flame with 13 l/min air co-flow spectrum plot in the wavelength of 590 nm to 620 nm

Experimental emission line wavelength (nm)	Spcies	Wavelength in Vacuum (nm)	Wavelength in Air (nm)	Intensity $(cm^{-1}/(molecule \cdot cm^{-2}))$
596.80	$\boldsymbol{H_2O}$	**596.95**	**596.79**	$\mathbf{1.27 \times 10^{-24}}$
	H_2O	596.96	596.80	1.32×10^{-26}
	H_2O	596.97	596.81	1.47×10^{-25}
613.94	$\boldsymbol{OH}$	**614.11**	**613.95**	$\mathbf{3.34 \times 10^{-24}}$
615.80	H_2O	616.01	615.84	1.95×10^{-28}
	$\boldsymbol{H_2O}$	**615.93**	**615.77**	$\mathbf{2.58 \times 10^{-28}}$
	H_2O	615.96	615.79	5.70×10^{-29}
	H_2O	615.97	615.80	1.32×10^{-29}
	H_2O	615.99	615.83	1.46×10^{-29}

Table. 32: List of species with their emission lines close to the additional emission lines of hydrogen-air diffusion flame with 13 l/min air co-flow in the range of 590 nm to 620 nm.

The species and elements which have the most outstanding contribution to the emission lines in the hydrogen-air diffusion flame with 13 l/min air co-flow are highlighted in bold in Table. 32 and Table. 33.

Experimental emission line wavelength (nm)	Elements	Wavelength in Air (nm)
596.80	**Ne**	**596.55**
	Ti	**596.58**
	Eu	596.61
	Eu	596.71
613.94	In	613.21
	V	**613.54**
	Ba	614.17
615.80	**O**	**615.60**

	O	**615.68**
	O	**615.82**

Table. 33: List of elements with their emission lines close to the additional emission lines of hydrogen-air diffusion flame with 13 l/min air co-flow in the range of 590 nm to 620 nm.

From the above two tables, it could be found that the oxygen atom in the HITRAN database has no noticeable emission lines, but there are intense lines in the NIST database. It might be due to the differences in how they collect the data. The HITRAN database is a mixture of experimental and calculated results, while the NIST database mainly focuses on the theoretical calculation and observation from the solar corona.

Experimental emission line wavelength (nm)	**Species/Elements**	**Wavelength in Air (nm)**
596.80	Ne	596.55
	Ti	596.58
	H_2O	596.79
613.94	V	613.54
	OH	613.95
615.80	O	615.60
	O	615.68
	H_2O	615.77
	O	615.82

Table. 34: List of elements and species with their emission lines close to the additional experimental emission lines of hydrogen-air diffusion flame with 13 l/min air co-flow in the range of 590 nm to 620 nm.

To summarise, the above table lists the species and elements that may have an influence and their corresponding wavelengths on the spectrum.

6.4.2 Emission lines in the range of 620 nm to 650 nm

There are 6 emission lines in the wavelength range of 620 nm and 650 nm. Their wavelength is 620.25 nm, 624.54 nm, 630.59 nm, 631.71 nm, 637.42 nm and 644.11 nm. These 6 emission lines are all consistent with the emission lines of the hydrogen flame with 6.5 l/min air co-flow. However, there are 3 emission lines of the 6.5 l/min air co-flow flame that become inconspicuous or disappear in the 13 l/min air co-flow flame in this range. They are emission lines at 622.30 nm, 626.482 nm and 632.80 nm.

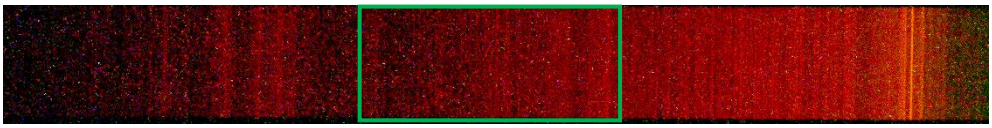

Fig. 105: Spectrum of the hydrogen-air diffusion flame with 13 l/min air co-flow in the wavelength of 620 nm to 650 nm (Green boxed).

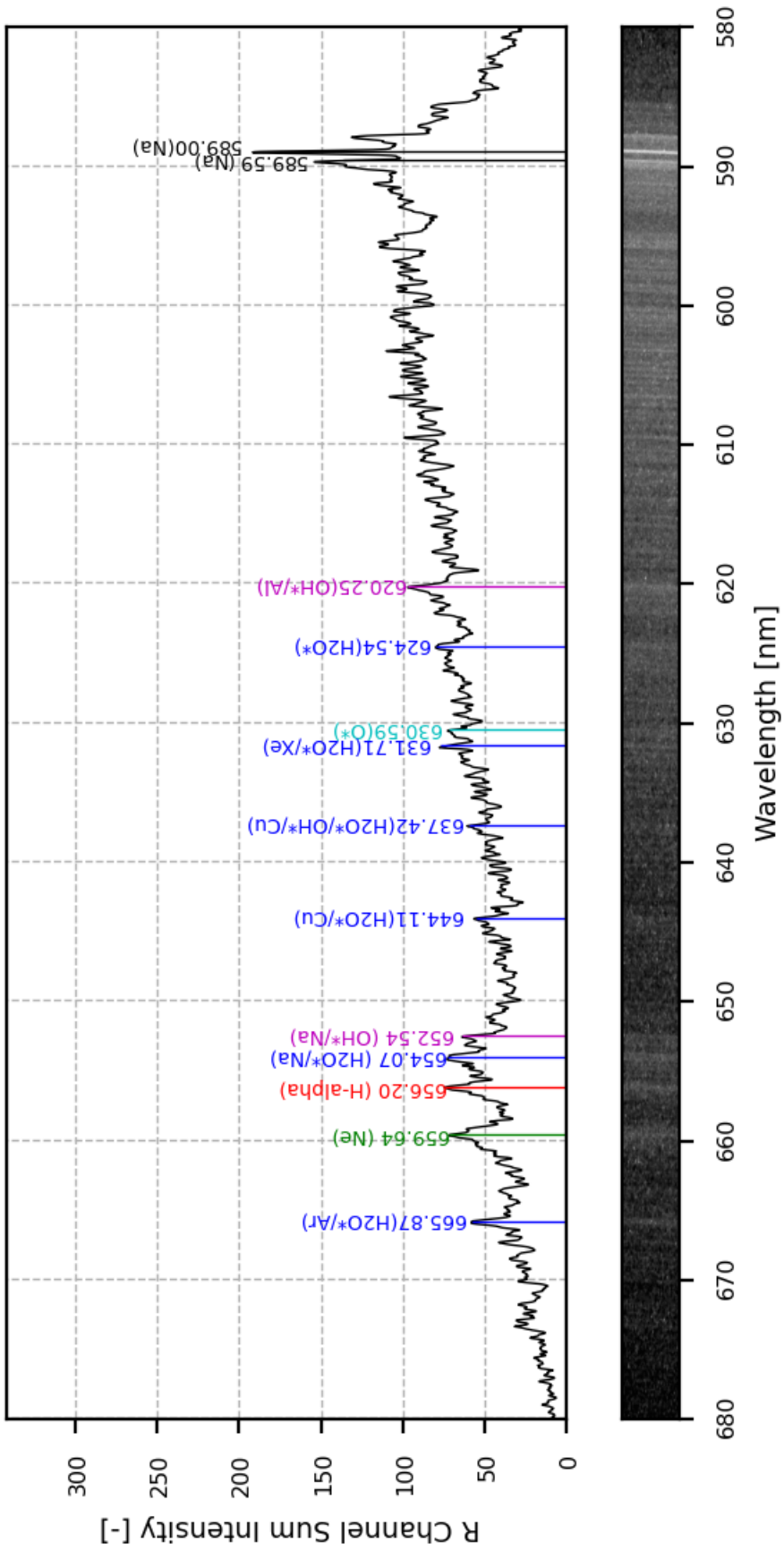

Fig. 106: Hydrogen-air diffusion flame with 13 l/min air co-flow spectrum plot in the wavelength of 620 nm to 700 nm.

As analysed in 6.3.2, the additional emission lines of the 6.5 l/min air co-flow hydrogen flame at 622.30 nm might be due to OH. The line at at 626.48 nm might be the emission line of H_2O, Ti and Ne. The line at 632.46 nm might caused by H_2O.

6.4.3 Emission lines in the range of 660 nm to 700 nm

The emission lines in the wavelength range of 660 nm to 700 nm can barely be seen in the spectrum. However, from the spectrum plot, the emission lines are clearly shown.

Fig. 107: Spectrum of the hydrogen-air diffusion flame with 13 l/min air co-flow in the wavelength of 660 nm to 700 nm (Yellow boxed).

Unlike the spectrum of the hydrogen-air diffusion flame with 6.5 l/min air co-flow, there is only one distinct emission line in this wavelength range. Its wavelength is 665.84, which is considered the same emission line as the 666.25 nm line of the 6.5 l/min air co-flow flame. Besides the emission line at 666.25 nm, 6.5 l/min air co-flow hydrogen flame has another line at 667.48 nm, which is considered to belong to H_2O and Ar.

6.4.4 Conclusion

In conclusion, there are 15 noticeable emission lines in the wavelength range of 590 nm to 620 nm, 11 lines in the range of 620 nm to 650 nm, and 1 line between 660 nm and 700 nm. The additional emission lines compared to the hydrogen-air

diffusion flame with 6.5 l/min air co-flow, the additional emission lines in this wavelength band are mainly due to the increase in air co-flow flow rate. They result in more hydrogen mixing with air and combusted more sufficiently. More sufficient combustion results in a higher flame temperature; hence the elements in the nozzle, burner and atmosphere are easier to be excited by the high temperature.

6.5 Spectrum of hydrogen-air diffusion flame with oxygen co-flow at 0.30 l/min and 0.55 l/min

In order to analyse the hydrogen-air diffusion flame spectrum better, in addition to the air co-flow, oxygen was also added as co-flow for comparison. In this sub-section, the spectra of hydrogen-air diffusion flame with 0.30 l/min and 0.55 l/min oxygen co-flow will be discussed.

(a)

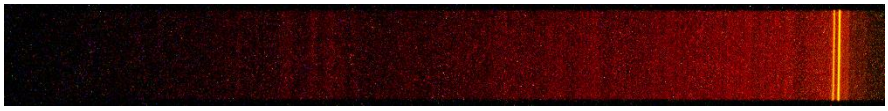

(b)

Fig. 108: Spectrum of the hydrogen-air diffusion flame with (a) 0.30 l/min oxygen co-flow; (b) 0.55 l/min in the wavelength of 590 nm to 700 nm.

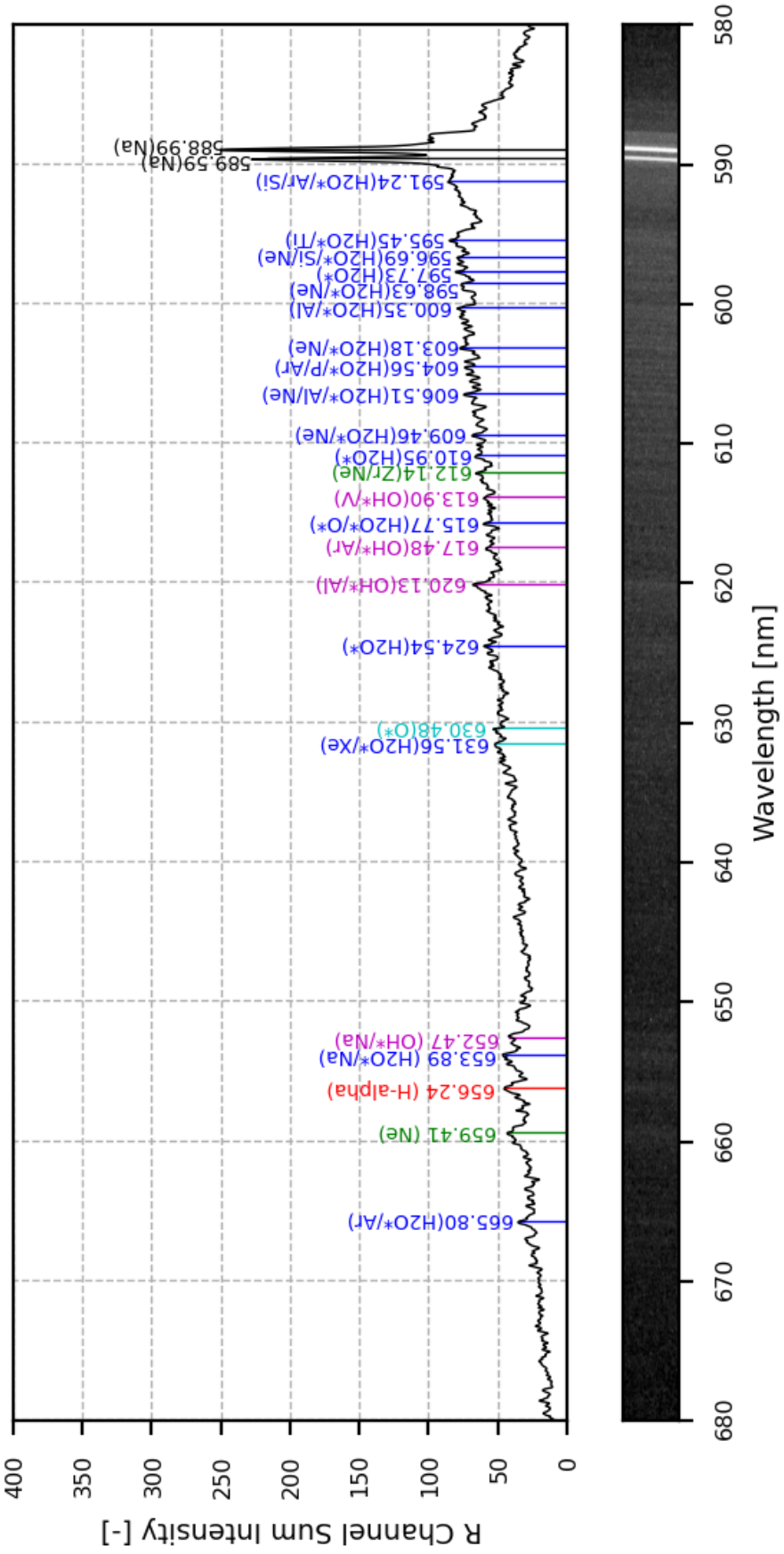

Fig. 109: Hydrogen-air diffusion flame with 0.30 l/min oxygen co-flow spectrum plot in the wavelength of 590 nm to 700 nm.

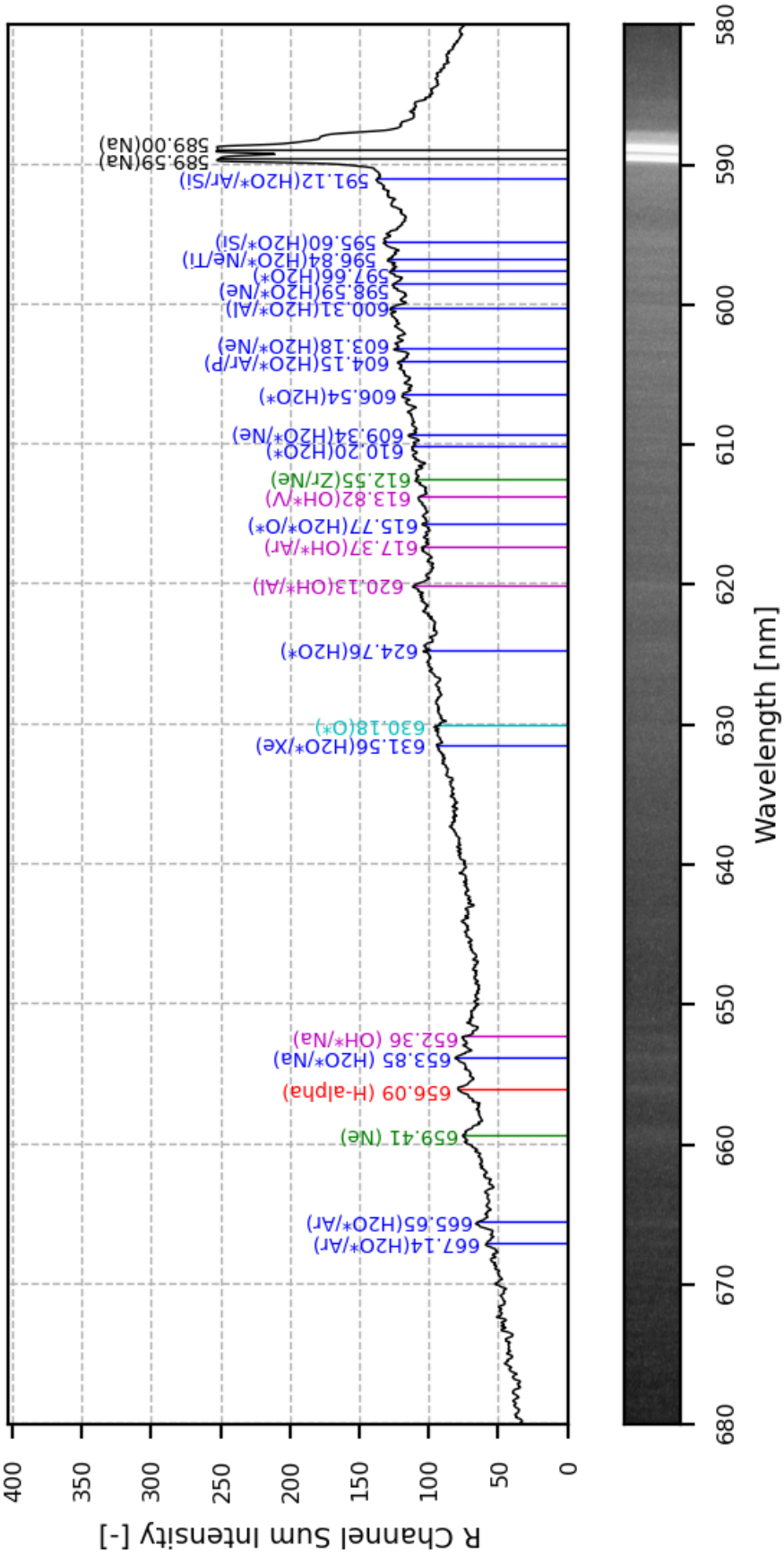

Fig. 110: Hydrogen-air diffusion flame with 0.55 l/min oxygen co-flow spectrum plot in the wavelength of 590 nm to 700 nm.

It can be found from Fig. 108 that the two spectra are similar. The intensity of the (b) spectrum is generally higher than the (a) spectrum. However, the relative intensities of the emission lines in (b) are lower, which means the contrast of the spectrum is lower than (a).

The emission lines both in the hydrogen-air diffusion flame with oxygen co-flows are the same. They are also the same as the emission lines of the 13 l/min air co-flowed hydrogen diffusion flame. Except for two emission lines, which intensities are too low or disappear at the wavelength of 637.42 nm and 644.11 nm. The table below lists all the emission lines and their possible contributed species and elements.

Experimental emission line wavelength (nm) of 0.30 l/min oxygen co-flow	**Experimental emission line wavelength (nm) of 0.55 l/min oxygen co-flow**	**Species/Elements**
591.14	591.12	H_2O
		Ar
		Si
595.45	595.60	H_2O
		Ti
596.70	596.84	H_2O
		Ne
		Ti
597.73	597.66	H_2O
598.63	598.59	H_2O
		Ne
600.35	600.31	H_2O
		Al
603.18	603.18	H_2O
		Ne
604.56	604.15	H_2O

		P
		Ar
606.51	606.54	H_2O
609.46	609.34	H_2O
		Ne
610.95	610.20	H_2O
		Ne
612.14	612.55	Zr
		Ne
613.90	613.82	OH
		V
615.77	615.77	H_2O
		O
617.48	617.37	OH
		Ar
620.13	620.13	OH
		Al
624.54	624.76	H_2O
630.48	630.18	H_2O
631.56	631.56	H_2O
665.80	665.65	H_2O
		Ar

Table. 35: The emission lines and possible species and elements of hydrogen-air diffusion flame with 0.30 and 0.55 l/min oxygen co-flow in the range of 590 nm to 650 nm and 660 nm to 700 nm.

In addition to the above emission lines, the 0.55 l/min oxygen co-flow hydrogen flame has a line at 667.14 nm, which is considered as the emission line of H_2O and Ar.

6.6 Emission lines of 650 nm to 660 nm of hydrogen-air diffusion flame with co-flow

The emission lines in the wavelength range of 650 nm to 660 nm with co-flows are the same, and they are listed in the table below.

6.5 l/min air co-flow	**13 l/min air co-flow**	**0.30 l/min oxygen co-flow**	**0.55 l/min oxygen co-flow**	**Species/Elements**
652.88	652.54	652.47	652.36	OH
				Na
654.41	654.07	653.89	653.85	H_2O
				Na
656.58	656.20	656.24	656.09	$H-\alpha$
659.86	659.64	659.41	659.41	Ne

Table. 36: List of emission lines of the co-flowed hydrogen-air diffusion flame in the range of 650 nm to 660 nm.

Although there are slight differences in the values, they can still be considered the same emission lines. Also, they are determined to be the same as the lines in the hydrogen diffusion flame without co-flow. Therefore, it can be known that these emission lines are consistent under different combustion conditions. Especially the wavelength at 656 nm, which is very close to the emission line of $H-\alpha$. The presence of this emission line in all the hydrogen diffusion flames means that the existence of $H-\alpha$ is highly likely. Besides, the emission lines at 652 nm are considered the contribution of OH and Na. The lines at 654 nm might be caused by H_2O and Na, and

the lines at 659 nm could be the emission lines of Ne.

6.7 List of emission lines of hydrogen diffusion flame under different co-flow conditions in the range of 590 nm to 700 nm

In order to summarise and compare the emission lines in the wavelength range of 590 nm to 700 nm of hydrogen-air diffusion flame under different co-flow conditions, the following table (Table. 37) lists all the emission lines and the elements or species that may cause these lines.

Co-flow conditions					**Species/ Elements**
No co-flow	**6.5 l/min air**	**13 l/min air**	**0.30 l/min oxygen**	**0.55 l/min oxygen**	
/	591.27	591.27	591.24	591.12	H_2O/Ar/Si
595.04	/	/	/	/	H_2O/Ti
595.60	595.49	595.79	595.45	595.60	H_2O/Si
/	/	596.80	596.69	596.84	H_2O/Ne/Ti
597.25	597.28	/	/	/	H_2O
597.77	/	597.69	597.73	597.84	H_2O/Ti/Si
/	598.67	598.67	598.63	598.59	H_2O/Ne
599.04	/	/	/	/	H_2O/Kr
600.53	600.42	600.83	600.35	600.31	H_2O/Al
603.00	603.33	603.26	603.18	603.18	H_2O/Ne
604.30	604.71	604.64	604.56	604.15	H_2O/P/Ar
606.69	606.66	606.54	606.51	606.54	H_2O

607.29	/	/	/	/	H_2O/Al/Ne
/	608.82	/	/	/	H_2O/Xe/P
609.61	609.64	609.49	609.46	609.34	H_2O/Ne
610.65	611.06	610.99	610.95	610.20	H_2O
612.85	612.82	612.18	612.14	612.55	Zr/Ne
/	/	613.94	613.90	613.82	OH/V
/	/	615.80	615.77	615.77	H_2O/O
/	617.71	617.71	617.48	617.37	OH/Ar
620.43	620.40	620.25	620.13	620.13	OH/Al
622.19	622.30	/	/	/	OH
624.84	624.76	624.54	624.54	624.76	H_2O
626.45	626.48	/	/	/	H_2O/Ti/Ne
630.81	630.78	630.59	630.48	630.18	H_2O
632.01	631.93	631.71	631.56	631.56	H_2O/Xe
632.42	632.46	/	/	/	H_2O
/	637.80	637.42	/	/	H_2O/OH/Cu
/	644.40	644.11	/	/	H_2O/Cu
652.88	652.88	652.54	652.47	652.36	OH/Na
654.34	654.41	654.07	653.89	653.85	H_2O/Na
656.58	656.58	656.20	656.24	656.09	$H-\alpha$
659.90	659.86	659.64	659.41	659.41	Ne
666.25	666.25	665.84	665.80	665.65	H_2O/Ar
667.48	667.55	/	/	667.14	H_2O/Ar

Table. 37: List of emission lines hydrogen diffusion flame under different co-flow conditions in the range of 590 nm to 700 nm.

6.8 Integration of H_2O, OH, O and $H-\alpha$ peaks

In this section, the integration of H_2O, OH, O, and $H-\alpha$ emission lines in the experiments are listed below in Table. 38 and Table. 39.

$6.5\ l/min$ air co-flow		$13\ l/min$ air co-flow		$0.30\ l/min\ O_2$ co-flow		$0.55\ l/min\ O_2$ co-flow	
Wavelength (nm)	**Value of integrati-on**	**Wavelength (nm)**	**Value of integration**	**Wavelength (nm)**	**Value of integration**	**Wavelength (nm)**	**Value of integration**
591.27	27.9379	**591.27**	38.1536	**591.24**	49.7679	**591.12**	66.2487
595.49	31.3021	**595.79**	31.8876	**595.45**	27.623	**595.6**	101.0113
/	/	**596.8**	45.3571	**596.69**	40.2728	**596.84**	118.0389
597.28	21.9961	**/**	/	**/**	/	**/**	/
/	/	**597.69**	30.3054	**597.73**	37.1036	**597.66**	97.9290
598.67	21.8492	**598.67**	30.0960	**598.63**	50.1833	**/**	/
600.42	29.5043	**600.83**	54.5821	**600.35**	44.5390	**600.31**	88.9384
603.33	23.5596	**603.26**	34.2932	**603.18**	35.8125	**603.18**	58.0718
604.71	31.9201	**604.64**	36.1269	**604.59**	36.5845	**604.15**	62.8790
606.66	22.0579	**606.54**	30.8065	**606.51**	36.4775	**606.54**	57.1851
608.82	22.7576	**/**	/	**/**	/	**/**	/
609.64	30.4497	**609.49**	36.9921	**609.46**	47.3273	**609.34**	54.1714
611.06	30.8959	**610.99**	53.6356	**610.95**	54.4723	**610.20**	62.0509
/	/	**615.80**	39.7688	**615.77**	40.8615	**615.77**	53.0866
624.76	16.3185	**624.54**	34.9747	**624.54**	37.6925	**624.76**	87.2786
626.48	16.3597	**/**	/	**/**	/	**/**	/
631.93	13.8440	**631.71**	26.6770	**631.56**	30.0762	**631.56**	41.8133
632.46	13.3752	**/**	/	**/**	/	**/**	/
637.80	19.7610	**637.42**	19.3927	**/**	/	**/**	/
644.40	9.9644	**644.11**	16.2351	**/**	/	**/**	/
654.41	25.4604	**654.07**	39.7051	**653.89**	39.4440	**653.85**	63.6677
666.25	13.3867	**665.87**	40.4248	**665.80**	41.4796	**665.65**	48.8035
667.55	11.3922	**/**	/	**/**	/	**667.14**	51.9692

Table. 38: Integration of experimental H_2O emission lines in hydrogen-air diffusion flame under different co-flow conditions.

$6.5\ l/min$ air co-flow		$13\ l/min$ air co-flow	
Wavelength (nm)	**Value of integration**	**Wavelength (nm)**	**Value of integration**
/	/	**613.94**	91.8732
617.71	31.8586	**617.71**	50.4527
620.40	52.8865	**620.25**	92.9317
622.30	27.9592	**/**	/
652.88	26.1855	**652.54**	39.2489
$0.30\ l/min\ O_2$ co-flow		$0.55\ l/min\ O_2$ co-flow	
Wavelength (nm)	**Value of integration**	**Wavelength (nm)**	**Value of integration**
613.90	32.6188	**613.82**	117.4483
617.48	43.2172	**617.37**	84.2187
620.13	83.3252	**620.13**	88.7247
/	/	**/**	/
652.47	32.6406	**652.36**	104.986

Table. 39: Integration of experimental OH emission lines in the hydrogen-air diffusion flame under different co-flow conditions.

In Table. 38, the integration of the red channel value correspond to each emission lines that is attributed to H_2O. By summing the integrals of all emission lines, the intensity of the emission lines attributed to H_2O in the spectral range of 590 nm to 700 nm can be obtained. The sum for the hydrogen-air diffusion flame with $6.5\ l/min$ air co-flow is 434.09, for the flame with $13\ l/min$ air co-flow is 639.41, for the flame with $0.30\ l/min\ O_2$ co-flow is 649.72, and for the flame with $0.55\ l/min\ O_2$ co-flow is 1113.14. Due to the relatively lower intensities of some emission lines, they were not included in the table To exclude the influence of these emission lines, the sum of selected emission lines for each of the four co-flow cases was also calculated (emission lines not selected in the diffusion flame without co-flow were excluded as well)., resulting in 268.70 for the flame with $6.5\ l/min$ air co-flow, 420.11 for the flame with $13\ l/min$ air co-flow, 431.53 for the flame with $0.30\ l/min\ O_2$ co-flow, and 725.87

for the flame with 0.55 l/min O_2 co-flow. The integration of the H_2O emission lines in the non-co-flowed hydrogen-air diffusion flame was calculated as 331.64 in the previous chapter. If only calculate the total sum of integrals for the emission lines that exist simultaneously in the presence of co-flow, it is 195.71.

The same calculation method was also being used to calculate the integral for OH emission lines. Without excluding the co-existing emission lines, the sum for the hydrogen-air diffusion flame with 6.5 l/min air co-flow is 138.89, for the flame with 13 l/min air co-flow is 274.51, for the flame with 0.30 l/min O_2 co-flow is 191.80, and for the flame with 0.55 l/min O_2 co-flow is 395.38. When only considering the simultaneously present emission lines in all four co-flow conditions, the sum for the hydrogen-air diffusion flame with 6.5 l/min air co-flow is 79.07, for the flame with 13 l/min air co-flow is 132.18, for the flame with 0.30 l/min O_2 co-flow is 115.97, and for the flame with 0.55 l/min O_2 co-flow is 193.71. The integration of the OH emission lines in the non-co-flowed hydrogen-air diffusion flame was calculated as 72.32 and the total sum of integrals for the emission lines that exist simultaneously in the presence of co-flow, it is 46.92.

Co-flow condition	O		$H-\alpha$	
	Emission line (nm)	Integration	Emission line (nm)	Integration
Non co-flow	630.81	15.7617	656.58	44.6635
6.5 l/min air	630.78	37.8033	656.58	53.9120
13 l/min air	630.59	80.6062	656.20	91.2643
0.30 l/min O_2	630.48	68.3088	656.24	69.9860
0.55 l/min O_2	630.18	138.6994	656.09	126.7201

Table. 40: Integration of experimental O and $H-\alpha$ emission lines in the hydrogen-air diffusion flame under different co-flow conditions.

Table. 40 is the Integration of experimental O and $H-\alpha$ emission lines in the hydrogen-air diffusion flame under different co-flow conditions.

Besides, the FWHM of the $H-\alpha$ emission line in the five co-flow conditions are 0.93 nm for the non-co-flow flame, 0.99 nm for the flame with $6.5\ l/min$ air co-flow, 1.03 nm for the flame with $13\ l/min$ air co-flow, 0.94 nm for the flame with $0.30\ l/min$ O_2 co-flow, and 1.00 nm for the flame with $0.55\ l/min\ O_2$ co-flow.

From the Chemkin models it could be known that the H radical concentration are higher as the co-flow speed increases, thus it can be concluded that the linewidth of $H-\alpha$ emission line is positively correlated with the H radical concentration. Besides, in the case of flame with oxygen co-flow, the flame temperature is higher compared to the air co-flow conditions, and the linewidth and intensity of the $H-\alpha$ emission line are also the highest.

6.9 Conclusion

In this chapter, the air or oxygen co-flows were applied to the hydrogen-air diffusion flame, and the methodology was identical to the hydrogen diffusion flame spectrum experiment. The gas flow rate in the experiment is also mentioned in detail, including the flow rate of fuel gas and the co-flow and the conversion of oxygen and air.

In addition, from the Chemkin model of hydrogen diffusion flames, it is understood that there are H, O and OH radicals present in the reaction zone of the flame. However, the simulated flame temperature and the mole fraction of radicals

cannot directly represent the intensity of their excitation within the flame. Therefore, the model can only serve as a reference.

In general, the spectra of hydrogen-air diffusion flames with co-flows are similar to the hydrogen flame spectrum without co-flow. The sodium double lines at 588.59 nm and 590.00 nm are present in all co-flow conditions. By comparing with data in HITRAN and NIST database, in the red-light band, most of the emission peaks are caused by the final product H_2O , intermediate product OH and other pollutants from the equipment and atmosphere. However, there are some emission lines that only become apparent or appear under certain co-flow conditions.

In the wavelength range of 590 nm to 620 nm, there are 8 emission lines that appear in all the flames. They are at around 595.5 nm, 600.4 nm, 603.2 nm, 604.5 nm, 606.5 nm, 609.5 nm, 610.8 nm and 612.5 nm. These emission lines are contributed mainly by H_2O. There are also some lines that only appear in certain co-flow conditions. Such as, the line at 591.2 nm, 598.6 nm, and 617.5 nm exists in both the air and oxygen co-flow flames but not in the no co-flow flame. On the other hand, there are some emission lines that only appear in the hydrogen diffusion flame and not in flames with co-flows. They are 595.6 nm, 599.0 nm and 607.3 nm. Besides, the emission line at 608.8 nm only exists in the hydrogen flame with 6.5 l/min air co-flow. Also, the lines at approximately 596.8 nm, 613.9 nm, and 615.7 nm only appear in the spectra of hydrogen flames with oxygen co-flow and 13 l/min air co-flow.

In the wavelength of 620 nm to 650 nm, there are 4 emission lines present in all the hydrogen flame spectra. They are at about 620.3 nm, 624.6 nm, 630.5 nm and 631.6 nm. In addition, there are 3 emission lines that only appear in the hydrogen

diffusion flame and flames with air co-flow. Their wavelengths are 622.2 nm, 626.4 nm and 632.4 nm. Furthermore, two emission lines exist in the air co-flow flames only, which are at around 637.5 nm and 644.6 nm.

In the 660 nm to 700 nm band, the number and intensity of emission lines are lower than those of the other bands discussed earlier. The line at approximately 666.2 nm appears in all the five testing flames, and the line at 667.5 nm only exists in the flame without co-flow and the flame with $6.5\ l/min$ air co-flow.

The most interesting wavelength range is between 650 nm and 660 nm, which is the range that might have $H-\alpha$. All The flames have the same emission lines in this range. They are at about 652.6 nm, 654.0 nm, 656.4 nm and 659.7 nm. The 652.6 nm emission line might be due to OH and Na. The one at 654.0 nm might be because of H_2O and Na, and the line at 659.7 nm would be due to Ne. It is worth noting that the line at 656.4 nm matches the emission line of $H-\alpha$. This emission line is present in all the hydrogen-air diffusion flames. Therefore, it is highly possible that $H-\alpha$ contributed to the reddish flame colour of hydrogen diffusion flame.

To sum up, the emission lines of the hydrogen-air diffusion flames with co-flow are slightly different from those without co-flow. The emission lines newly appear or become obvious in the flame with air co-flow are mainly contributed by H_2O. Upon comparison of the integration sum of all the flames, it could be seen that in the flame with $0.55\ l/min\ O_2$ co-flow, the intensity of the H_2O emission is the highest, followed by the flame with $0.30\ l/min\ O_2$ co-flow, $13\ l/min$ air co-flow, $6.5\ l/min$ air co-flow, and finally, the non-co-flowed hydrogen-air diffusion flame with the lowest intensity.

The addition of air co-flow leads to a better hydrogen and air mixing, which leads

to a higher local flame temperature. Moreover, an increase in the flow rate of the air co-flow also increases the possibility of collisions of the atoms. Hence, it is more likely for these atoms to be excited due to the effect of collision at a higher flow rate. Therefore, in the case of $13\ l/min$ air co-flow, the emission line intensities of OH, O, and $H-\alpha$ are higher than the $0.30\ l/min\ O_2$ co-flow flame. Furthermore, the newly appeared emission lines in the flames with oxygen co-flow are mainly due to the OH. The temperature of oxygen co-flowed flame would be higher than the flame with air co-flow. Hence the intensities of OH emission lines might become more apparent in the spectra due to the higher local flame temperature, and more elements in the equipment materials or the atmosphere will be excited, resulting in the appearance of emission lines.

Chapter 7: Conclusion and recommendations for future work

7.1 Conclusion

In this thesis, the research on visualization of the hydrogen-air diffusion flame colour was realized by the schlieren imaging technique, high-speed imaging technique, and direct imaging technique. The spectra of hydrogen diffusion flames under different conditions were analysed using the spectrograph. The key findings of the research are listed below.

7.1.1 Hydrogen flame ignition process visualisation

- The schlieren images of the hydrogen bubble ignition process show that the hydrogen bubble blasted at the first spark, and the hydrogen was mixed with the surrounding air.
- The mixture of hydrogen and air was ignited at the second spark, and the visible flame only existed for about 56 ms in the soapy bubble case and 11 ms in the distilled water case.

- The heated gas continued to propagate after the visible flame disappeared, and it propagated in all directions firstly and then along the horizontal plane.
- The flame colour of the soapy hydrogen bubble and the distilled water hydrogen bubble differed. The colour of the soapy bubble flame was more yellowish, and the colour of the distilled water flame was more reddish.
- Sodium might be the main contributor to the yellow flame of the soapy hydrogen bubble. However, the reddish colour of the hydrogen flame should not be contributed by sodium.

7.1.2 Hydrogen-air diffusion flames direct imaging visualization

- When the hydrogen rate is fixed, the hydrogen-air diffusion flame length is proportional to the co-flow rate.
- The hydrogen flame with oxygen co-flows is brighter than the flames under other co-flow conditions, and it might be due to the higher flame temperature.
- The $6.5\ l/min$ air co-flowed hydrogen flames have similar colour as the flame without co-flow, while the hydrogen flames with the oxygen co-flows and the $13\ l/min$ air co-flow are more reddish in colour.
- The application of the narrowband $H-\alpha$ filter proves that the hydrogen diffusion flame has emission lines in the range of 652.78 nm to 656.78 nm. Hence the existence of $H-\alpha$ is highly possible.

7.1.3 Hydrogen-air diffusion flame spectrum

- The hydrogen-air diffusion flame has 13 relatively strong emission lines in the wavelength of 590 nm to 620 nm. H_2O contributes to most of the lines.
- H_2O and OH have the most contribution to the 7 emission lines in the range of 620 nm and 650 nm.
- Besides the species involved in the combustion mechanism, elements in the equipment and atmosphere also have the possibility to participate in the flame due to high temperature. The elements from the equipment which might contribute to the spectrum are Ti, Si, Kr, Al Ne, P and Zr. The elements from the atmosphere which might have been excited and emitted light are Ar and Na.
- In the wavelength range of 660 nm to 700 nm, only two emission lines exist. They are both considered to be contributed by H_2O and Ar.
- In the wavelength range of 650 nm to 660 nm, there are 4 emission lines. They are at 652.88 nm, 654.34 nm, 656.58 nm and 659.90 nm. The line at 652.88 nm might be due to OH and Na, and the line at 654.34 nm might be due to H_2O and Na, and the line at 659.90 might be caused by Ne.
- The emission line at 656.58 nm is highly possible to be contributed by $H-\alpha$.

7.1.4 Hydrogen-air diffusion flame with co-flows spectrum

- The spectra of hydrogen diffusion flame with co-flows are similar to the spectrum of the flame without co-flow.

- Some emission lines only exist or become obvious in the co-flowed flames. They are contributed mainly by H_2O, OH, and elements from the surroundings (Xe, Cu, V, Ne, Ti, Ar etc.).
- The involvement of co-flows could make the mixture of hydrogen and oxidant more sufficient, and higher flow rate would increase the possibility of molecular collision. Therefore, more products and intermediate products will be produced, which might lead to the additional H_2O and OH emission lines. Furthermore, the flame temperature of the oxygen co-flowed flame would be higher, which might cause more elements from the atmosphere and equipment to participate in the combustion reaction; hence more emission lines would be generated.

7.2 Recommendations for future work

In addition to the research done in this study, recommended future works are summarised below.

7.2.1 Ignition process of hydrogen contained flames

- The ignition process of hydrogen diffusion flames could be further studied. Different initial energy provided by the electric spark could be applied to the fydrogen gas.
- Various ignition and different hydrogen bubble suspension methods could be tried. For example, the hydrogen bubble could be suspended using ultrasound levitation, silicon carbide wires or other types of bubble stand. The ignition

methods could involve electric sparks, matches, lighters etc.

- The bubble could be filled with a mixture of hydrogen and different oxidizers or inert gases. Their ignition process could be compared with the pure hydrogen bubble flames.
- Apart from bubbles, the hydrogen-containing gas could be confined in different kinds of containers. Their flow and flame behaviour could be studied and compared.

7.2.2 Flame colour of hydrogen contained flames

- To further analyse the hydrogen flame colour in the red colour band, the absolute intensities of all the emission lines could be determined. Especially the intensity of $H-\alpha$ emission line at 656.28 nm.
- Hydrogen-air premixed and hydrogen-oxygen premixed flame with various equivalence ratios could be tested, and their spectra could be analysed.
- The spectra of hydrogen diffusion flame with other co-flows could be studied, such as N_2, CO_2, NH_3, NO etc. The difference in the spectra could be compared.
- The diffusion flame of hydrogen-oxygen or other gases could be experimented with, and their spectra could be analysed.

7.2.3 Applications of $H-\alpha$ in diagnostics

- Research on the correlation between the $H-\alpha$ and the hydrogen flame under different co-flow or equivalence ratio conditions could be done in the future.
- The temperature of the flames could be measured and associated with the

intensity of $H-\alpha$ emission lines.

- The relationship between $H-\alpha$ emission intensity and the hydrogen contained flame combustion efficiency could be studied and applied as a new diagnostic method.

Bibliography

[1] W. F. Barrett, "On Certain Phenomena Associated with a Hydrogen Flame," *Nature,* vol. 5, no. 129, p. 482–484, 1872.

[2] N. P. Brandon and Z. Kurban, "Clean Energy and the Hydrogen Economy," *Philosophical Transactions of the Royal Society A,* vol. 375, p.1-17, 2017.

[3] IEA, "The Future of Hydrogen-Seizing today's opportunities," G20, Japan, 2019. [online]:https://read.oecd-ilibrary.org/energy/the-future-of-hydrogen_1e0514c4-en#page1

[4] J. J. Romm, "The Hype about Hydrogen," *Issues in Science and Technology,* vol. 20, no. 3, 2004.

[5] A. N. Cox, Allen's Astrophysical Quantities, New York: Springer-Verlag, 2000.

[6] HITRAN, "HITRAN Online Database," 2022. [Online]. Available: https://hitran.org/lbl/. [Accessed 3 January 2022].

[7] NIST, "Basic Atomic Spectroscopic Data Finding List," 2022. [Online]. Available: https://physics.nist.gov/PhysRefData/Handbook/Tables/findinglist13.htm. [Accessed 3 January 2022].

[8] IEA, "Global Energy Review 2021," International Energy Agency, 2021.

[9] K. K. Pant and R. B. Gupta, "Fundamentals and Use of Hydrogen as a Fuel," in *Hydrogen Fuel: Production, Transport and Storage,* Boca Raton: CRC Press Taylor & Francis Group, 2009.

[10] W. B. Jensen, "The Origin of the Bunsen Burner'," *Journal of Chemiacl Education,* vol. 82, p. 518, 2005.

[11] T. E. Thrope, "On the Theory of the Bunsen Lamp," *J Chem Soc,* vol. 31, pp. 627-642, 1877.

[12] J. G. Speight, "Chapter 10 - Combustion of Hydrocarbons," in *Handbook of Industrial Hydrocarbon Processes*, Boston, Gulf Professional Publishing, 2011, p. 355–39.

[13] W. Commons, "types.jpg, File:Bunsen burner flame," Wikimedia Commons, the free media repository , 9 July 2021. [Online]. Available: https://commons.wikimedia.org/w/index.php?title=File:Bunsen_burner_flame_types.jpg&oldid=574185694.. [Accessed 18 March 2022].

[14] I. Glassman and R. A. Yetter, "Chapter 6 - Diffusion Flames," in *Combustion*,

4th ed., Burlington, Academic Press, 2008, p. 311–377.

[15] N. Fujisawa, Y. Matsumoto and T. Yamagata, "Influence of Co-flow on Flickering Diffusion Flame," *Flow Turbulence Combust,* vol. 97, pp. 931-950, 2016.

[16] Q. Wang, Y. Zhang and C. Y. Zhao, "Experimental Investigation of Coflow Effect on the Ignition Process of a Methane Jet Diffusion Flame," *Experimental Thermal and Fluid Science,* no. 91, pp. 184-196, 2018.

[17] D. R. Snelling, K. A. Thomson, G. J. Smallwood and O. L. Gulder, "Two-dimensional imaging of soot volume fraction in laminar diffusion flames," *Applied Optics,* vol. 38, no. 12, pp. 2478-2485, 1999.

[18] Y. Xiong, S. H. Chung and M. S. Cha, "A Parametric study of AC electric field-induced toroidal vortex formation in laminar nonpremixed coflow flames," *Combustion and Flame,* vol. 182, pp. 142-149, 2017.

[19] I. Glassman and R. A. Yetter, "Chapter 4 - Flame Phenomena in Premixed Combustible Gases," in *Combustion*, 4th ed., Burlington, Academic Press, 2008, p. 147–260.

[20] K. A. Murty, Introduction to Combustion Phenomena, Boca Raton: CRC Press, 1975.

[21] A. G. Gaydon, The Spectroscopy of Flames, Dordrecht: Springer Netherlands, 1974.

[22] A. P. French and E. F. Taylor, An introduction to quantum physics, 1st ed., New York: Norton, 1978.

[23] H.-W. Huang and Y. Zhang, "Flame colour characterization in the visible and infrared spectrum using a digital camera and image processing," *Meas. Sci. Technol,* vol. 19, p. 085406, 2008.

[24] U. safety, "Uvex safety, UK," [Online]. Available: https://www.uvex-safety.co.uk/en/risks-associated-with-blue-light/. [Accessed 8 April 2020].

[25] Y. Wang, L. Zheng, R. Wolley and Y. Zhang, "Investigation of ignition process from visible to infrared by a high speed colour camera," *Fuel,* vol. 185, p. 500–507, 2016.

[26] AZoSensors, "How UV, IR and Imaging Detectors Work," 21 June 2017. [Online]. Available: https://www.azosensors.com/article.aspx?ArticleID=815. [Accessed 10 April 2020].

[27] M. Momirlan and T. N. Veziroglu, "The Properties of Hydrogen as Fuel Tomorrow in Sustainable Energy System for a Cleaner Planet," *Internaltional J. Hydrog. Energy,* vol. 30, no. 7, p. 795–802, 2004.

[28] X. Liu and Q. Zhang, "Influence of Initial Pressure and Temperature on

Flammability Limits of Hydrogen and Air," *Int. J. Hydrog. Energy,* vol. 39, p.6774-6782, 2014.

[29] D. Rainer, "Hydrogen," *J. Chem. Health Saf.,* vol. 5, 2008.

[30] J. G. Quintiere, Principles of Fire Behavior, New York: Delmar, a division of Thomson Learning, 1998.

[31] J. Olmsted and G. M. Williams, Chemistry: The Molecular Science, Dubuque: Brown Publishers, 1997.

[32] A. A. Konnov, "Remaining uncertainties in the kinetic mechanism of hydrogen combustion," *Combust. Flame,* vol. 152, no. 4, p. 507–528, 2008.

[33] W. K. Kim, T. Mogi and R. Dobashi, "Fundamental study on accidental explosion behavior of hydrogen-air mixtures in an open space," *Internal Journal of Hydrogen Energy,* vol. 38, pp. 8024-8029, 2013.

[34] W. K. Kim, T. Mogi and R. Dobashi, "Effect of propagation behaviour of expanding spherical flames on the blast wave generated during unconfined gas explosions," *Fuel,* vol. 128, pp. 396-403, 2014.

[35] R. W. B. Pearse and A. G. Gaydon, The Identification of Molecular Spectra, London, U.K.: Chapman & Hall Ltd., 1965.

[36] R. W. Schefer, W. D. Kulatilaka, B. D. Patterson, and T. B. Settersten "Visible Emission of Hydrogen Flames," *Combust. Flame,* vol. 156, no. 6, pp. 1234-1241, 2009.

[37] Lab of Atomic & Solid State Physics, "Applications of Quantum Mechanics, Atomic Physics," Erich Mueller Research Site, 10 February 2018. [Online]. Available: https://quantum.lassp.cornell.edu/lecture/atomic_physics. [Accessed 27 May 2022].

[38] A. Z. Capri, Nonrelativistic Quantum Mechanics, Singapore: World Scientific Publishing Co. Pte. Ltd., 2002.

[39] C. Mavroukakis-Karagounis, I. Papadopoulou, M. Papadopoulou and C. Makedonas, "Taking flame tests one step forward: the case of a DIY atomic emission spectrophotometer," *Chemistry Teacher International,* vol. 20180013, 2019.

[40] D. C. Harris and M. D. Bertolucci, Symmetry and spectroscopy: An introduction to vibrational and electronic spectroscopy, New York: Dover Publications, 1978.

[41] B. Kasalica, S. Stojadinović, I. Belča, M. Sarvan, L. Zeković and J. Radic-Peric, "The anomalous sodium doublet D2/D1 spectral line intensity ratio – a manifestation of CCD's presaturation effect," *J Anal Spectrom,* vol. 28, no. 1, p. 92–97, 2013.

[42] "Delta IV Payload Planners Guide," United Launch Alliance, 2007.

[43] J. O'Challaghan, "What is more powerful: A Soyuz rocket or a Delta IV rocket," Spaceanswers, Bath, 2018.

[44] B. Ward, "Bright sodium line meteors," British Astronomical Association, [Online]. Available: https://britastro.org/node/16454. [Accessed 9 April 2020].

[45] T. Kitagawa, "The Formation of the Activeated Water Molecules in High Vibrational States in the Oxy-Hydrogen Flame," *Proceedings of the Imperial Academy,* vol. 12, no. 9, pp. 281-284, 1936.

[46] T. Kitagawa, "Emission Spectrum of the Oxy-Hydrogen Flame and Its Reaction Mechanism," *Rev. Phys. Chem. Jpn.,* vol. 13, no. 2, p. 13, 1939.

[47] A. G. Gaydon, "Flame spectra in the photographic infra-red," *Proceedings of the Royal Society A,* pp. 197-209, 1942.

[48] J. Tennyson and O. L. Polyansky, "Water on the Sun: the Sun yields more secrets to spectroscopy," *Contemporary Physics,* vol. 39, no. 4, pp. 283-294, 1998.

[49] A. G. Gaydon, Spectroscopy and Combustion Theory, 2nd ed., London: Chapman & Hall Ltd., 1948.

[50] L. Zheng, "Combustion Visualization Monitoring Using High Speed Imaging," The University of Sheffield, Sheffield, 2018.

[51] W. C. contributors, "File:Hydrogen transitions.svg," 25 October 2020. [Online]. Available: https://commons.wikimedia.org/w/index.php?title=File:Hydrogen_transitions.svg&oldid=501332484. [Accessed 18 March 2022].

[52] A. K. How, "Hydrogen Alpha Explained," Astronomy Know How, [Online]. Available: http://www.astronomyknowhow.com/hydrogen-alpha.htm. [Accessed 18 March 2022].

[53] I. P. Newton, "A letter of Mr. Isaac Newton, Professor of the Mathematicks in the University of Cambridge; containing his new theory about light and colors," *Philosophical Transactions,* vol. 80, pp. 3075-3087, 1672.

[54] E. D. Malacara and B. J. Thompson, Handbook of optical engineering, New York: Marcel Dekker, 2001.

[55] B. Planelarium, "DADOS Slit-Spectrograph," Baader Planelarium, 2022. [Online]. Available: https://www.baader-planetarium.com/en/baader-dados-slit-%E2%80%93-spectrograph.html. [Accessed 18 May 2022].

[56] N. C. Xuan, "Wavelength opto-electronic," 29 April 2020. [Online]. Available: https://wavelength-oe.com/blog/what-is-a-spectrometer/. [Accessed 18

March 2022].

[57] C. Palmer, Diffraction Grating Handbook, 6th ed., New York: Newport Corporation, 2005.

[58] I. C. London, "The Grating Spectrometer," Imperial College London, London.

[59] L. Hills, "The Camera," Capstone, Oxford, 2004.

[60] W. H. F. Talbot, "Invention of photography – Talbot, 'An oak tree in winter'," [Online]. Available: https://www.bl.uk/collection-items/invention-of-photography. [Accessed 18 March 2022].

[61] R. Stefoff, The Camera, Singapore: Marshall Cavendish, 2007.

[62] K. Keller, "Photography" in Ullmann's Encyclopedia of Industry Chemistry, Weinheim: Wiley-VCH, 2005.

[63] S. Anchell, The Darkroom Cookbook, Oxford: Elsevier, 2008.

[64] M. Caserta, "Density Design Integrated Course Final Synthesis Studio," 2015. [Online]. Available: https://commons.wikimedia.org/w/index.php?curid=37058198. [Accessed 26 May 2022].

[65] MasterClass, "Film vs. Digital Photography: Breaking Down the Pros and Cons," MasterClass, 8 November 2020. [Online]. Available: https://www.masterclass.com/articles/film-vs-digital-photography#what-is-film-photography. [Accessed 26 May 2022].

[66] A. Gold, "The absolute beginner's guide to film photography: Color print film," DPReview, 5 Feburary 2021. [Online]. Available: https://www.dpreview.com/articles/9898575348/the-absolute-beginner-s-guide-to-film-photography-color-print-film. [Accessed 26 May 2022].

[67] G. E. Smith, "The Invention and Early History of the CCD," Nobel Lecture, 2009.

[68] S. learning, "What is a sensor," Sensor learning, 2018. [Online]. Available: https://www.sensorcleaning.com/whatisasensor.php. [Accessed 25 March 2022].

[69] C. H. Museum, "1963: Complemetary MOS Circuit Configuration is invented," Computer History Museum, [Online]. Available: https://www.computerhistory.org/siliconengine/complementary-mos-circuit-configuration-is-invented/. [Accessed 25 March 2022].

[70] T. Flir, "How to Evaluate Camera Sensitivity," Teledyne Flir, 17 March 2021. [Online]. Available: https://www.flir.com/discover/iis/machine-vision/how-to-evaluate-camera-sensitivity/. [Accessed 20 May 2022].

[71] L. Susstrunk, R. Buckley and S. Swen, "Standard RGB colour spaces," in

IS&T/SID 7th Colour Imaging Conference, Scottsdale, Arizona, USA, 1999.

[72] SharkD, "Wikimedia Commons File:RGB color solid cube.png," 12 January 2008. [Online]. Available: https://en.wikipedia.org/wiki/File:RGB_color_solid_cube.png. [Accessed 20 May 2022].

[73] V. Vicente, "What Does “RGB” Mean, and Why Is It All Over Tech?," 11 July 2021. [Online]. Available: https://www.howtogeek.com/730577/what-does-rgb-mean-and-why-is-it-all-over-tech/. [Accessed 20 May 2022].

[74] "Camera Exposure," Cambridge in Colour, [Online]. Available: https://www.cambridgeincolour.com/tutorials/camera-exposure.htm. [Accessed 16 April 2020].

[75] J. Honour, "A brief history of principles used in high speed cameras," *The Imaging Science Journal,* vol. 6, no. 57, pp. 303-316, 2009.

[76] M. Peres, The Focal Encyclopedia of Photography, New York: Taylor & Francis Gropu, 2007.

[77] H. Xing, Q. Zhang, C. H. Braithwaite, B. Pan and J. Zhao, "High-Speed Photography and Digital Optical Measurement Techniques for Geomaterials: Fundamentals and Applications," *Rock Mechanics and Rock Engineering,* vol. 6, no. 50, pp. 1-49, 2017.

[78] B. Brixner, J. E. Mack, C. K. Perkins, W. G. Marley and J. Aeby, "High-speed Photography," Atomic Heritage Foundation, 10 July 2017. [Online]. Available: https://www.atomicheritage.org/history/high-speed-photography. [Accessed 23 April 2022].

[79] K. S. Balch, "Fourth-generation motion analyzer," *19th Intl Congress on High-Speed Photography and Photonics,* vol. 1358, pp. 373-398, 1990.

[80] P. Limited, "FASTCAM SA 4/ FASTCAM SA4 RV Hardware Manual," Photron Limited, Tokyo, 2009.

[81] V. Research, "Phantom V210 Data Sheet," Vision research, New Jersey, 2009.

[82] P. Evans, "Properties of Air at atmospheric pressure," Theengineeringmindset, 29 March 2015. [Online]. Available: https://theengineeringmindset.com/properties-of-air-at-atmospheric-pressure/. [Accessed 23 May 2022].

[83] "Oxygen - Density and Specific Weight vs. Temperature and Pressure," The Engineering ToolBox, 2022. [Online]. Available: https://www.engineeringtoolbox.com/oxygen-O2-density-specific-weight-temperature-pressure-d_2082.html. [Accessed 23 May 2022].

[84] C. J. McDaid, "Developing and Implementing Advanced Optical Diagnostics for the Investigation of Fuel and Flow Effects on Ignition, Flame Structure

and Wall Temperature of Impinging Jet Flames," The University of Sheffield, Sheffield, 2013.

[85] Cannon, "Cannon," 2022. [Online]. Available: https://www.canon.co.uk/for_home/product_finder/cameras/digital_slr/eos_1200d/. [Accessed 15 May 2022].

[86] B. Planetarium, "Badder H-alpha 7 nm CCD Narrowband-Filter," Badder Planetarium, 2022. [Online]. Available: https://www.baader-planetarium.com/en/baader-h-alpha-7nm-ccd-narrowband-filter.html. [Accessed 14 May 2022].

[87] C. Palmer, Diffraction Grating Handbook, 5th edition ed., New York: Thermo RGL Richard Grating Laboratory, 2002.

[88] P. S. Foundation, "Python (3). [Software]," 1995.

[89] C. R. Harris, K. J. Millman and S. J. van der Walt, "Array Programming with NumPy.," *Nature,* p. 585, 2020.

[90] E. Jones, T. Oliphant and P. Peterson, "SciPy: Open Source Scientific Tools for Python," 2001.

[91] S. Van der Walt, J. L. Schnberger and J. Nunez-Iglesi, "Scikit-image: image processing in Python. PeerJ 2 e453," 2014.

[92] B. planetarium, "DADOS: Baader Blaze Reflection Gratings 1200 L/mm," Baader planetarium, 2022. [Online]. Available: https://www.baader-planetarium.com/en/baader-blaze-reflection-gratings-1200-lmm.html. [Accessed 24 May 2022].

[93] SkywalkerPL, "Wikimedia Commons," 26 August 2012. [Online]. Available: https://en.wikipedia.org/wiki/File:Sony_A77.jpg#file. [Accessed 5 May 2022].

[94] P. E. Ciddor, "Refractive index of air: new equations for the visible and near infrared.," *Applied Optics,* vol. 35, pp. 1566-1573, 1996.

[95] J. A. Stone and J. H. Zimmerman, "Engineering Metrology Toolbox," 2019. [Online]. Available: https://emtoolbox.nist.gov/Wavelength/Documentation.asp#References. [Accessed 3 January 2022].

[96] J. A. Stone and J. H. Zimmerman, "Index of Refraction of Air Vacuum Wavelength and Ambient Conditions Based on Ciddor Equation," 2004. [Online]. Available: emtoolbox.nist.gov/wavelength/ciddor.asp. [Accessed 27 December 2021].

[97] J. A. Stone and J. H. Zimmerman, "Engineering Metrology Toolbox," 2019. [Online]. Available: https://emtoolbox.nist.gov/Wavelength/Documentation.asp#References. [Accessed 3 January 2022].

[98] P. E. Ciddor, "Refractive index of air: new equations for the visible and near infrared," *Apply Optics*, vol. 35, pp. 1566-1573, 1996.

[99] T. W. Hnsch, M. H. Nayfeh, S. A. Lee, S. M. Curry and I. S. Shahin, "Precision Measurement of the Rydberg Constant by Laser Saturation Spectroscopy of the Balmer α Line in Hydrogen and Deuterium," *Phys. Rev. Lett.,* vol. 32, pp. 1336-1340, 1974.

[100] P. Zhao, W. Lichten, H. Layer and J. C. Bergquist, "Remeasurement of the Rydberg constant," *Phys. Rev. A.,* vol. 34, pp. 5138-5141, 1986.

[101] J. G. Quintiere, Principles of Fire Behavior, New York: Delmar, a division of Thomson Learning, 1998.

[102] I. Glassman, R. A. Yetter and N. G. Glumac, Combustion, London: Academic Press, 2015.

[103] D. D. Pollock, Thermocouples: theory and properties, Boca Raton: CRC Press, 1991.

[104] "Thermocouple technical reference information," [Online]. Available: https://www.sterlingsensors.co.uk/thermocouples. [Accessed 18 March 2022].

[105] A. N. Cox, Allen's Astrophysical Quantities, New York: Springer Science+Business Media New York, 2002.

[106] H. Schardin, "Schlieren methods and their applications," NASA, Washington DC, 1970.

[107] G. S. Settles, Schlieren and shadowgraph techniques: visualizing phenomena in transparent media, New York: Springer-Verlag, 2001.

[108] T. Liu, J. Ji, F. Qi, L. Yang, M. Xu and Q. Yao, "Development of China's Fundamental Research in Combustion," *Science Foundation in China,* pp. 325-329, 2012.

[109] A. A. Ovsyannikov and M. F. Zhukov, Plasma Diagnostics, Cambridge: Cambridge International Science Publishing, 2000.

Appendix

Appendix I-RGB Python Script

```
from PIL import Image
import matplotlib.pyplot as plt
import matplotlib.image as mapimg
import numpy as np

I = mapimg.imread ('file path')
I1 = I.astype(np.float64)
J = np.average(I1[:,:,0])+10

I1[I1[:,:,0]<=J] = [0,0,0]
I2 = I1.astype(np.uint8)
plt.imshow(255-I2)

T =np.array([[0,0,0,0,0]])
i_index = np.size(I1,0);
j_index = np.size(I1,1);
count = 0;
for i in range(i_index):
    for j in range(j_index):
        if (I1[i,j,0]!=0):
            T=np.append(T,[[I1[i,j,0],I1[i,j,1],I1[i,j,2],i,j]], axis =
 0)
            count = count + 1


Red_average = np.average(T[:,0])
Green_average = np.average(T[:,1])
Blue_average = np.average(T[:,2])

Red_median = np.median(T[:,0])
Green_median = np.median(T[:,1])
Blue_median = np.median(T[:,2])

Red_amax = np.max(T[:,0])
Green_amax = np.max(T[:,1])
Blue_amax = np.max(T[:,2])

def tenmaxavg(T,i):
   R = abs(np.sort(-T[:,i]))
   Red_tma = np.average(R[1:10])
```

```
    return Red_tma

Red_tma = tenmaxavg(T, 0)
Green_tma = tenmaxavg(T, 1)
Blue_tma = tenmaxavg(T, 2)

print('Average R,G,B is ',Red_average,Green_average,Blue_average)
print('median R,G,B is ',Red_median,Green_median,Blue_median)
```

Appendix II-Spectrum Python Script

```
import matplotlib
import matplotlib.pyplot as plt
import numpy as np
from PIL import Image
from scipy import interpolate
from scipy import ndimage

matplotlib.style.use('seaborn-paper')


def pre_process_image(img: np.ndarray) -> np.ndarray:
    image_01_np = img

    if image_01_np.shape[2] == 3:
        image_02_grayscale = np.dot(image_01_np, (1, 0, 0))
    elif image_01_np.shape[2] == 4:
        image_02_grayscale = np.dot(image_01_np, (1, 0, 0, 0))
    else:
        raise ValueError(image_01_np.shape)

    image_02_grayscale = ndimage.median_filter(image_02_grayscale, 3)

    return image_02_grayscale


def calibrate_f2p_p2f(p_1=5173, f_1=588.9950, p_2=5189, f_2=589.5924):
    def make_func(x1, y1, x2, y2):
        return lambda x: (y1 - y2) / (x1 - x2) * x + (y1 - (y1 -
 y2) / (x1 - x2) * x1)


    p2f = make_func(y1=f_1, x1=p_2, y2=f_2, x2=p_1)
    f2p = make_func(x1=f_1, y1=p_2, x2=f_2, y2=p_1)

    return f2p, p2f


def make_final_plot(p2f: Callable, img: np.ndarray, fp_img: str = None,
                    text_xys=None, vlines=None, sum_area_width: int = 1
50):

    fig, (ax1, ax2) = plt.subplots(
        figsize=(5.67, 3), nrows=2, gridspec_kw={'height_ratios': [1, 1
0]}, sharex=True, dpi=200
    )
```

```
    y_sum_mov_ave_tol = 150
    y_sum = np.average(img, axis=1)  # sum along y-axis, i.e., columns
    y_sum_mov_ave = np.zeros_like(y_sum)
    for i in range(len(y_sum)):
        i1 = max(0, i - y_sum_mov_ave_tol)
        i2 = min(len(y_sum), i + y_sum_mov_ave_tol)
        y_sum_mov_ave[i] = np.sum(y_sum[i1:i2])
    y_sum_mov_ave = y_sum_mov_ave / y_sum_mov_ave.max() * 1e3
    y_sum_mov_ave_peak = np.argmax(y_sum_mov_ave)
    print(f'Peak on y-axis: {y_sum_mov_ave_peak} ± {y_sum_mov_ave_tol}')

    i1 = y_sum_mov_ave_peak - y_sum_mov_ave_tol
    i2 = y_sum_mov_ave_peak + y_sum_mov_ave_tol
    img_cropped = img[i1:i2, :]

    ax1.imshow(img_cropped, cmap='gray', aspect='auto', extent=(p2f(0),
 p2f(img_cropped.shape[1]), -1, 1))

    ax1.set_xticks(())
    ax1.set_yticks(())
    ax1.tick_params(axis='x', which='both', labelbottom=False, bottom=F
alse)

    x = p2f(np.arange(img_cropped.shape[1]))
    y = np.average(img_cropped, axis=0)
    func_frequency2intensity = interpolate.interp1d(x, y)

    def add_text(x_, y_, s_, l_y_max=None, ax_=ax2):
        kw_text = dict(clip_on=True, ha='center', va='bottom', fontsize
='xx-small', color='r', rotation='vertical')
        ax_.text(x_, y_, s_, **kw_text)
        if l_y_max is not None:
            ax_.vlines(x_, 0, l_y_max, colors='r', lw=0.5)
```

Appendix III-Hydrogen Datasheet

BOC
A Linde company

Hydrogen Research Grade (N5.5)

Gas
→ Hydrogen research grade (N5.5)

Specification
99.9995% minimum
→ nitrogen ≤5 ppm
→ oxygen ≤1 ppm
→ carbon dioxide ≤0.5 ppm
→ total hydrocarbons ≤1 ppm
→ moisture ≤2 ppm
→ carbon monoxide ≤1 ppm

The above concentrations are ideal volume fractions (= mole fractions).

Part numbers
290626-L, 110971-F, 162657-RSH, 162600-RSQ.

Cylinder size	Cylinder contents volume (m^3)†	Maximum filled pressure at 15°C (bar)	Approx. dimensions (H x ø) - heights are given to centre of typical valve outlet (m)	Approx. gross cylinder weight (kg)
L	8.80	200	1.54 x 0.23	71
F	1.17	137	0.82 x 0.14	18
RSH*	0.135	150	0.44 x 0.095	3
RSQ**	0.135	150	0.44 x 0.095	3

† Volume of gas expanded to 15°C, 1atm
ø Represents cylinder diameter

Appendix IV-Oxygen Datasheet

BOC
A Member of The Linde Group

Oxygen N5.5

Gas
→ Oxygen N5.5

Specification
99.9995% minimum
→ nitrogen ≤2 ppm
→ argon ≤2 ppm
→ total hydrocarbons ≤0.05 ppm
→ hydrogen ≤0.05 ppm
→ moisture ≤1 ppm

The above concentrations are ideal volume fractions (= mole fractions).

Part numbers
284916-L, 284918-V, 284916-WL-C.

Cylinder size	Cylinder contents volume (m^3)†	Maximum filled pressure at 15°C (bar)	Approx. dimensions (H x ø) - heights are given to centre of typical valve outlet (m)	Approx. gross cylinder weight (kg)
L	10.64	200	1.54 x 0.23	84
V	2.12	200	0.88 x 0.14	22

Manifolded 15 cylinder pallet (MCP)	MCP contents volume (m^3)†	Maximum filled pressure at 15°C (bar)	Approx. dimensions (H X W X D)‡ - heights are given to centre of typical valve outlet (m)	Approx. gross MCP weight (kg)
WL	159.6	200	1.85 x 1.29 x 0.84	1536

† Volume of gas expanded to 15°C, 1atm
ø Represents cylinder diameter
‡ Height x width x depth